Universitat de Lleida

Energy characterization and experimental validation of natural ventilated semitransparent double skin PV components

Jordi Cipriano Líndez

Dipòsit Legal: L.228-2015
http://hdl.handle.net/10803/286038

Universitat de Lleida

Energy characterization and experimental validation of natural ventilated semitransparent double skin PV components

Jordi Cipriano Líndez

PhD program: Enginyeria i Tecnologies de la Informació

Directors: Daniel Chemisana, Guillaume Houzeaux

September 2014

Agraïments

Vull agrair aquesta tesi a la Laia, el Dídac i a la Jana. Sense ells, sobre tot sense tot l'amor de la Laia, la seva paciència i el permís de "flexibilitzar" les meves càrregues familiars durant tot un any, no hagués pogut fer la part final d'aquesta tesi.

També vull agrair als meus pares tot el sacrifici que van haver de fer per a que jo i els meus germans poguéssim finalitzar exitosament les nostres carreres, i que en el meu cas, ha constituït la base del coneixement que he desenvolupat en aquesta tesi. Especialment vull agrair a la meva germana Núria la seva manera d'afrontar la vida i el seu suport moral i logístic i al meu germà Xavi per estar dia dia al meu costat mirant de tirar endavant tot el projecte del Bee Group.

Vull donar també les meves gràcies a tot l'equip del Bee Group, començant pels de Lleida, el Gerard, el Josep, la Meredith i el Jose per cobrir les tasques que he hagut de deixar mentre estava escrivint la tesi. I acabant pels de Terrassa, el Dani, el Jordi, l'Stoyan, el Fabio, el Mike, la Gabi, el Gonzalo, el Xavi, l'Oriol i, des de la llunyania, el Jaime, per fer que cada dia que em llevo per anar a treballar, ho faci amb la il · lusió i la confiança de que estem construint un projecte coherent, sòlid i amb molta implicació, tant personal com cap a la societat en la que vivim.

No em vull descuidar de donar les gràcies al Joan Ignasi, al Dani i al Jerome, pel fet de permetre'm establir-me a Lleida, desenvolupar les meves activitats amb total confiança i finalment poder presentar la tesi a la UdL. Vull fer menció especial al Dani, per l'empenta que m'ha donat els últims mesos per a que pogués acabar en el plaç que m'havia marcat.

Vull agrair també a tot l'equip de CIMNE, especialment a l'Anna, el Javier, la Mari Carmen, la Merce, la Mercè, el Dani, el Francisco i el Valentín, per portar endavant una estructura tan complexa com és el CIMNE i per a aguantar-nos cada dia.

No em vull oblidar del Guillaume, del Javier i del Mariano per haver-me despertat la inquietud de començar seriosament el doctorat i per estar sempre disposats a escoltar i a compartir converses i moments molt interessants.

Vull donar les gràcies al David, a l'Edu, al Gustavo, a la Eva, al Salvador, al Pep i al Josep Maria per la seva constància i implicació en fer créixer el que va ser una idea fa déu anys i que s'ha plasmat en el que és ara Inergy.

Vull mencionar també als companys d'Aiguasol i Pich Aguilera per estar sempre disposats a fer coses junts, especialment al Jordi Pascual perquè em deu un sopar...

Finalment, vull fer menció especial a l'Eugenio, per ser la primera persona que va creure que dos joves inexperts es podien sortir en la creació d'un grup autònom i autàrquic i per donar-me la confiança i la llibertat de poder treballar en el que m'agrada durant tants anys.

Lleida 31 d'Octubre de 2014

Contents

Abstract

Double skin semi transparent components with Photovoltaic integrated systems are building components which combine functions of the building envelope with natural lighting, electricity and thermal energy generation. The energy transfer modeling of these components, especially under free convection situations, raises a high complexity and is the first main drawback for a massive dissemination of this technology. Many attempts to fill this gap have been undertaken and some mathematical correlations and dynamic simulation models to evaluate the overall energy performance of these components have been obtained in the last decades. However, very few studies have faced a detailed analysis of the valid range of these mathematical expressions and simulation models and of the restrictions entailed.

The second drawback for a wide spread of these complex PV components is related to the difficulty in setting up monitoring and experimental campaigns to measure their real energy performance with sufficient accuracy and precision. This difficulty is dramatically increased in the case of natural ventilated PV components since the air flow within the ventilated air gap is very erratic, turbulent and non stationary.

Besides the drawbacks in the energy modeling and in the measurement of ventilated PV components in real conditions, there is also a lack of knowledge on methods for calibrating building energy simulation models in general, and specifically in the calibration of dynamic models of ventilated PV components. The calibration of forward complex dynamic models plays a fundamental role in building energy performance analysis and is a critical factor for a proper evaluation of the energy savings produced by the building integration of these natural ventilated PV components . In order for the dynamic simulation models to be used with any degree of confidence, it is necessary that the existing model closely represents the actual behaviour of the component under study.

This PhD thesis addresses these existing drawbacks and introduces an overall methodology for the energy characterization and experimental validation of ventilated PV components. This research also contributes in increasing the knowledge on methods for coupling the mathematical development of dynamic simulation models with innovative approaches for its calibration with experimental measures. It aims at getting more insights of different approaches to analyze the valid range of the mathematical correlations for the heat transfer processes, of the dynamic models and its large number of unknown parameters, and of the existing methods for the optimization of the calibration process.

Resum

Els sistemes integrats Fotovoltaics (FV) de doble pell, són components de l'edifici que combinen les funcions d'envolvent, amb les d'il · luminació natural, generació d'electricitat i generació d'energia tèrmica. La modelització dels processos de transferència d'energia d'aquests components, especialment en situacions de convecció natural, planteja una alta complexitat i és un dels inconvenients principals per a una disseminació massiva d'aquesta tecnologia. En les últimes dècades s'han dut a terme diferents intents per a superar aquest inconvenient i s'han desenvolupat diferents correlacions matemàtiques i models de simulació per a avaluar l'eficiència energètica global d'aquests sistemes. No obstant això, molt pocs estudis s'han enfrontat a una anàlisi detallat del rang de validesa d'aquestes correlacions i models i tampoc de les limitacions inherents en la seva definició. El segon inconvenient per a una àmplia propagació d'aquests components FV complexos, està relacionat amb la dificultat per a dur a terme campanyes experimentals de mesura del seu comportament energètic en condicions reals. Aquesta dificultat s'incrementa dramàticament en el cas de condicions de convecció natural, principalment, perquè el flux d'aire dins del canal ventilat és molt turbulent i no estacionari. A més dels inconvenients en la modelització de la transferència d'energia i en la mesura experimental en condicions reals, s'hi afegeix una gran manca de coneixement sobre mètodes estandarditzats per a la cal · libració dels models de simulació de components FV ventilats . La cal · libració de models dinàmics juga un paper fonamental en el camp de l'anàlisi energètic d'edificis i representa un factor molt crític per a una correcta avaluació dels estalvis d'energia generats per la integració d'aquests components FV ventilats en els edificis. Per tal que els models de simulació dinàmica puguin ser utilitzats amb suficient grau de fiabilitat, és del tot necessari que el model teòric representi, amb prou exactitud, el seu comportament real.

Aquesta tesi doctoral aborda aquests inconvenients mencionats i introdueix una metodologia general per a la caracterització energètica i la validació experimental dels components FV ventilats. Aquesta investigació també contribueix a augmentar el coneixement sobre mètodes per a integrar el desenvolupament de models de simulació dinàmica, amb enfocaments innovadors per a la seva cal · libració. Finalment, aquesta tesi pretén aconseguir un major coneixement sobre estratègies en l'anàlisi de les correlacions de transferència de calor, dels models de simulació dinàmica i dels mètodes d'optimització del procés de cal · libració.

Resumen

Los sistemas integrados Fotovoltaicos (FV) de doble piel, son components del edificio que combinan las funciones de envolvente, con las de illuminación natural, generación eléctrica y generación de energía térmica. La modelització de los procesos de transferència de energia de estos components, especialmente en situaciones de convección natural, plantea una alta complejidad y es uno de los inconvenientes principales para una diseminación masiva de esta tecnología. En las últimas décadas, se han llevado a cabo diferentes intentos para a superar este inconveniente y se han desarrollado diferentes correlaciones matemáticas y modelos de simulación para evaluar la eficiéncia energética global de estos sistemas. Sin embargo, muy pocos estudios se han enfrentado al análisis detallado del rango de validez de estas correlaciones y modelos y tampoco de las limitaciones inherentes en su definición. El segundo inconvenient para una amplia propagación de estos components FV complejos, está relacionado con la dificultad para llevar a cabo campañas experimentales de medida de su comportamento energético en condiciones reales. Esta dificultad se incrementa dramáticamente en el caso de condiciones en convección natural, principalmente, porqué el flujo de aire dentro del canal ventilado es muy turbulento y no estacionario. Además de estos inconvenientes en la modelización de la transferència energética y en la medida experimental en condiciones reales, se constata una carencia significativa de conocimiento sobre métodos estandarizados para la calibración de los modelos de simulación de componentes FV ventilados . La calibració de modelos dinámicos juega un papel fundamental en el campo del análisis energético de edificios y representa un factor muy crítico para una correcta evaluación de los ahorros energéticos que se puedan conseguir con la integración de estos componentes FV ventilados en los edificios. Para que los modelos de simulación dinámica se puedan utilizar con suficiente grado de fiabilidad, es totalmente necesario que el modelo teórico represente, con suficiente exactitud, su comportamiento real.

Esta tesis doctoral aborda todos estos inconvenientes mencionados anteriormente e introduce una metodología general para la caracterización energética y la validación experimental de los componentes FV ventilados. Esta investigación también contribuye a aumentar el conocimiento sobre métodos para integrar el desarrollo de modelos de simulación dinámica, con estrategias innovadoras para su calibración. Finalmente, esta tesis pretende profundizar en estratégias de análisis de las correlacions de transferencia de calor, de los modelos de simulación dinámica y de los métodos de optimización del proceso de calibración.

Chapter 1

Introduction and scope of the research

Photovoltaic (PV) elements only allow to transform about 10 % (amorphous silicon) to 20 % (mono-crystalline silicon) of the incident solar radiation into electrical energy. The remaining incident solar radiation is converted into sensible heat, which results in warming-up of the PV elements. This increase in temperature leads to a reduction of the PV efficiency (by 0.4-0.5 % per temperature degree), thus, an attractive concept is to integrate the PV systems in buildings as double skin ventilated façades and to use the heating-up of the elements for generating a buoyancy effect within the ventilated air gap. This approach simultaneously improves the thermal performance of the buildings and the PV efficiency.

Although in recent years some shining examples of newly constructed buildings have shown the benefits of this strategy, the spread of this technology has not occurred at the necessary scale. Most of the projects of building integrated photovoltaics have historically been conceived as outstanding buildings where the electricity production and the visual integration of the PV was the priority. The heat energy produced at the back side of the PV systems has been rarely used as a thermal energy source or as a way to improve the thermal resistance of the outer skin.

One of the reasons of underestimating the potential of the heat energy produced at the back side of the PV cells, we believe, has to do with the high complexity of evaluating the heat transfer processes which occur within the ventilated air gap. More specifically, the main drawback to overcome concerns the evaluation of the convective heat transfer coefficients and the air mass flow rate. Unless sophisticated predictive tools such as Computational Fluid Dynamics codes (CFD) or Artificial Neural Networks, most of the existing transient dynamic prediction models use mathematical correlations which relate these two variables with the corresponding dimensionless numbers and the air flow regimes. In recent years, many authors have been addressing this problematic. Since the 1990's Hans Bloem, of the Joint Research Center [1, 2, 3, 4], has been carrying out an intensive characterization of PV ventilated façades, with and without ventilated air gaps. Some European funded projects have been actively supporting this work, PASSLINK, PV-HYBRIDPAS and IMPACT [5]. Between 1999 and 2000, Ursula Eicker, [6] undertook the theoretical analysis and monitoring of the Mataro's public library building, which had the first PV ventilated façade in Europe. More recently, the treatment of the induced flow and the heat transfer at the air gap and the surfaces of a natural ventilated double skin façade has been progressively refined by Brinkworth [7, 8, 9, 10].In most of these previous studies, two predominant situations were considered for the boundary conditions within the

ventilated air gap: symmetric boundary conditions and asymmetric boundary with adiabatic wall at the coldest side. These boundary conditions are very common when the double PV skins are formed by opaque PV panels at the outer skin and an opaque wall at the inner side. Nevertheless, in the case of double skins formed by semi-transparent PV panels, the short wave solar radiation crosses the transparent layers among the PV cells and heats the inner wall, leading to asymmetric boundary conditions situation. This situation was faced by Aung et al. [11], however, no expressions for the heat transfer co- efficient of each wall were obtained. The mathematical correlations obtained by Brinkworth [7, 8, 9, 10] present some discontinuities which clearly invalidate their use within iterative dynamic software tools.

Another factor which makes more difficult the wide spread of integrated ventilated PV components is related to the technical data provided by the PV industry. The PV manufacturers normally include only the electrical performance under Standard Test Conditions (STC) and measurements of Nominal Operating Cell Temperature (NOCT), as described in the IEC 61215 [12]. However, building designers and engineers require performance indicators of PV systems under real operating conditions for a typical climate, location and building integration situation. Some insights on the effect of the inclination, the air flow regime and the materials which form the rear side of these double skins, need to be obtained and provided to the European construction sector. Previous studies addressed this need through indoor experimental procedures [13, 14]. These procedures are normally accurate and replicable, however they do not take into account the dynamic variations in the boundary conditions of the components once they are integrated into a real building. On the other hand, experiences involving the measurements of double skin BIPV systems in real buildings, revealed that these studies are expensive and problematic in achieving good quality data. Therefore, controlled outdoor test facilities may be considered as an economical and practical intermediate bridge between laboratory tests and monitoring of real and occupied buildings. In these kind of controlled outdoor test environments, real climate effects are taken into account and high accuracy of the data is reached while avoiding occupancy effects.

Concerning to the mathematical model to define the energy performance of ventilated PV components, simplified methods have been proposed by Ursula Eicker [15] and Li Mei [6]. More sophisticated models for double skin façades have bee also developed by Debora Faggembau [16] and Dirk Saelens [17, 18]. Mats Sandberg [19, 20, 21] has carried out a detailed analysis of the convective heat transfer within the air channel. All these authors have assumed forced flow correlations for the convection heat transfer coefficient and they didn't consider the effect of the asymmetry in the laminar boundary conditions. Saelens [17] also made a review of several ways to model the air channel and he concluded that a single volume model with linear variation of the average temperature has he same accuracy than finite difference schemes. In this research, this model will be used to analyze the energy and mass flow rates within the air gap of the PV ventilated façade. In parallel, Yun et. [22] used the software ESP-r to model the overall energy performance of a ventilated PV façade and defined a new index of effectiveness which included the reduction in artificial lighting, the thermal energy and the electrical energy produced. In this study, a parameter optimization has been performed but without a contrast with experimental measures. Although these detailed studies have lead to an increase in the knowledge of the heat transfer processes, there are still many unclear fields such as: the convective heat transfer coefficients definition; the evaluation of the direct solar radiation absorbed by the solid parts; the evaluation of the air mass flow rate in non-developing turbulent flows and, and the methodology to validate the predictive dynamic model.

This last field related with the validation of the theoretical models and the reduction of the gap between the dynamic simulation models and the real energy performance, also known as calibration procedure, plays a fundamental role in building energy performance analysis and is a

critical factor for proper evaluation of energy savings produced by the integration of ventilated PV components in buildings . In order for a dynamic model to be used with any degree of confidence, it is necessary that the existing model closely represents the actual behaviour of the building component under study. The need for calibration of dynamic models is not an indication of the limited capacity for the prediction; it is ,instead, a manifestation of the limited knowledge that the model developer has on the operational parameters of the component, as well as on the stochastic nature of the external inputs. Calibration can be understood as the process of "fine-tuning" the values of the unknown parameters of a model in order to minimize the differences between the predicted outputs and the observed data. Due to the large number of unknown input parameters in a detailed dynamic simulation model, calibration is a complex procedure characterized by a non-unique solution and high uncertainties.

This research aims at addressing some of the issues previously mentioned that are delaying the massive integration of ventilated PV components in buildings. In order to achieve the requirements of the new EU directive on the energy performance of buildings (EPBD) [23], solar energy technologies integrated in the building envelopes need to be promoted and new integral methodologies for the characterization, parametric analysis and optimization of these innovative component should be developed.

This PhD thesis starts with a contribution to the increase in the the basic knowledge of the basic heat transfer processes which occur within natural ventilated PV components by means of a detailed analysis of the valid range of the existing mathematical correlations and by providing an evaluation of the effect of the asymmetry in the wall boundary conditions. A Computational Fluid Dynamics code (CFD), based on finite elements approach, has been used as the basic tool to calibrate the accuracy of each mathematical correlation.

The PhD thesis then follows with a landing to the reality of these PV systems through the construction of a an improved version of the outdoor test reference environment (TRE), developed by J.J. Bloem [2], named the TRE-L. The TRE-L has been designed and built at the Lleida Outdoot Test Center (LOTCE) [2, 24] in 2009 and further improved in 2013, and the results from the extended monitoring campaigns are presented herewith. Detailed analysis of the effect of different ventilation regimes, including natural ventilation, several inclinations and rear facing materials over the energy performance of the double skin PV system are carried out and conclusions are presented. The performance of the ventilated PV module placed at the TRE-L is also compared with the performance of other two identical PV modules: one reference module which is fully insulated and another reference PV module which is kept under free-rack conditions.

The PhD thesis finishes with the development and validation of a multi stage calibration procedure, based on Latin Hypercube Montecarlo Methods (LHMC), as well as its integration with a flexible transient simulation model of a PV ventilated component. In order to reduce the uncertainty of the calibration method before applying it to the dynamic model, a detailed evaluation of the effect of the LHMC sampling size and the number of iterations, over the strong parameters detection and over the deviation with the monitored data, is carried out in the next to last paper and some conclusions are obtained.

The last paper of the PhD thesis is centered in the definition and programming of a very flexible dynamic simulation model and its integration with the calibration methodology previously developed and validated. A systemic approach to identify strong and weak parameters of the model is also adapted to the specific conditions of natural ventilated semitransparent PV components. This overall analysis methodology is recommended for use as a method to evaluate mid to long term predictions of the thermal and electrical energy produced by ventilated PV components and to achieve high goodness of fit with the measured data.

1.1 Main stages of the research

This research is structured in the following stages:

1. Intensive evaluation of the existing heat transfer relations for asymmetrical heated vertical air channels under free convection
2. Experimental analysis of the energy performance of a ventilated double skin photovoltaic component in a controlled outdoor test reference environment
3. Definition of a valid methodology to calibrate dynamic building energy models applying uncertainty and sensitivity multi-stage analysis methods
4. Developing of a dynamic simulation model of a semi-transparent double skin PV component and calibration of the model with the experimental data

Chapter 2

Methodology

2.1 Paper 1: Numerical Analysis of the most appropriate heat transfer correlations for free ventilated double skin Photovoltaic Façades

2.1.1 Introduction

This paper has been accepted in a journal published by Elsevier. More details are:

Title: Numerical analysis of the most appropriate heat transfer correlations for free ventilated double skin photovoltaic façades

Authors: Jordi Cipriano, Guillaume Houzeaux, Daniel Chemisana, Chiara Lodi , Jaime Martí-Herrero

Journal: Applied Thermal Engineering. Vol. 57 (2013). p.p. 57-68

This paper aims at increasing the knowledge of the heat transfer processes which occur in these situations by means of a detailed analysis of the valid range of the existing mathematical correlations and by providing an evaluation of the effect of the asymmetry in the wall boundary conditions.

2.2 Paper 2: Experimental evaluation of the energy performance of semi transparent ventilated double skin photovoltaic components

2.2.1 Introduction

The aim of this paper is to analyze the effect of different ventilation regimes, including natural ventilation, several inclinations and rear facing materials over the energy performance of the double skin BIPV system. The performance of the ventilated PV panel placed at the TRE-L is also compared with the performance of other two identical PV modules: one reference module which is fully insulated and another reference PV module which is kept under free-rack conditions.

The paper starts with the description of the experimental set-up. It follows the analysis of the experimental results and the evaluation of the overall energy and exergy performance of the component. Finally, conclusions are drawn and further developments are outlined.

2.3 Paper 3: Evaluation of a multi-stage guided search approach for the calibration of building energy simulation models

This paper has been accepted in a journal published by Elsevier. More details are:

Title: Evaluation of a multi-stage guided search approach for the calibration of building energy simulation models

Authors: Jordi Cipriano, Gerad Mor, Daniel Chemisana, Daniel Pérez , Gonzalo Gamboa, Xavier Cipriano

Journal: Energy and Buildings. The volume and date of publication are not yet received.

2.3.1 Introduction

In this paper, a new procedure for calibration BES models of buildings under free-floating conditions is proposed. This procedure has many similarities with the methodology defined by [25], however some changes are implemented. In this research, a multi stage procedure based on Latin Hypercube Monte Carlo is also used, however, in stead of fixing the strong parameters to discrete values, as proposed by [25], a re-assignment of their estimates and range of variation is carried out after each iteration. A detailed evaluation of the effect of the LHMC size over the strong parameters detection and over the deviation with the monitored data is also carried out and some conclusions are obtained.

2.4 Paper 4: Integrated development and calibration of a dynamic model for natural ventilated photovoltaic components

2.4.1 Introduction

In this paper, a contribution to achieve deeper knowledge in the energy performance of ventilated PV components is proposed by the development of a very flexible dynamic simulation model and the integration of a calibration methodology previously developed and validated. A systemic approach to identify strong and weak parameters of the model is also adapted to the specific conditions of these components. This calibration methodology is recommended for use as a method to evaluate mid to long term predictions of the thermal and electrical energy produced by ventilated PV components and to achieve high goodness of fit with the measured data.

Chapter 3

Articles

Applied Thermal Engineering 57 (2013) 57–68

Contents lists available at SciVerse ScienceDirect

Applied Thermal Engineering

journal homepage: www.elsevier.com/locate/apthermeng

Numerical analysis of the most appropriate heat transfer correlations for free ventilated double skin photovoltaic façades

Jordi Cipriano [a], Guillaume Houzeaux [b], Daniel Chemisana [c,*], Chiara Lodi [c], Jaime Martí-Herrero [a]

[a] Building, Energy and Environment Group, International Center for Numerical Methods in Engineering (CIMNE), 08224 Terrassa, Spain
[b] Barcelona Supercomputing Center (BSC-CNS), 08034 Barcelona, Spain
[c] Applied Physics Section of the Higher Polytechnic School (EPS), University of Lleida, Jaume II 69, 25001 Lleida, Spain

HIGHLIGHTS

- This paper focuses on the heat transfer modelling of double skin PV façades.
- The validity range of existing heat transfer mathematical correlations is analysed.
- A numerical code is used and calibration with experimental measures is carried out.
- Asymmetrical boundary conditions affect heat transfer only for small Rayleigh numbers.
- Asymmetrical boundary conditions affect air mass flow rate for high Rayleigh numbers.

ARTICLE INFO

Article history:
Received 20 November 2012
Accepted 23 March 2013
Available online 10 April 2013

Keywords:
Double skin photovoltaic facades
Free convection
Heat transfer correlations
Computational Fluid Dynamics (CFD)

ABSTRACT

Double skin façades with photovoltaic integrated systems are building components which combine functions of the building envelope with electricity and thermal energy generation. The heat transfer modelling of these components, especially under free convection situations, raises a high complexity and is one of the main drawbacks for a massive dissemination of this technology. Many attempts to fill this gap have been undertaken and some mathematical correlations allowing evaluating average Nusselt numbers and air mass flow rate have been obtained in the last decades. However, very few studies faced a detailed analysis of the valid range of these mathematical expressions and of the restrictions entailed. This paper introduces a methodology to analyse the valid range of the existing mathematical correlations for the convective heat transfer coefficients and for the air mass flow rate in laminar and transition to turbulent free convection, and provides an evaluation of the effect of the asymmetry of the wall boundary conditions. A specific numerical code, based on a stabilized finite element formulation (FEM), is used to solve the incompressible Navier–Stokes equations within the air gap and to determine the accuracy of the existing heat transfer correlations. This evaluation was preceded by an extensive bibliographic research as well as a detailed validation of the physical and numerical hypothesis adopted in the finite element code.

1. Introduction

Commercial photovoltaic (PV) elements only allow transforming about 14–20% of the incident solar radiation into electrical energy. The remaining incident solar radiation is converted into sensible heat, which results in warming-up the PV elements. It is well known that this increase in temperature leads to a reduction of the PV efficiency [1]. In case of land based PV installations, this is not so critical since these systems are ventilated by the wind, however, in building integrated PV systems (BIPV), this temperature effect can lead to a significant reduction in the electrical energy production. An attractive concept to minimise this temperature effect is to integrate the PV systems in buildings as double skin ventilated façades or rooftops and to use the heating-up of the elements for generating a buoyancy effect within the ventilated air gap. Although in recent years some shining examples of newly constructed buildings have shown the benefits of this strategy [2], the spread of this technology has not occurred at the necessary

* Corresponding author. Tel.: +34 973003711; fax: +34 973003575.
E-mail address: daniel.chemisana@macs.udl.cat (D. Chemisana).

1359-4311/$ – see front matter © 2013 Elsevier Ltd. All rights reserved.
http://dx.doi.org/10.1016/j.applthermaleng.2013.03.056

Nomenclature

A	aspect ratio of the parallel-plate duct (−)
RE	relative error, RE $= 100(y_p - \widehat{y}_p)/y_p$
b	width of the vertical parallel-plate duct (m)
C_p	specific heat capacity of the air (J/kg K)
CP	coefficient of pressure (−)
D_h	hydraulic diameter (m)
f_{app}	apparent friction factor (−)
g	gravitational acceleration (m/s^2)
G	buoyancy term (−), $G = 2SGr_{Dh}/Pr$
Gr	Grashof number (−)
H	height of the vertical parallel-plate duct (m)
I	identity matrix (−)
H^+	dimensionless height (−), $H^+ = H/2b\mathrm{Re}$
k	thermal conductivity (W/m K)
n	number of measured data
$\mathbf{n}$	unitary vector
NMBE	normalized mean bias error, NMBE $= 100\sum_{p=1}^{n}(y_p - \widehat{y}_p)/n\overline{y}$
$\overline{Nu}$	average Nusselt number (−)
P	pressure
Pr	Prandtl number (−)
ΔP_w	hydraulic pressure losses (Pa)
q_w	specific heat flux (W/m^2)
Q	air flow rate (m^3/s)
r_h	heat flux ratio, $r_h = q_{wc}/q_{wh}$
R_k	convergence ratio
Ra'_b	modified Rayleigh number for uniform wall temperature (−), $Ra'_b = (\rho^2 g\beta C_p \Delta T b^4)/\mu k H$
Ra''_b	modified Rayleigh number for uniform heat flux boundary conditions (−) $Ra''_b = (\rho^2 g\beta C_p q w b^4)/\mu k^2 H$
Re	Reynolds number based on hydraulic diameter (−)
t	time
$\mathbf{t}$	stress tensor
T	temperature (°C)
ΔT	temperature difference (°C), $\Delta T = (T_w - T_{air})$
$\mathbf{u}$	velocity vector (m/s)
u	horizontal velocity component (m/s)
v	vertical velocity component (m/s)
V	wind velocity (m/s)
y	measured data
$\widehat{y}$	simulated or predicted data
$\overline{y}$	mean value

Greek letters

β	coefficient of thermal expansion (°C^{-1})
δ	numerical error
ε	residual, $\varepsilon = y_p - \widehat{y}_p$
$\overline{\varepsilon}$	mean of residuals
μ	dynamic viscosity (Pa s)
ν	kinematic viscosity (m^2/s)
ρ	air density (kg/m^3)
σ	standard deviation
σ^2	variance

Subscripts

air	ambient air
b	relative to air gap width
c	cold wall
Dh	hydraulic diameter
D	Dirichlet condition
fd	fully developed
h	hot wall
i	inlet
N	Neumann condition
o	outlet
p	position in the data series
$plate$	parallel-plate duct
w	wall

scale. One of the reasons may have to do with the high complexity of evaluating the heat transfer processes which occur within the ventilated air gap. More specifically, the main drawback to overcome concerns the evaluation of the convective heat transfer coefficients and the air mass flow rate. Unless sophisticated predictive tools such as Computational Fluid Dynamics codes (CFD) or Artificial Neural Networks [3], most of the existing transient dynamic prediction models use mathematical correlations which relate these two variables with the corresponding dimensionless numbers and the air flow regimes (natural, forced and mixed convection). In the previous decades forced convection in air channels have been extensively analysed by several authors. Earlier studies were carried out by Filonenko [4] and [5]. They were extended to annular passages by Heaton et al. [6] and to flat plates and tubes by Churchill and Ozoe [7]. Asymmetry in the boundary conditions was analysed by Kakaç et al. [8,9] and more recently by Nield [10]. These correlations are valid for both laminar and turbulent situations and can be applied to wide or narrow double skin photovoltaic façades. Free and mixed convection have been also extensively analysed in literature. Earlier research in this field was carried out by Aung W. et al. [11], who included the analysis of asymmetric boundary conditions in the walls. Numerical solutions for the velocity and temperature distribution as well as correlations of $\overline{Nu}$ were obtained. Concerning the air mass flow rate, no correlations were obtained. Olsson C. [12] carried out a detailed analysis of the existing correlations for the $\overline{Nu}$ and the air mass flow rate for vertical parallel plates under laminar buoyancy driven flow. Cases with uniform wall temperatures and uniform heat fluxes were analysed and some correlations for symmetrical situations were suggested. The situations with asymmetric boundary conditions were not analysed. In 2012, Lau et al. [13] conducted a detailed analysis of natural convection in vertical channels by combining indoor experiments and numerical approximation based on Large-eddy simulations (LES) scheme. A new correlation for asymmetric uniform heat flux with adiabatic wall, under turbulent regime, was obtained. Several authors [14,15] obtained a dynamic transient model able to predict the thermal performance of double skin PV systems. This model considered a fixed value for the air mass flow rate. Concerning the convective heat transfer, the authors assumed a mixed convection situation with symmetrical $\overline{Nu}$. Following these investigations, Fux [16] made some improvements to the previously defined dynamic model and proposed a new correlation for mixed convection flows which is valid for symmetrical uniform boundary conditions and for low asymmetry levels. More authors [17–19], followed a different approach based on the estimation of the air mass flow rate as superposition of the buoyancy and the wind effect. This methodology assumed the velocity profile to be always symmetric and fully developed, therefore, the error in the air mass flow rate increased at higher heat flux and asymmetrical boundary conditions. The convective heat transfer coefficients were obtained through weighted functions of the situations with adiabatic wall at the coldest side. The mathematical expressions of

these functions lead to some discontinuities when the uniform heat fluxes at each wall approach zero. More sophisticated methods, based on finite volume discretization, were developed by Saelens et al. [20]. In these studies, the air channel is modelled through a transient one-dimensional algorithm in the vertical direction. The asymmetry effect was treated using the superposition methodology defined by Kakaç et al. [8]. This methodology also presented some discontinuity problems. A software code based on finite volume discretization combined with the step-by-step method to obtain the velocity, temperature and pressure at the outlet of each control volume, was developed by Faggembauu et al. [21]. Symmetric uniform wall temperatures were considered and the convective heat transfer coefficients were obtained from the Gnielinsky correlations [22]. Recently, Ghadamian et al. [23] developed a heat and mass transfer model for natural ventilated double skin façades based on finite volume discretization. Uniform wall temperatures and heat fluxes were considered and the convective heat transfer coefficients were obtained from empirical correlations with symmetric boundary conditions [24]. In most of these previous studies, two predominant situations were considered for the boundary conditions: symmetric boundary conditions and asymmetric boundary with adiabatic wall at the coldest side. These boundary conditions are very common when the double PV skins are formed by opaque PV panels at the outer skin and an opaque wall at the inner side. Nevertheless, in the case of double skins formed by semi-transparent PV panels, the short wave solar radiation crosses the transparent layers among the PV cells and heats the inner wall, leading to asymmetric boundary conditions situation. As mentioned previously, this situation was faced by Aung et al. [11], however, no expressions for the heat transfer coefficient of each wall were obtained. The mathematical correlations obtained by Brinkworth [17–19] present some discontinuities which clearly invalidate their use within iterative dynamic software tools. This paper aims at increasing the knowledge of the heat transfer processes which occur in these situations by means of a detailed analysis of the valid range of the existing mathematical correlations and by providing an evaluation of the effect of the asymmetry in the wall boundary conditions. A Computational Fluid Dynamics code (CFD), based on finite elements approach, has been used as the basic tool to calibrate the accuracy of each mathematical correlation.

2. Overview of existing mathematical correlations for double skin PV

2.1. Mathematical correlations for the average Nusselt number

This section gives a brief overview of the existing correlations of $\overline{Nu}_b$ in naturally ventilated vertical cavities. The vertical walls can be either isothermal for the uniform wall temperature boundary condition (UWT) or isoflux for the uniform heat flux boundary condition (UHF). The considered mathematical correlations are only valid for the laminar regime. Mathematical correlations for the cases where the boundary conditions are symmetric UWT and for the cases with asymmetric UWT with an adiabatic wall at the coldest side are summarised in Table 1.

In cases with UHF, the $\overline{Nu}_b$ can be defined in terms of the mean temperature of each vertical wall $\overline{T}_w$, the temperature at middle height, $T_{H/2}$, or the temperature at the top of the wall, T_H. The mathematical correlations for cases with symmetric UHF and for the cases with asymmetric UHF with one adiabatic wall at the coldest wall are summarised in Table 2. They are all valid for a range of $Ra''_b \leq 1 \cdot 10^5$.

In the cases where the boundary conditions are pure asymmetric, no mathematical correlations were found in literature.

2.2. Mathematical correlations for the air mass flow rate and the equivalent Reynolds number

As in the previous section, these correlations are only valid for the laminar regime and for a fixed geometry of a vertical parallel air duct in two dimensions. The boundary conditions at the vertical walls can be either UWT or UHF and the validity range is $Ra''_b \leq 1 \cdot 10^5$ in the case of UHF, and $Ra'_b \leq 1 \cdot 10^5$ in the case of UWT. The mathematical correlations for the cases where the boundary conditions are symmetric UWT and for the cases with symmetric UHF are summarised in Table 3.

Regarding the situations with asymmetric UHF or asymmetric UHF with an adiabatic wall at the coldest side, no correlations were found in literature.

3. Analysis of the Computational Fluid Dynamics (CFD) software package

3.1. Numerical model

The Computational Fluid Dynamics (CFD) software package used in this work is called ALYA and has been developed by Houzeaux et al. [25,26]. The numerical method is based on a stabilized finite element formulation (FEM). The analysis of vertical ventilated air gaps under free convection is governed by the incompressible Navier–Stokes equations. The buoyancy is accounted for using the Boussinesq approximation. The temperature transport equation is coupled with the momentum equation via this buoyancy term, and the resulting system of equations is called Boussinesq system. The governing equations for laminar regime are summarised in Eqs. (1) and (2). The momentum and continuity equations are expressed as:

$$\nabla \mathbf{u} = 0 \tag{1}$$

$$\rho \frac{\partial \mathbf{u}}{\partial t} + \rho(\mathbf{u}\cdot\nabla)\mathbf{u} - 2\nabla[\mu\varepsilon(\mathbf{u})] + \nabla p = \rho \mathbf{f} \tag{2}$$

The symmetric velocity tensor is expressed as:

$$\varepsilon(\mathbf{u}) = \frac{1}{2}\left(\nabla \mathbf{u} + \nabla \mathbf{u}^T\right) \tag{3}$$

In Eq. (2), $\mathbf{f}$ is the force vector per unit mass.

Following the Boussinesq hypothesis, the force vector is expressed as:

$$\mathbf{f} = g\beta(T_{air} - T) \tag{4}$$

The boundary conditions are imposed on the boundary of the domain. They can be of Dirichlet or Neumann type, involving the velocity and the traction, respectively:

$$\mathbf{u} = \mathbf{u}_D \quad \text{on } \Gamma_D : \text{Dirichlet} \tag{5}$$

$$\sigma\cdot\mathbf{n} = \mathbf{t}_N \quad \text{on } \Gamma_N : \text{Neumann} \tag{6}$$

where $\mathbf{n}$ is the exterior normal and the Cauchy stress tensor is expressed as:

$$\sigma = -pI + 2\mu\varepsilon(\mathbf{u}) \tag{7}$$

The energy conservation equation is expressed by:

$$\rho C_p\left[\frac{\partial T}{\partial t} + \mathbf{u}\cdot\nabla T\right] - \nabla[k\nabla T] = 0 \tag{8}$$

In Eq. (8), Joule effects have been neglected. Boundary conditions of the temperature equation are defined as:

Table 1
Correlations of $\overline{Nu}$, UWT.

Authors	Proposed correlation	Comments	Valid range
Symmetric UWT			
[30]	$\overline{Nu_b} = \left(\frac{576}{(Ra'_b)^2} + \frac{2.873}{(Ra'_b)^{0.5}}\right)^{-0.5}$		$Ra'_b \le 1 \cdot 10^5$
[35]	$\overline{Nu_b} = 0.645(Ra'_b)^{0.25}$	–	$200 < Ra'_b < 2 \cdot 10^5$
[31]	$\overline{Nu_b} = [(\overline{Nu_{fd}})^{-1.9} + (\overline{Nu_{plate}})^{-1.9}]^{-1/1.9}$ $\overline{Nu_{fd}} = \frac{Ra'_b}{24}$ $\overline{Nu_{plate}} = c\overline{C}_l(Ra'_b)^{1/4}$ $\overline{C}_l = \frac{0.671}{\left[1+\left(\frac{0.492}{\mathrm{Pr}}\right)^{9/16}\right]^{4/9}}$	$c = 1.32$ and $c = 1.20$ give good agreement with experimental data. $c = 1.00$ is the asymptotic value for an insulated vertical plate	$Ra'_b \le 1 \cdot 10^5$
[12]	$\overline{Nu_b} = [(\overline{Nu_{fd}})^{-1.3} + (\overline{Nu_{plate}})^{-1.9}]^{-1/1.3}$ $\overline{Nu_{fd}} = \frac{Ra'_b}{24}$ $\overline{Nu_{plate}} = c\overline{C}_l(Ra'_b)^{1/4\cdot P}$ $P = 1 + (Ra'_b)^{-0.4}$ $\overline{C}_l = \frac{0.671}{\left[1+\left(\frac{0.492}{Pr}\right)^{9/16}\right]^{4/9}}$	The value of c is not clearly defined by the author	$Ra'_b \le 1 \cdot 10^5$
Asymmetric UWT with one adiabatic wall			
[30]	$\overline{Nu_b} = \left(\frac{144}{(Ra'_b)^2} + \frac{2.873}{(Ra'_b)^{0.5}}\right)^{-0.5}$		$Ra'_b \le 1 \cdot 10^5$
[36]	$\overline{Nu_b} = 0.667(Ra'_b)^{0.29}$		$200 < Ra'_b < 8 \cdot 10^4$

Table 2
Correlations of $\overline{Nu}$, UHF.

Authors	Proposed correlation	Comments
Symmetric UHF		
[30]	$\overline{Nu_{b,T_H}} = \left(\frac{48}{Ra''_b} + \frac{2.51}{(Ra''_b)^{0.4}}\right)^{-0.5}$ $\overline{Nu_{b,T_{H/2}}} = \left(\frac{12}{Ra''_b} + \frac{1.88}{(Ra''_b)^{0.4}}\right)^{-0.5}$	
[31]	$\overline{Nu_{b,\overline{T}_w}} = [(\overline{Nu_{fd}})^{-3.5} + (\overline{Nu_{plate}})^{-3.5}]^{-1/3.5}$ $\overline{Nu_{fd}} = 0.29(Ra''_b)^{1/2}$ $\overline{Nu_{plate}} = c\overline{H}_l(Ra''_b)^{1/5}$ $\overline{H}_l = \frac{6}{5}\cdot\left(\frac{\mathrm{Pr}}{4+9\sqrt{\mathrm{Pr}}+10\mathrm{Pr}}\right)^{1/5}$	$c = 1.15$ and $c = 1.07$ give good agreement. $c = 1.00$ is the asymptotic value for an isolated vertical plate
[33]	$\overline{Nu_{b,\overline{T}_w}} = \left(\frac{185}{(H/b)^5} + (23Ra''^{-1.3}_b + 0.5Ra''^{-0.6}_b)^{-1.25}\right)^{0.2}$	The first term quantifies the increase in Nusselt number due to pure diffusion effect.
Asymmetric UHF with an adiabatic wall		
[30]	$\overline{Nu_{b,T_H}} = \left(\frac{24}{Ra''_b} + \frac{2.51}{(Ra''_b)^{0.4}}\right)^{-0.5}$ $\overline{Nu_{b,T_{H/2}}} = \left(\frac{6}{Ra''_b} + \frac{1.88}{(Ra''_b)^{0.4}}\right)^{-0.5}$	
[18]	Forced convection correlations could be used: $T^*_h = \frac{4}{\mathrm{Pr}}H^+ + \frac{2}{\overline{Nu}}$ $T^*_c = \frac{4}{\mathrm{Pr}}H^+ - \frac{9}{13\cdot\overline{Nu}}$ $H^+ = \frac{H}{2b\mathrm{Re}}$ $\overline{Nu} = n_2 + \frac{n_1}{H^+}$ Fully developed flow: $\overline{Nu} = 5.385$ Developing flow: [6] $n_2 = 5.385$; $n_1 = 0.07$. $H^+ > 0.001$ [9] $n_2 = 5.385$ and $n_1 = 0.015$. $H^+ > 0.01$	$T^* = \frac{(T_w - T_o)K}{q_{wh}b}$ q_{wh} = heat flux at the hot wall.

Table 3
Correlations of air mass flow rate and *Re*.

Authors	Proposed correlation	Comments
Symmetric UWT		
[12]	$\mathrm{Re} = \frac{2}{\mathrm{Pr}}\left(\frac{1}{\left(\frac{4Ra'_b\mathrm{Pr}}{f_{app}}\left(\frac{H}{b}\right)\right)^{0.81/2}} + \frac{1}{\left(6.6(Ra'_b)^{1/4}\mathrm{Pr}^{1/4}\left(\frac{H}{b}\right)\right)^{0.81}}\right)^{-1/0.81}$ $f_{app}\mathrm{Re} = 4\left[\frac{3.44}{(H^+)^{1/2}} + \frac{24+\frac{0.674}{(4H^+)}-\frac{3.44}{(H^+)^{1/2}}}{1+2.9\cdot10^{-5}(H^+)^{-2}}\right]$	The friction factor, f_{app}, was obtained by Refs. [8,9]
Symmetric UHF		
[17–19,34]	$G(H^+)^3 + B(H^+)^2 - \frac{1}{2}[(f_{app}\mathrm{Re})H^+ + \sum K_h] = 0$ $G = \frac{2SGr_{Dh}}{\mathrm{Pr}}$ buoyancy term $S =$ stratification coefficient $\approx$0.0 to 1.0 $B = \frac{\Delta P_w D_h^4}{\rho v^2 H^2}$ wind effect term $\Delta P_w = \frac{1}{2}CP_i V_i^2 - \frac{1}{2}CP_o V_o^2$ $f_{app}\mathrm{Re} = 96 + \frac{0.674}{H^+}$ friction term Once the H^+ is obtained: $\dot{m} = \frac{H}{b}\frac{\mu}{4H^+}$ (kg/s m)	$f_{app}Re$ is based on forced convection correlations obtained by Ref. [8]
[12]	$\mathrm{Re} = \frac{2}{\mathrm{Pr}}\left(\frac{1}{\left(\frac{4Ra''_b\mathrm{Pr}}{f_{app}}\left(\frac{H}{b}\right)^2\right)^{2.4/3}} + \frac{1}{\left(1.5(Ra''_b)^{1/5}\mathrm{Pr}^{1/5}\left(\frac{H}{b}\right)\right)^{2.4}}\right)^{-1/2.4}$ $f_{app}\mathrm{Re} = 4\left[\frac{3.44}{(H^+)^{1/2}} + \frac{24+\frac{0.674}{(4H^+)}-\frac{3.44}{(H^+)^{1/2}}}{1+2.9\cdot10^{-5}(H^+)^{-2}}\right]$	The exponents are based on experimental results obtained by Refs. [32,33]. The friction factor, f_{app}, was obtained by Refs. [8,9]

$$T = T_D \quad \text{on } \Gamma_D : \text{Dirichlet} \tag{9}$$

$$k\nabla T\cdot\mathbf{n} = q_N \quad \text{on } \Gamma_N : \text{Neumann} \tag{10}$$

3.2. Geometry

Fig. 1 shows the 2D geometry used to carry out the CFD simulations. It is formed by two vertical parallel smooth plates. The aspect ratio is defined as: $A = H/b$. The analysed aspect ratios and their corresponding sizes are: a) $A = 6$, $H = 0.3$ m, $b = 0.05$ m; b) $A = 12$, $H = 0.3$ m, $b = 0.025$ m; c) $A = 30$, $H = 0.3$ m, $b = 0.01$ m; d) $A = 80$, $H = 0.8$ m, $b = 0.01$ m; e) $A = 100$, $H = 0.6$ m, $b = 0.06$ m.

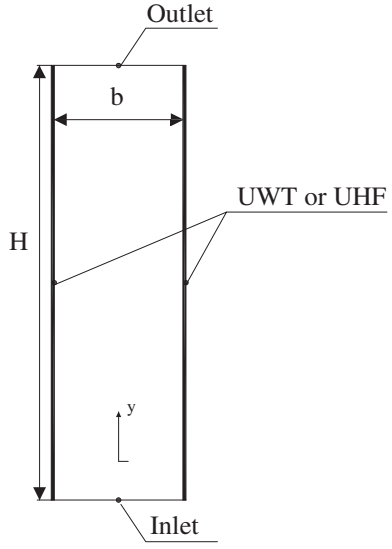

Fig. 1. Geometry of the vertical parallel-plate duct.

3.3. Numerical domains, finite element meshes and boundary conditions

Two computational domains were analysed. An artificial extension at the inlet is considered in one of the domains.

This artificial extension has a length of 0.1 m for aspect ratios of 6, 12 and 30 while a length of 0.3 m when the aspect ratios are 80 and 100. In order to choose the best approach, an evaluation of the effect of this extended domain was undertaken. One simulation for the aspect ratio of 12 and symmetric UWT was carried out for each domain. The calculated average Nusselt numbers were compared with the correlations obtained by Olsson [12]. The calculated air mass flow rates were compared with experimental results obtained by Salom [27]. In Table 4 an evaluation of each domain is carried out. As can be seen, in case of *Q*, the extended domain causes no variation in the relative error, however, in the case of the $\overline{Nu}_b$ there is a high reduction leading to the conclusion that a numerical domain with an artificial extension is needed to achieve higher accuracy in the simulations. This result is in coherence with conclusions about the effect of an extended domain over the thermal field prediction obtained by Pasut and De Carli [28].

Concerning the finite element meshes, structured meshes formed by quadrilateral elements were selected. Two examples of the meshes for the aspect ratio $A = 6$ are shown in Fig. 2. The meshes have been refined close to the walls and the entrance for allowing a better capturing of the boundary layer.

A sensitive analysis of the mesh size for each aspect ratio was undertaken. The calculated $\overline{Nu}_b$ and the air mass flow rate were compared with the correlations obtained by Olsson C. [12] and with

Table 4
Evaluation of the effect of an artificial extension at the inlet of the numerical domain ($A = 6$; $b = 0.025$; $Ra' = 617$; $T_h = 25$ °C; $T_c = 25$ °C; $T_i = 20$ °C).

Numerical domain	CFD		Olsson C. [12]	Salom J. [27]	RE (%)	
	$\overline{Nu}$ [−]	Q [m^3/s]	$\overline{Nu}$ [−]	Q [m^3/s]	$\overline{Nu}$ [−]	Q [m^3/s]
Without extension	3.332	0.0025	3.040	0.0026	−9.60	3.84
With extension	3.054	0.0025	3.040	0.0026	−0.46	3.84

the experimental results obtained by Salom J. [27]. As can be seen in Table 5, in the case of Q, a mesh size over 4000 finite elements has no effect. In case of $\overline{Nu}_b$ there are some variations in RE in both aspect ratios. To evaluate the effect of the mesh size, the methodology for verification defined by Stern et al. [29] is followed. Two aspect ratios of $A = 6$ and $A = 30$ are analysed. For each aspect ratio, meshes from 3000 to 24,000 elements are built. The convergence ratio, R_k, is calculated for the Nusselt number and for both aspect ratios obtaining values of $R_6 = -1$ and $R_{30} = 0$. The first value means that the mesh refinement follows an oscillatory convergence, while the second value means a monotonic convergence. For $A = 6$, the numerical error could not be determined, however, an evaluation of the uncertainty effect of the mesh refinement is determined. The uncertainty of increasing the mesh density from 3400 to 14,000 elements is 0.35%, and it decreases to 0.071% when the density increases by up to 22,400 elements. In the case $A = 30$, the numerical error for each mesh density level is obtained. It has a value of 0.5% when the mesh density increases from 4800 to 14,400 and has null value when the mesh density increases up to 24,000 elements.

No-slip boundary condition is applied on the walls of the air gap for the velocity field and Neumann or Dirichlet boundary conditions are applied for UHF or UWT cases respectively.

In the virtual walls of the extended domain an adiabatic boundary condition is imposed for the temperature and slip boundary conditions for the velocity field. At the entrance of the extended domain, a Dirichlet condition corresponding to the ambient temperature, is applied for the temperature field. In the case of the Navier–Stokes equations, a dynamic pressure boundary condition is imposed. This boundary condition is derived from the Bernoulli equation between the entrance and a reference point, with atmospheric pressure, placed at the infinity. The pressure is imposed iteratively via the traction using the average inlet velocity $\overline{\mathbf{u}}_i$:

$$p_i = -\frac{1}{2}\rho\overline{\mathbf{u}}_i^2 \tag{11}$$

$$\mathbf{t}_N = -p_i\mathbf{n} \tag{12}$$

This boundary condition was applied after comparing the results with the alternative of defining zero pressure at the entrance. As previously, the calculated $\overline{Nu}_b$ and Q were compared with the correlations obtained by Olsson C. [12] and with the experimental results obtained by Salom [27], respectively. For aspect ratio $A = 12$ and symmetric UWT of 40 °C, the effect of the dynamic pressure boundary condition decreased the RE from 19% to 8% in the case of Q and from 5% to 0.02% in the case of $\overline{Nu}_b$. The net effect of this boundary condition decreases the air mass flow rate by lowering the pressure at the inlet.

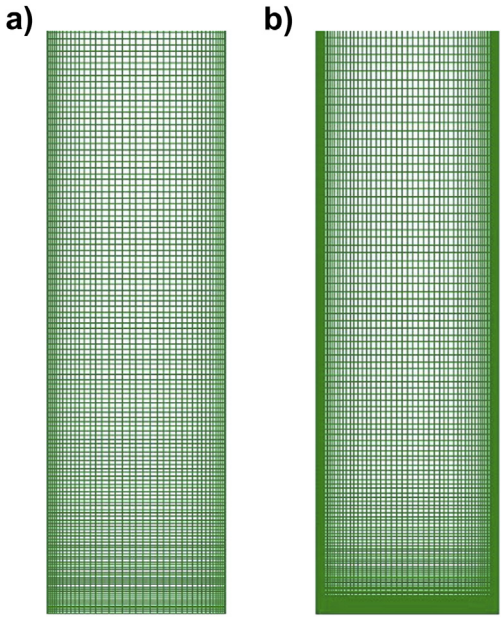

Fig. 2. Structured meshes for aspect ratio of $A = 6$. (a) Mesh formed by 10,000 elements and (b) mesh formed by 17,500 elements.

Table 5
Evaluation of the mesh size and the effect of mesh refinement ($A = 6$; $b = 0.05$; $Ra'_b = 19{,}766$; $T_h = 30$ °C; $T_c = 30$ °C and ($A = 30$; $b = 0.01$; $Ra'_b = 31.63$; $T_h = 30$ °C; $T_c = 30$ °C; $T_i = 20$ °C).

A	Number of finite elements	CFD		Olsson C. [12]	Salom J. [27]	RE (%)	
		$\overline{Nu}$ [−]	Q [m^3/s]	$\overline{Nu}$ [−]	Q [m^3/s]	$\overline{Nu}$ [−]	Q [m^3/s]
6	3400	6.84	0.0053	7.031	0.0052	2.72	−1.92
	14,000	6.89	0.0053	7.031	0.0052	2.01	−1.92
	22,400	6.88	0.0053	7.031	0.0052	2.15	−1.92
	24,000	6.89	0.0053	7.031	0.0052	2.01	−1.92
30	4800	0.86	0.0011	0.862	0.0011	0.23	0.00
	14,400	0.87	0.0011	0.862	0.0011	−0.93	0.00
	24,000	0.87	0.0011	0.862	0.0011	−0.93	0.00

3.4. Validation and verification of the numerical model using experimental results

In order to validate the accuracy of the numerical model and the assumed hypothesis, 400 simulations were carried out. The results of these simulations were compared with the experimental results obtained by Salom J. [27]. These experimental results were obtained using type K thermocouples for temperature measurements and Particle Image Velocimetry (PIV) technique for velocity measurements.

3.4.1. Validation of the velocity profiles

The vertical velocity profiles obtained through CFD simulations at a height $y = 0.15$ m and aspect ratio $A = 6$ are compared with those obtained by Salom J. [27], (see Fig. 3.1). Two cases with different Rayleigh number are analysed. The boundary conditions are symmetric UWT for the case of $Ra' = 19{,}776$ and asymmetric UWT for the case of $Ra' = 82{,}229$. As can be observed in Fig. 3.1, the velocity module increases with Ra'. The air mass flow rate can be calculated from the area defined by the velocity profile.

Fig. 3.2 shows the comparison of the vertical velocity profiles obtained through CFD simulations with those obtained by Salom J. [27] at a height $y = 0.15$ m and aspect ratio $A = 12$. Three cases with different Rayleigh number and symmetric UWT are analysed.

Fig. 3.3 shows the comparison of the vertical velocity profiles obtained through CFD simulations with those obtained by Salom J. [27] at a height $y = 0.15$ m and aspect ratio $A = 12$. Three cases with different Rayleigh number are analysed. The boundary conditions are asymmetric UWT for the three cases.

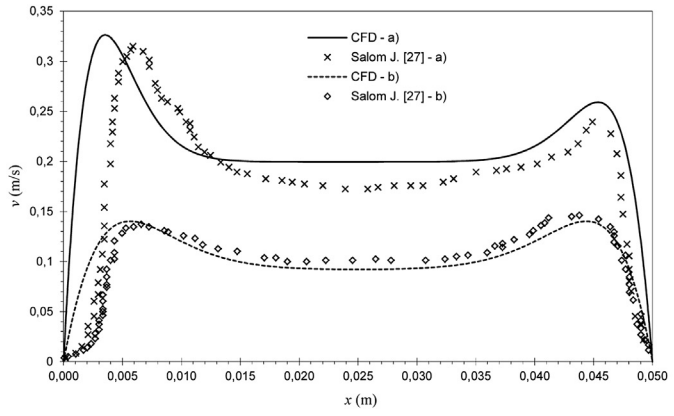

1

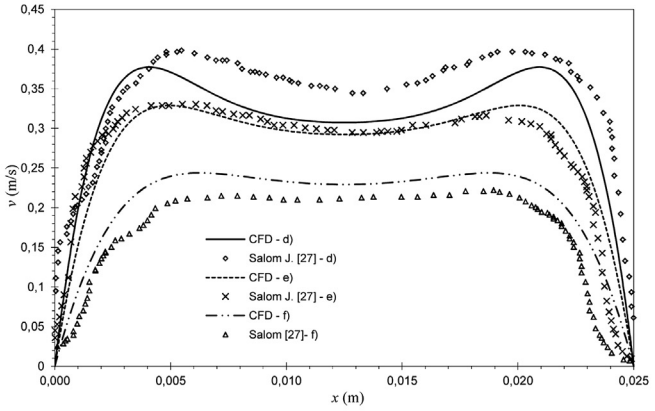

2

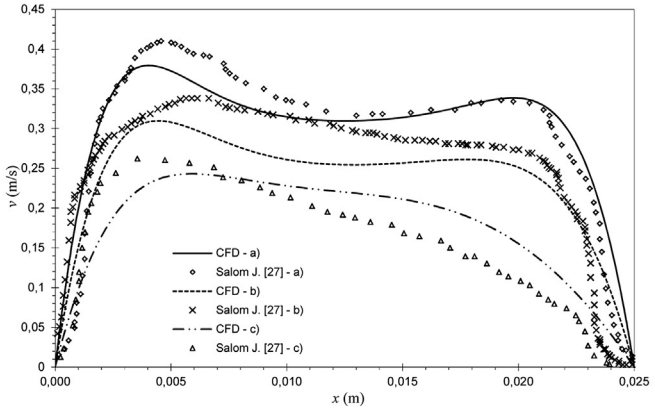

3

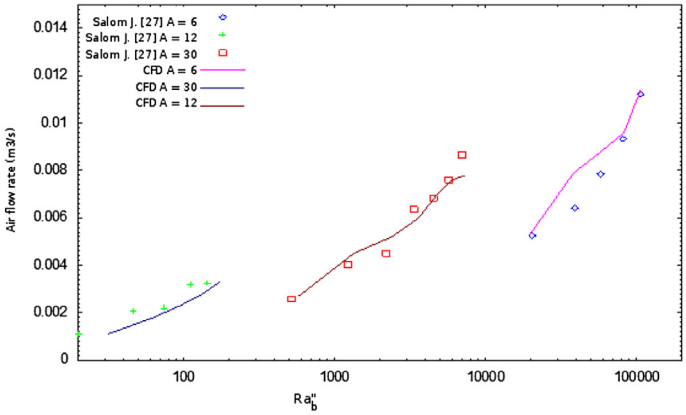

4

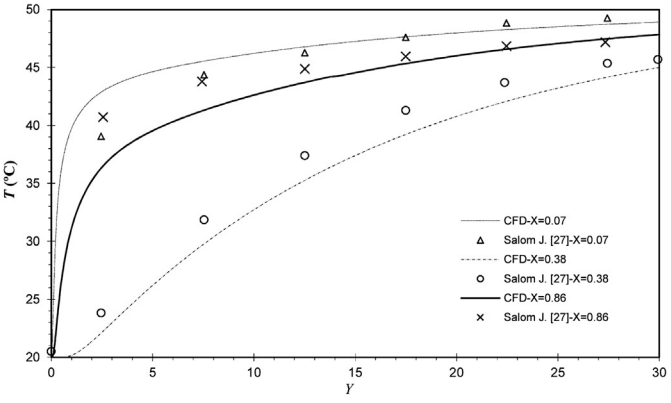

5

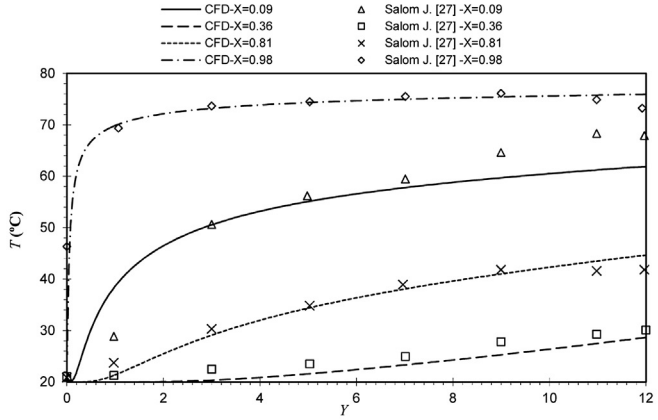

6

Fig. 3. (1) Velocity profiles at height $y = 0.15$ m. $A = 6$; $b = 0.05$. (a) $Ra_b^{'} = 82{,}229$; $T_h = 75$ °C; $T_c = 50$ °C; $T_i = 20.9$ °C. (b) $Ra_b^{'} = 19{,}766.6$; $T_h = T_c = 30$ °C; $T_i = 20$ °C. (2) Velocity profiles at height $y = 0.15$ m. $A = 12$; $b = 0.025$. (d) $Ra_b^{'} = 7350$; $T_{wh} = T_{wc} = 80$ °C; $T_i = 20.5$ °C. (e) $Ra_b^{'} = 4811$; $T_h = T_c = 60$ °C; $T_i = 21.05$ °C. (f) $Ra_b^{'} = 2397$; $T_h = T_c = 40$ °C; $T_i = 20.6$ °C. (3) Velocity profiles at height $y = 0.15$ m. $A = 12$; $b = 0.025$. (a) $Ra_b^{'} = 6036$; $T_h = 80$ °C; $T_c = 60$ °C; $T_i = 21.14$ °C. (b) $Ra_b^{'} = 3619$; $T_h = 60$ °C; $T_c = 40$ °C; $T_i = 20.7$ °C. (c) $Ra_b^{'} = 1347$; $T_h = 40$ °C; $T_c = 25$ °C; $T_i = 21.6$ °C. (4) Comparison between numerically calculated air flow rates and those determined experimentally, Salom [32]. Symmetric UWT. (5) Temperature profiles in several vertical sections ($A = 30$; $Ra_b^{'} = 94.88$; $b = 0.01$ m; $T_h = T_c = 50$ °C; $T_i = 20$ °C). (6) Temperature profiles in several vertical sections ($A = 12$; $Ra_b^{'} = 7412.5$; $b = 0.025$ m; $T_h = T_c = 80$ °C; $T_i = 20$ °C).

Table 6 shows a summary of the residuals analysis for the velocity profiles. As can be observed, for each aspect ratio both the standard deviation and the mean of residuals perform better for lower Rayleigh numbers. The NMBE is always smaller than ±2%. These values are within the acceptable range defined by Stern et al. [29] meaning that the CFD code and the numerical hypothesis can be considered as verified and validated for the velocity profiles.

3.4.2. Validation of the volumetric air flow rate

Salom J. [27] also obtained the volumetric air flow rate for the same experimental measurements of Section 3.4.1. Fig. 3.4 shows

Table 6
Analysis of the residuals for the vertical velocity profile. Values obtained from CFD simulations and values determined experimentally Salom J. [32].

A [−]	b [m]	$Ra_b^{'}$ [−]	σ [m/s]	σ^2 [(m/s)^2]	$\bar{\varepsilon}$ [m/s]	NMBE [%]
6	0.05	8,2229	0.0804	0.0065	−0.0540	−0.9556
	0.05	19,766	0.0285	0.0008	−0.0095	−0.0822
12	0.025	6036	0.0380	0.0014	−0.0135	−0.3614
	0.025	3619	0.0394	0.0016	0.01248	0.2918
	0.025	1347	0.0285	0.0008	−0.0073	−0.1052
	0.025	7350	0.0465	0.0022	0.0474	1.3860
	0.025	4811	0.0368	0.0014	0.0008	0.0198
	0.025	2397	0.0265	0.0007	−0.0185	−0.2630

the comparison between the numerical results and the experimental ones. Only symmetrical UWT were compared. The results show a very good agreement and the highest RE is 10%.

3.4.3. Validation of the temperature profiles

A comparison between the vertical temperature profiles obtained through numerical simulations and the measurements carried out by Salom J. [27] are shown in Fig. 3.5 and .6. The length variables are expressed in dimensionless form, $Y = y/b$ and $X = x/b$.

Table 7 shows a summary of the residuals analysis for the temperature profiles. The highest RE reaches 7.4% which is slightly bigger than the acceptable range of 5% [29]. As stated by Salom J. [27], these differences may be due to the difficulty of obtaining a steady state situation during the experimental measures and to the accuracy in the positioning of the temperature sensors. Assuming these experimental errors, the CFD code is considered as properly validated and the numerical hypothesis is verified for the vertical temperature profiles.

4. Evaluation of the existing average Nusselt number correlations

This section evaluates the correlations of $\overline{Nu}$ defined in Section 2.1. A comparison of each correlation with the results obtained from the CFD simulations is carried out for each wall boundary condition. The comparison of the $\overline{Nu}_b$ for symmetric UWT is shown in Fig. 4.1. It can be seen that the differences among the correlations and the CFD results are relatively small and they increase for higher Rayleigh numbers. The correlation which better fits the numerical results is the correlation of Rohsenow, modified by Olsson C. [12], using a coefficient $c = 1.10$. A correlation plot between the CFD results and this correlation shows a good linear dependence with a coefficient of determination of $R^2 = 0.9997$.

The comparison of $\overline{Nu}_b$ for asymmetric UWT with adiabatic wall at the coldest side is shown in Fig. 4.2. In this case, the differences among the correlations increase for very low Rayleigh numbers while for higher values, they are almost negligible. The correlation which better approximates the numerical results is the correlation of [30]. A correlation plot between numerical values and the values obtained with this correlation shows a good linear dependence with a coefficient of determination of $R^2 = 0.9975$.

Table 7
Analysis of the residuals for the vertical temperature profile. Values obtained from CFD simulations and values determined experimentally Salom J. [32].

A [−]	b [−]	$Ra_b^{'}$ [−]	X [−]	σ [°C]	σ^2 [°C^2]	$\bar{\varepsilon}$ [°C]	RE [%]
30	0.01	94.88	0.07	3.3541	11.2502	0.0982	2.6657
	0.01	94.88	0.38	0.4977	0.2477	0.4952	1.7805
	0.01	94.88	0.86	3.1002	9.6113	1.4582	6.2924
12	0.025	7412.50	0.09	5.0952	25.9606	1.5559	1.8063
	0.025	7412.50	0.36	0.4869	0.2371	1.7030	7.3634
	0.025	7412.50	0.81	1.7327	3.002	0.2287	1.8254
	0.025	7412.50	0.98	1.3555	1.8374	−0.1023	0.0715

As observed in Section 2.1, in cases where UHF are imposed, three reference temperatures can be used to define the $\overline{Nu}_b$. A comparison among the numerical simulations results and the relevant correlations for symmetric UHF is shown in Fig. 4.3. There are two correlations which better approximate the numerical results: the correlation of Ref. [31], with coefficient $c = 1.15$ and the correlation of Ref. [30]. The correlation plot between these two correlations and the numerical values shows a very good agreement in both cases with coefficients of determination of $R^2 = 0.9974$ and $R^2 = 0.997$ respectively.

A comparison among the numerical simulation results and the relevant correlations for asymmetric UHF with an adiabatic wall at the coldest side is shown in Fig. 4.4 (see Section 2.1). As it can be seen, the correlation which better fits the numerical results is the correlation of Ref. [30] with respect to the temperature in the middle of the channel $T_{H/2}$. The correlation plot between these correlations and the numerical values shows a very good agreement, with a coefficient of determination of $R^2 = 0.9965$.

As mentioned in Section 2.1, Brinworth [18] obtained other correlations for the dimensionless wall temperatures T_c^* and T_h^*, based on the expression of the Nusselt number depending on the dimensionless height H^+. In Fig. 5 a comparison with the CFD results is shown. The numerical values of T_c^* and T_h^* were calculated as the inverse of the $\overline{Nu}_b$ using the temperature at the end of the wall, T_H. As can be seen, the mathematical expression of T_h^* fits very well the numerical values. The correlation plot gives a high linear dependence with a coefficient of determination of $R^2 = 0.9981$. However, the correlation of T_c^* fits very well for Grashof numbers less than 10^5, with a coefficient of determination of $R^2 = 0.9996$. For higher values there is a great deviation, confirming that this correlation is only valid for pure laminar situations.

A summary of the mathematical correlations of $\overline{Nu}_b$ which better fit the numerical results for the situations with symmetric boundary conditions or asymmetric with an adiabatic wall, is showed in Table 8.

In the cases of pure asymmetric UHF, there are no correlations in literature for $\overline{Nu}_b$. To analyse these situations, two independent dimensionless numbers were considered $\overline{Nu}_h$ and $\overline{Nu}_c$. Starting with the hot wall, in Fig. 6.1 a comparison between the CFD results of $\overline{Nu}_h$ and the correlations of Ref. [30] for symmetric UHF and asymmetric UHF with adiabatic wall is shown. The numerical results always fit between both correlations, being the upper limit the correlation for the asymmetric UHF with adiabatic wall and the lower limit the correlation for symmetric UHF. The two correlations and the CFD solutions converge in a single line for $Ra_b'' > 1000$. This means a performance of almost isolated walls and no interaction between the two boundary layers. Nevertheless, for Ra_b'' bellow this limit, the interaction between the two boundary appears. The cold wall cools down the temperature closed to the hot wall and causes an over increase of the $\overline{Nu}_h$. In Fig. 6.1, the squared points of CFD results with the same Ra_b'' but different $\overline{Nu}_h$ account for this cooling effect.

The same analysis can be carried out for the cold wall (Fig. 6.2). It can be observed that for $Ra_b'' > 1000$ the performance is the same than the hot wall. For Ra_b'' bellow this limit, the $\overline{Nu}_c$ is always lower than the values from the correlation for symmetric UHF. As previously mentioned, this is due to the interaction between the two boundary layers which cause an effect over the air close to the cold wall. The points with the same Rayleigh number and very small Nusselt number are those corresponding to very high values of uniform heat flux at the hot wall and very small at the cold wall. In this case, the hot wall warms up the air closed to the cold wall and thus reduce the heat transfer between the wall and the air, leading to a drastic reduction of $\overline{Nu}_c$.

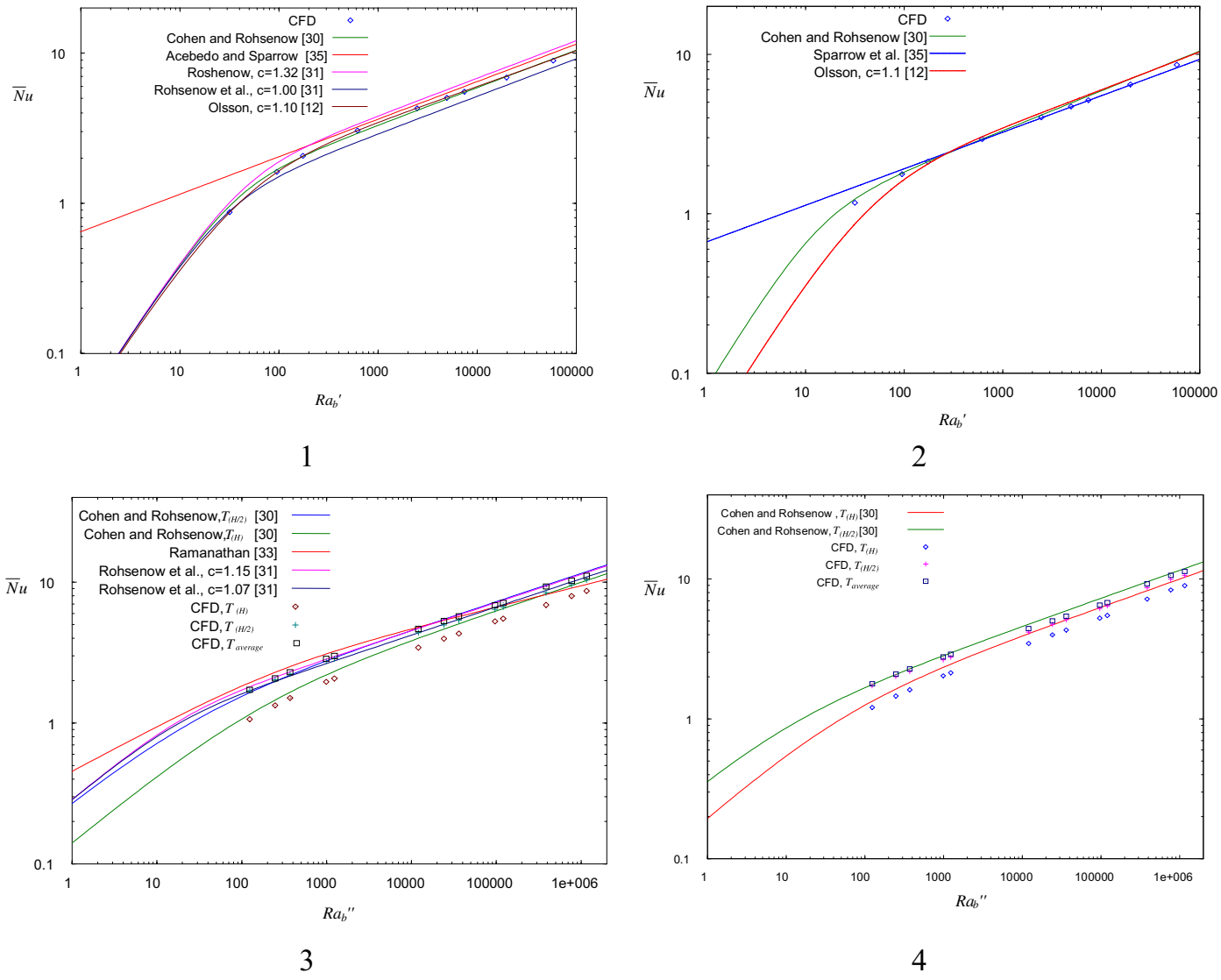

Fig. 4. Comparison of $\overline{Nu}$. (1) Symmetric UWT. (2) Asymmetric UWT with adiabatic wall. (3) Comparison of $\overline{Nu}$ for symmetric UHF. (4) Comparison of average Nusselt numbers for asymmetric UHF with adiabatic wall.

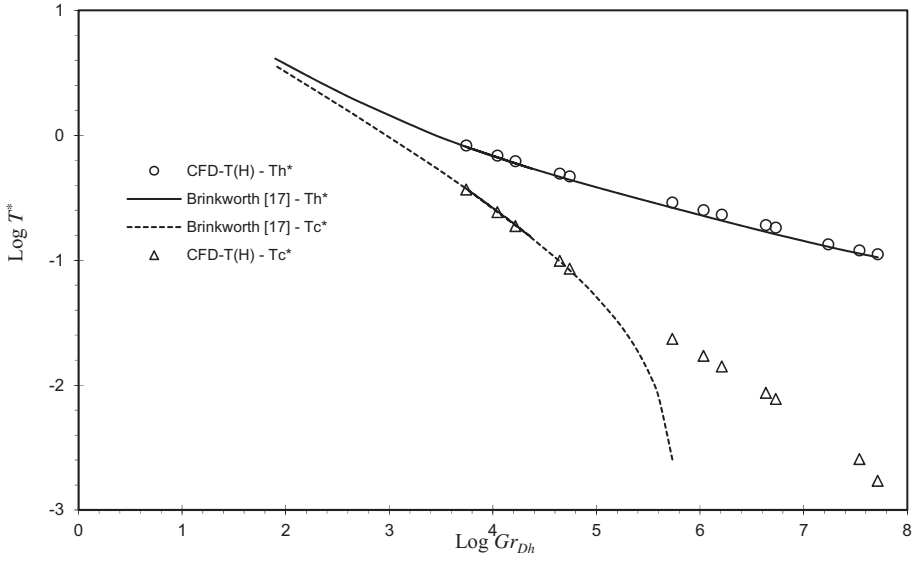

Fig. 5. Comparison of dimensionless wall temperatures for asymmetric UHF with adiabatic wall.

Table 8
Summary of the mathematical correlations which better approximate the numerical results for each boundary condition at the vertical walls.

$\overline{Nu}$				
	Symmetric UWT	Asymmetric UWT and adiabatic wall	Symmetric UHF	Asymmetric UHF and adiabatic wall
Rohsenow, modified by [12]; $c = 1.10$	✓	–	–	–
Rohsenow, modified by [12]; $c = 1.15$	–	–	✓	–
Cohen and Rohsenow [30]	–	✓	✓	✓
Air mass flow rate				
		Symmetric UWT		Symmetric UHF
Olsson C. [12]		✓		–
Brinkworth et al. [17–19,34]		–		✓

5. Evaluation of the existing average air mass flow rate and Reynolds number correlations

In this section, a comparison between the mathematical correlations of Section 2.2, the values obtained through the numerical simulations and the experimental measurements of Ref. [27] are carried out.

In the cases of symmetric UWT the correlation of Olsson C. [12], see Table 3, can be used. The comparison of this correlation, the numerical values and the experimental measurements of Ref. [27] is shown in Fig. 7.1

The correlation plot between the expression of Olsson C. [12] and the numerical values shows a very good agreement, with a coefficient of determination of $R^2 = 0.988$. In the cases of symmetric UHF, two correlations are summarised in Section 2.2. The first correlation is compared with the numerical results. This correlation models the relationship between H^+ and the Grashof number. Assuming a vertical linear variation of the average horizontal air temperature ($S = 0.5$), hydraulic losses coefficient of $\Sigma K_h = 1$ and the friction term based on the expression of Ref. [8], this correlation can be simplified as:

$$\frac{Gr_{Dh}}{0.71}\left(H^+\right)^3 - 48H^+ - 0.837 = 0 \tag{13}$$

Eq. (13) is solved using the Newton–Raphson method and the H^+ is obtained for each Grashof number. Fig. 7.2 shows the comparison between the H^+ obtained from Eq. (13) and the numerical results (CFD). The solutions of Eq. (13) approximate very well the numerical results obtained by the CFD simulations. The correlation plot gives a coefficient of determination of $R^2 = 0.9971$.

The second correlation for symmetric UHF, proposed by Olsson [12] (see Table 3), is compared with the numerical results (CFD) in Fig. 7.3. As it can be observed, there are significant deviations between this correlation and the results obtained from the numerical simulations, especially in the cases with large aspect ratios ($A = 6$).

These deviations were considered by Olsson C. [12] who argued that the coefficients and exponents of the correlation were determined based on experimental data obtained by Campo et al. [32,33]. These experiments provided a limited number of data to fit the correlations, therefore a general extension of this correlation may lead to significant deviations (see Fig. 7.3).

A summary of the mathematical correlations of the air mass flow rate which better fit the numerical results, for situations with symmetric boundary conditions is showed in Table 8.

As mentioned in Section 2.2 there are no correlations neither for asymmetric UHF with adiabatic wall at the coldest side nor for pure asymmetric UHF boundary conditions. Besides, there is an uncertainty about the limit of Rayleigh number over which the effect of asymmetry in the boundary conditions can affect the air flow pattern. Fig. 7.4 shows a comparison of the numerical results for cases with asymmetric UHF and the correlation obtained by Brinkworth [17–19,34]. It is depicted the calculated H^+ with respect to the buoyancy term G. As can be observed, the numerical results fit very well the equation of Ref. [17] for a range up to $G < 10^5$, which is equivalent to $Gr < 10^4$. Within this range, the effect of the asymmetry in the UHF is negligible and correlations for symmetric UHF can be also valid for asymmetric UHF conditions. However, within the range of $10^5 < G < 10^8$, which is the transition to turbulent region, the numerical results suffer dispersion because of the asymmetry in the heat fluxes. The cases with small heat flux ratios $r_h \sim 0.0$ (black rhombuses) fit very far from the mathematical correlation; while the cases with high heat flux ratios $r_h \sim 1.0$ (black circles) are very close to the correlation. This behaviour is probably due to the asymmetry in the boundary conditions which causes an asymmetry in the velocity profile and lead to higher values of H^+ than the ones expected for symmetric cases.

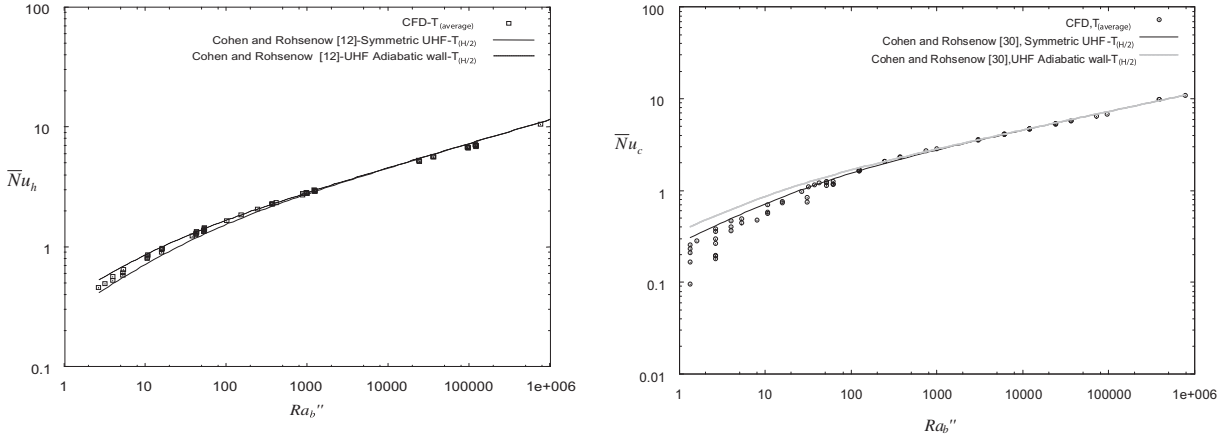

1 2

Fig. 6. Comparison of $\overline{Nu}_h$. (1) Cases with pure asymmetric UHF. (2) Cases with pure asymmetric UHF.

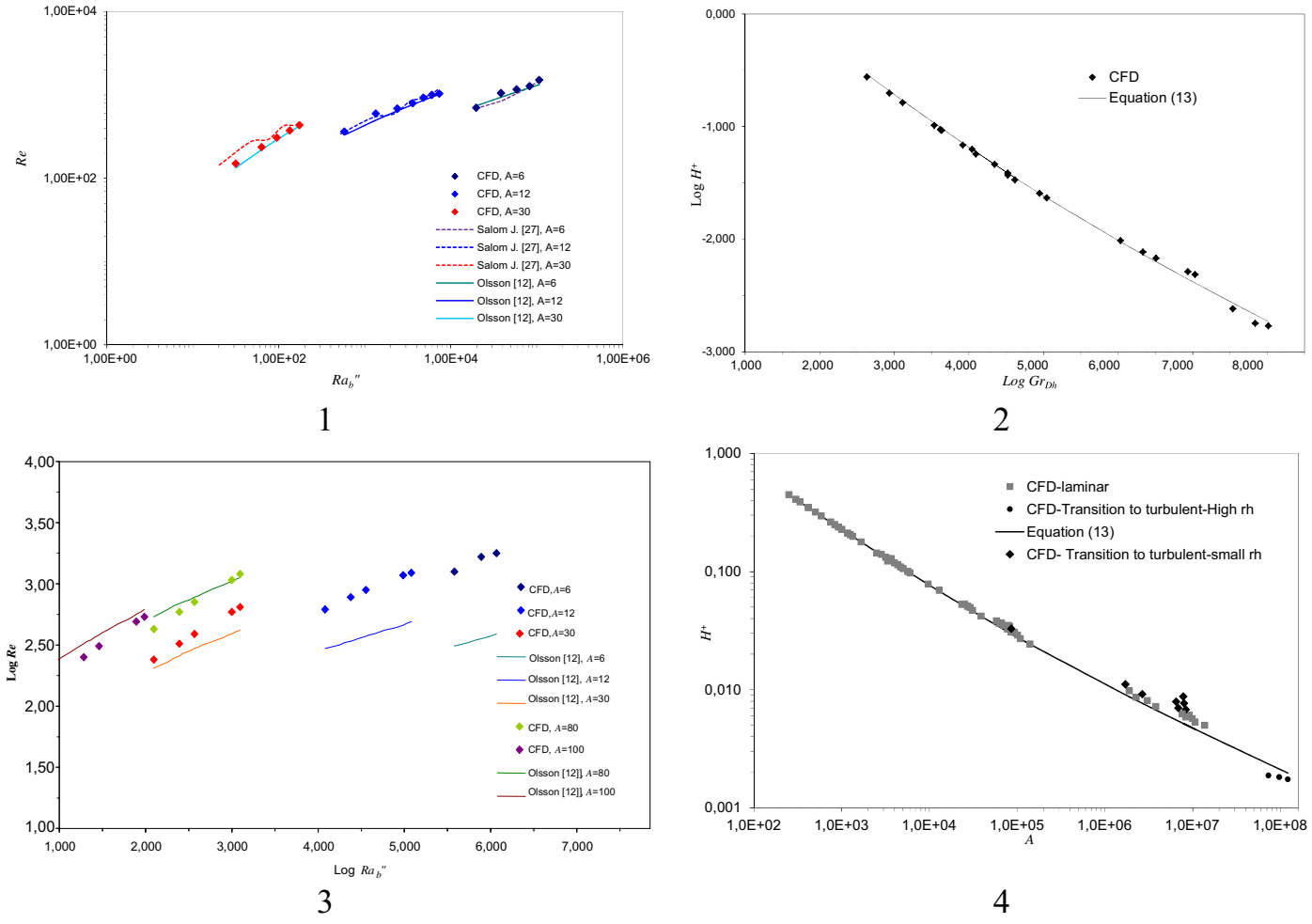

Fig. 7. (1) Cases with symmetric UWT. Comparison of *Re* calculated numerically with the experimental results of Salom J. [27] and the correlation of Olsson C. [12]. (2) Cases with symmetric UHF. Comparison of H^+ obtained from Eq. (13) and the numerical results. (3) Cases with symmetric UHF. Comparison of *Re* calculated numerically with the correlation of Olsson C. [12]. (4) Cases with asymmetric UHF. Comparison among the H^+ values obtained by Brinkworth [17–19] and the numerical results.

6. Conclusions

In this paper, a specific numerical code, based on a stabilized finite element formulation (FEM), is used as the basic tool to evaluate the accuracy of the existing correlations for the $\overline{Nu}$ and the air mass flow rate in double skin PV façades.

A sensitive analysis on the proper size of the mesh for each aspect ratio has been undertaken showing that meshes in the range of 14,000 elements are enough to approach the problem.

The main conclusion of the physical hypothesis evaluation is that inlet modelling significantly affects the simulation results. It is found that the best modelling approach consisted in including an artificial extension at the inlet and applying a dynamic pressure boundary condition at the entrance of this extended domain.

The FEM code is able to describe the heat transfer processes occurring in double skin façades with integrated PV under natural convection and in laminar regime, showing NMBE within the acceptable range of 5% when velocity and temperature profiles are calibrated with experimental measures.

Once the FEM code was calibrated, an intensive numerical simulation campaign in the laminar and transition to turbulent range and for UHF and UWT boundary conditions, has been carried out. In the post-processing stage, the average Nusselt number for each wall and the air mass flow rate have been calculated and contrasted with the existing mathematical correlations.

In the case of the average Nusselt number and symmetric or asymmetric with adiabatic wall situations, at least one mathematical correlation for each boundary case fits the numerical results with a high precision. Table 8 shows the correlations which best fit the numerical results for each case.

In cases with pure asymmetric UHF there are no available mathematical correlations for the average Nusselt numbers. From the numerical results post process it can be observed that for $Ra_b'' > 1000$ there is no interaction between the boundary layers, therefore, existing mathematical correlations for symmetric UHF or for asymmetric UHF with adiabatic wall are both valid. For Ra_b'' below this limit, the two boundary layers interact and affect the temperatures of the air in contact with the walls. New mathematical correlations are necessary to model the convective heat transfer coefficient in this region.

Regarding the air mass flow rate, or the Reynolds number and cases of asymmetric UHF with adiabatic wall, no mathematical correlations were found in literature, therefore, further research to find suitable correlations for these situations is necessary.

For situations with pure asymmetric UHF, correlations for the air mass flow rate were neither found in literature. From the numerical results post process, it can be concluded that for a range $Gr < 10^4$ the effect of the asymmetry in the UHF is negligible and correlations for symmetric UHF can be also valid for pure asymmetric UHF conditions. Within the range of $10^4 < Gr < 10^7$, which is the

transition to turbulent region, it can be seen that the asymmetry in the boundary conditions clearly affect the air mass flow rate leading to higher velocities close to the hot wall. To properly model this effect, further research is necessary to find new suitable mathematical correlations.

References

[1] B. Marion, A method for modeling the current–voltage curve of a PV module for outdoor conditions. Progress in photovoltaics: research and applications, National Renewable Energy Laboratory 10 (2002) 205–210.
[2] H.A. Zondag, Flat-plate PV–thermal collectors and systems: a review, Renewable and Sustainable Energy Reviews 12 (2008) 891–959.
[3] X. Cipriano, J. Carbonell, J. Cipriano, Monitoring and modelling energy efficiency of municipal public buildings: case study in Catalonia region, International Journal of Sustainable Energy 28 (2009) 3.
[4] G.K. Filonenko, Hydraulic Resistance in Pipes, in: Heat Exchanger Design Handbook, vol. 1, Teploenergetica, Moscou, Soviet Union, 1954.
[5] W.H. McAdams, Heat Transmission, McGraw-Hill, New York, USA, 1954.
[6] H.S. Heaton, W.C. Reynolds, W.M. Kays, Heat transfer in annular passages. Simultaneous development of velocity and temperature fields in laminar flow, International Journal of Heat and Mass Transfer 7 (1964) 763–781.
[7] S.W. Churchill, H. Ozoe, Correlations for forced convection with uniform heating in flow over a plate and in developing and fully developed flow in a tube, Journal of Heat Transfer 95 (1973) 78–84.
[8] S. Kakaç, R.K. Shah, W. Aung, Handbook of Single-phase Convective Heat Transfer, John Wiley & Sons, New York, USA, 1987.
[9] R.K. Shah, A.L. London, Laminar Flow Forced Convection in Ducts. Advances in Heat Transfer, Academic Press, New York, USA, 1978.
[10] D.A. Nield, Forced convection in a parallel plate channel with asymmetric heating, International Journal of Heat and Mass Transfer 47 (2004) 5609–5612.
[11] W. Aung, L.S. Fletcher, V. Sernas, Developing laminar free convection between vertical flat plates with asymmetric heating, International Journal of Heat and Mass Transfer 15 (1972) 2293–2304.
[12] C.-O. Olsson, Prediction of Nusselt number and flow driven flow between vertical parallel plates, Journal of Heat Transfer 126 (2004) 97–103.
[13] G.E. Lau, G.H. Yeoh, V. Timchenko, J.A. Reizes, Numerical investigation of passive cooling in open vertical channels, Applied Thermal Engineering 39 (2012) 121–131.
[14] D. Infield, L. Mei, U. Eicker, Thermal performance estimation for ventilated PV facades, Solar Energy 76 (2004) 93–98.
[15] L. Mei, D. Infield, U. Eicker, F. Volker, Thermal modelling of a building with an integrated ventilated PV facade, Energy and Buildings 35 (2003) 605–617.
[16] V. Fux, Thermal Simulation of Ventilated PV Façades. Doctoral Thesis, Loughborough University, Loughborough, UK, 2006.
[17] B. Brinkworth, Estimation of flow and heat transfer for the design of PV cooling ducts, Solar Energy 69 (2000) 413–420.
[18] B.J. Brinkworth, A procedure for the routine calculation of laminar free and mixed convection in inclined ducts, International Journal of Heat and Fluid Flow 21 (2000) 456–462.
[19] B.J. Brinkworth, M. Sandberg, Design procedure for cooling ducts to minimise efficiency loss due to temperature rise in PV arrays, Solar Energy 80 (2006) 89–103.
[20] D. Saelens, S. Roels, H. Hens, Strategies to improve the energy performance of multiple-skin facades, Building and Environment 43 (2008) 638–650.
[21] D. Faggembauu, M. Costa, M. Soria, A. Oliva, Numerical analysis of the thermal behaviour of ventilated glazed facades in Mediterranean climates. Part I: development and validation of a numerical model, Solar Energy 75 (2003) 217–228.
[22] A. Bejan, K.D. Alla, Heat Transfer Handbook, John Wiley & Sons, New Jersey, USA, 2003.
[23] H. Ghadamian, M. Ghadimi, M. Shakouri, M. Moghadasi, M. Moghadasi, Analytical solution for energy modeling of double skin façades building, Energy and Buildings 50 (2012) 158–165.
[24] F.P. Incropera, P.D. DeWitt, Fundamentals of Heat and Mass Transfer, John Wiley & Sons, New York, USA, 1996.
[25] G. Houzeaux, R. Codina, A Dirichlet/Neumann domain decomposition method for incompressible turbulent flows on overlapping subdomains, Computational Fluids 33 (5–6) (2003) 771–782.
[26] G. Houzeaux, J. Príncipe, A variational subgrid scale model for transient incompressible flows, International Journal of CFD (2006).
[27] J. Salom, Numerical Simulation of Natural Convection Phenomena Using Domain Decomposition Techniques. Doctoral Thesis, Politechnical University of Catalonia, Terrassa, Spain, 1999.
[28] W. Pasut, M. De Carli, Evaluation of various CFD modelling strategies in predicting airflow and temperature in a naturally ventilated double skin façade, Applied Thermal Engineering 37 (2012) 267–274.
[29] F. Stern, R. Wilson, J. Shao, Quantitative V&V of CFD simulations and certification of CFD codes, International Journal for Numerical Methods in Fluids 50 (2006) 1335–1355.
[30] A.B. Cohen, W.M. Rohsenow, Thermally optimum spacing of vertical, natural convection cooled, parallel plates, Journal of Heat Transfer 106 (1984) 116–123.
[31] M. Rohsenow Warren, James P. Hartnett, Young I. Cho, Handbook of Heat Transfer, Mc Graw-Hill, New York, USA, 1998.
[32] A. Campo, B. Morrone, Numerical analysis of partially heated vertical parallel plates in natural convective cooling, Numerical Heat Transfer, Part A: Applications 36 (1999) 129–151.
[33] S. Ramanathan, R. Kumar, Correlations for natural convection between heated vertical plates, Journal of Heat Transfer 113 (1991) 97–107.
[34] B.J. Brinkworth, R.H. Marshall, Z. Ibarahim, A validated model of naturally ventilated PV cladding, Solar Energy 69 (2000) 67–81.
[35] L.F.A. Azevedo, E.M. Sparrow, Natural convection in open-ended inclined channels, Journal of Heat Transfer 107 (1985) 893–901.
[36] E.M. Sparrow, G.M. Chrysler, L.F. Azevedo, Observed flow reversals and measured-predicted Nusselt numbers for natural convection in a one-sided heated vertical channel, Journal of Heat Transfer 106 (1984) 325–332.

Experimental evaluation of the energy performance of semi transparent ventilated double skin photovoltaic components

J. Cipriano[a]*, C. Lodi[b], J. Carbonell [a], S. Danov [a], X. Cipriano [a], D. Chemisana[c],

[a] *Centre Internacional de Mètodes Numèrics a l'Enginyeria (CIMNE), Building Energy and Environment Group, c/Rambla St Nebridi 22 , 08222 Terrassa, Spain*

[b] *Energy Efficiency Laboratory (EELab), Department of Engineering "Enzo Ferrari", University of Modena and Reggio Emilia, via Vignolese 905/B, 41125 Modena, Italy*

[c] *Applied Physics Section of the Environmental Science Department, University of Lleida, c/Jaume II 69, 25001 Lleida, Spain*

* *Corresponding author: Centre Internacional de Mètodes Numèrics a l'Enginyeria (CIMNE), Building Energy and Environment Group. CIMNE-UdL Classroom. c/Pere de Cabrera s/n. CREA building. Office 1.15, 25001. Lleida, Spain. e-mail: cipriano@cimne.upc.edu, phone: +34 973003574, fax: +34 973003575*

Abstract

Experimental results of an extensive monitoring campaign on a ventilated double skin with integrated photovoltaic system are presented. Measurements have been carried out at the facilities of the Outdoor Test Reference Environment of Lleida (TRE-L) and both mechanical and natural ventilated situations have been extensively measured and analysed. The TRE-L facility allows testing integrated photovoltaic systems in outdoor conditions but with a controlled test environment. Several experiments, with different inclinations, ventilation regimes and rear facing materials, are performed and the corresponding energy balance analysis are carried out. A comprehensive sensitivity analysis on the influence of these factors over the thermoelectric performance of the PV system is presented and contributions to the revision of performance indicators of PV systems under real operating conditions are presented. The results serve to evaluate the trade-off between different design aspects of building integrated double skin PV ventilated systems.

Keywords: ventilated BIPV façades, monitoring campaign, sensitivity analysis, Test Reference Environment

1. Introduction

In order to achieve the requirements of the new EU directive on the energy performance of buildings (EPBD) [1], solar energy technologies integrated in the building envelopes need to be promoted. In particular, an attractive concept with great potential is the integration of photovoltaic (PV) systems in buildings as double skin ventilated facades or roofs. In these systems, both the electrical efficiency can be increased and the pre-heated air within the ventilated air gap can be used to reduce ventilation thermal losses and space heating or cooling demand of buildings. This approach combines electricity generation with other functions of the building envelope and it may contribute to the success in reaching the requirements set for nearly-Zero Energy Buildings (nZEB) by 2020.

Email address: cipriano@cimne.upc.edu, chiara.lodi@unimore.it, jordi@cimne.upc.edu, sdanov@cimne.upc.edu, xciprian@cimne.upc.edu ,daniel.chemisana@udl.cat (D. Chemisana[c],)

Double skin applications of Building Integrated Photovoltaic systems (BIPV) require a deep knowledge of the thermal and electrical characteristics of the system, mainly of the heat transfer process which occur within the ventilated air gap [2]. The technical data provided by the PV industry normally include only the electrical performance under Standard Test Conditions (STC) and measurements of Nominal Operating Cell Temperature (NOCT), as described in the IEC 61215 [3]. However, building designers and engineers require performance indicators of PV systems under real operating conditions for a typical climate, location and building integration situation. Some insights on the effect of the inclination, the air flow regime and the materials which form the rear side of these double skins, need to be obtained and provided to the European construction sector. Previous studies addressed this need through indoor experimental procedures [4, 5]. These procedures are normally accurate and replicable, however they do not take into account the dynamic variations in the boundary conditions of the components once they are integrated into a real building. On the other hand, experiences involving the measurements of double skin BIPV systems in real buildings [6, 7, 8, 9] revealed that these studies are expensive and problematic in achieving good quality data, isolating the performance of the individual components, and extending results to different buildings, occupancies and climates.

Therefore, controlled outdoor test facilities may be considered as an economical and practical intermediate bridge between laboratory tests and monitoring of real and occupied buildings. In these kind of controlled outdoor test environments, real climate effects are taken into account and high accuracy of the data is reached while avoiding occupancy effects. Some studies of the energy performance of BIPV in controlled outdoor test facilities have been found in literature. From the experience gained during several European projects [10], the first version of an outdoor Test Reference Environment (TRE) for mechanically ventilated double skin applications of BIPV systems was designed and built at the EC Join Research Centre (JRC) of Ispra [11]. The purpose of the experimental work at the TRE was to obtain several data series for the same PV module under different boundary conditions and to compare them with data series from other PV modules. Several experiments were carried out at the TRE, testing different PV module configurations under several air flow rates and studying the effect of transversal fins positioned along the air gap. Another example of outdoor experimental set-up of a solar chimney with solar PV systems is presented by Martí-Herrero [12]. In this work, a theoretical physical model of the solar chimney was developed and some simulations of the temperatures of the PV system and the air gap and and heat fluxes are obtained based on real data from the experimental set up. The main conclusion was that the solar chimney with thermal inertia and PV modules acts as natural ventilation system appropriate to Mediterranean climates mainly due to the nocturnal ventilation produced. More recently, an outdoor installation for measuring the energy performance of mechanically ventilated BIPV systems was installed at the Concordia University in Canada [13]. In this outdoor facility, two different PV module inclinations were tested (45 and 30 deg) and several forced air flow rates were performed. More recently, Park et. al.[14] performed an experimental analysis of thermal and electrical performance of a semi-transparent PV module in vertical position and under natural ventilated conditions. Some conclusions about decrease in the electrical efficiency due to temperature effects are found, however, only vertical position and one kind of rear facing material were analyzed. Olivieri et. al.[15]carried out an integral energy evaluation of semi transparent double skin façades and obtained some conclusions about the effect of transparency level in the energy performance of the PV systems.

This paper aims at extending these previous studies towards wider parametric evaluations. An improved version of the TRE was designed and built at the Lleida Outdoot Test Center (LOTCE) [16, 17, 18, 19]in 2009 and further improved in 2013 (see Fig. 1) and the results from the extended monitoring campaigns are presented herewith. Detailed analysis of the effect of different ventilation regimes, including natural ventilation, several inclinations and rear facing materials over the

energy performance of the double skin BIPV system are carried out and conclusions are presented. The performance of the ventilated PV module placed at the TRE-L is also compared with the performance of other two identical PV modules: one reference module which is fully insulated and another reference PV module which is kept under free-rack conditions.

The paper starts with the description of the experimental set-up. It follows the analysis of the experimental results and the evaluation of the overall energy performance of the component. Finally, conclusions are drawn and further developments are outlined.

2. Experimental set-up

2.1. Geometry and materials

The Test Reference Environment of Lleida (TRE-L) (see Figure 1) is composed by a wooden box with external sizes of 206 x 236 x 37 cm and a support structure which allows any inclination to be tested. The weather resistant wooden box is made by 2.2 cm thick white-painted plywood panels. In order achieve adiabatic conditions at the back side of the PV system, the TRE-L is filled in with an insulation layer of 20 cm thick of expanded polystyrene (EPS) with thermal conductivity of 0.031 W/m^{o}K. The TRE-L has a south-oriented opening where a glass-tedlar silicon PV module (with dimensions of 97.6 x 150.7 cm) was positioned. The tested PV module is formed by 28 mono crystalline silicon (m-Si) solar cells and it has a packing factor of 0.46. An air channel with the same height as the PV panel and 11.5 cm width, (aspect ratio of 13.6) is performed at the backwards of the PV module. Two ventilation situations can be tested: forced convection and natural convection. In the case of forced convection, the air enters from the bottom and is extracted from the top by means of a 12.5 cm diameter PVC tube, placed at the rear side of the box so that it remains shaded. A variable speed fan forces airflow at several airflow rates. An array of plastic made cylindrical tubes of 0.5 cm diameter and 0.5 m length are placed at the inlet to guarantee a non disturbed pattern flow.

a)  b) 

Figure 1: Test Reference Environment (TRE) of Lleida in the PCiTAL. a) front view; b) rear view

In the case of the natural ventilation situation, the array of cylindrical tubes is substituted by a wood made box which reduces the pressure losses but protect the inlet from wind effect. The variable speed is also removed from the outlet. The PV module is easily removable and the rear side of the air gap is then accessible. This allows for different rear facing materials to be installed. During the experiments two different rear facing materials were tested in the TRE-L: the ALANOD-Mirotherm absorber black sheet and the DuPont diffuse light reflector (DLR80). The Mirotherm

sheet has a solar absorption of 95 ± 1 % (in the range of wavelength between 380 and 1650 nm) and a thermal emission of 5 ± 2 % (in the range of wavelength between 3 and 20 μm). The DuPont white reflector has a light diffuse reflectivity of 96.3 % (averaged to all incidence angles).

Next to the TRE-L, other two reference modules, in vertical position, (see Fig. 1) are installed : one of them is leaved in free-rack conditions and the other one is fully insulated at the backside with a layer of 10 cm of EPS, thus avoiding convective and radiative thermal fluxes at the rear side.

2.2. Monitoring set up

The measurement set-up of the TRE-L is schematically shown in Fig. 2. It is formed by 32 sensors connected to a data logger (Campbell CR1000). The data are measured every 30 seconds and averaged on a 10-minute basis.

The following sensors have been used:

- 9 type J thermocouples to measure the air temperature at the air gap inlet (11r, 11s, 11t) and outlet (10w, 10y, 10z) and in correspondence of the middle of the air cavity (13f, 13h, 13j)
- 12 type J thermocouples to measure the surface temperature of the rear side of the PV module (1a, 1b, 1c, 1e, 2f, 2g, 2h , 2j, 3m, 3n, 3o, 3q)
- 6 type J thermocouples to measure the surface temperature of the rear facing material (4b, 4e, 5g, 5j, 6n, 6q)
- 1 type J thermocouple to measure the air temperature at the plastic tubes air entrance (12)
- 3 type J thermocouple to check the adiabatic condition at the back side of TRE-L box (7,8 and 9)
- 1 pyranometer placed in the south oriented face of TRE-L to measure incident solar radiation at each inclination

To measure outdoor weather conditions, a weather station formed by a cup-type anemometer, a wet bulb thermometer and a dried thermometer was used. It is placed next to the TRE-L and at 2 m height (see Fig.1). An extra weather station, formed by a cup-type anemometer, a horizontal pyranometer, a wet bulb thermometer and a dried thermometer placed at 10 m height was also installed for control or back-up purposes. Furthermore, in the measurement campaign of natural ventilation situations, a pyrheliometer was installed at the University Campus of Lleida to measure direct solar radiation.

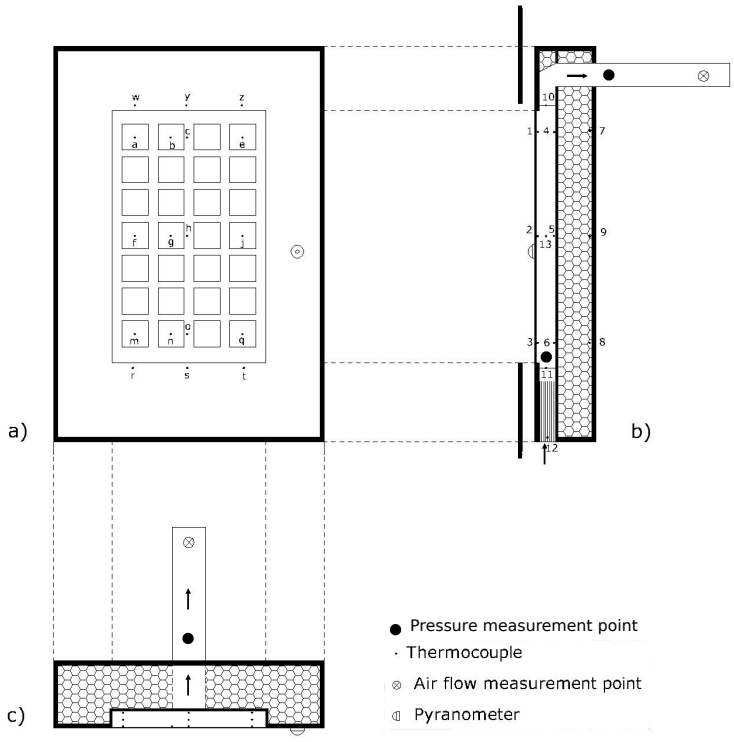

Figure 2: TRE-L measurement set-up: positioning of the sensors. (a) Front view; (b) cross view; (c) top view

In forced convection, the air flow produced by the variable speed fan is measured using a hot wire omni directional anemometer for small velocity regimes and a vane anemometer for high velocity regimes.

In natural convection, the air flow is measured through an indirect method based on measuring the readings of a differential pressure manometer with one pressure point measure placed at the entrance of TRE-L and the other pressure point placed at the PVC tube (see Fig. 1)

2.2.1. PV production monitoring

Special connections were manufactured within the PV modules: each string of PV cells was separately connected allowing four different short circuit current (I_{SC}) and open circuit voltage (V_{OC}) measurements within the same module. An electrical circuit, composed by relays and shunts, was manufactured for each one of the PV modules. The data logger collects voltage measurements and controls the circuits allowing these two different measurements to be made. To avoid excessive warming-up of the circuit shunts, each string remains 4 minutes in open voltage condition and only 1 minute in short circuit condition. The PV power production of the module is calculated as follows:

$$P_{PV} = FF_{PV}\, V_{OC}\, I_{SC} \tag{1}$$

The fill factor (FF) can be measured with a PVPM I-V curve tracer for instantaneous solar radiation levels or it can be evaluated following the expression obtained by Marion [20], which expresses its variation in function of the PV module temperature. The second option was selected for simplicity

2.2.2. Monitoring the temperatures of the reference modules

In the reference modules no thermocouples were installed at the rear side because non uniformity temperature distributions were expected. In these modules, the same special connections as the PV module of TRE-L were installed and the concept of equivalent cell temperature (ECT) was used to determine the PV module temperature. ECT was defined by the international standard IEC 60904-5 [21] as the uniform p-n junction temperature that would produce the measured electrical output of the PV device. The ECT can be calculated from V_{OC} measurements with equation 2.

$$ECT = T_{STC} + \beta^{-1} \cdot \left[V_{OC} - V_{OSTC} + D \cdot n_s \cdot ln\left(\frac{G_{STC}}{G}\right)\right] \tag{2}$$

The temperature coefficient of the open-circuit voltage of the PV module (β) defines the variation of the open circuit voltage with the temperature. Based on the measures performed by King and Kratochvil [22] for several PV modules with similar characteristics, the following value has been adopted: $\beta = -2.29\,^{\mathrm{mV}}/_{^{\circ}\mathrm{C}}$. The other coefficient,(D) corresponds to the diode thermal voltage. A value of $D = 29$ was obtained following the methodology defined in the international standard IEC 60904-5 [21]. The open circuit voltage at standard conditions $V_{O,STC}$, is provided by the manufacturer of the PV module.

2.2.3. Monitoring of the air flow rate in natural convection

To measure the air flow rate in natural convection, an indirect method has been used. A differential pressure transducer has been installed with two pressure points (see Fig.2, pressure points are the black dots). The pressure difference in these two points has been measured in such way that a negative pressure difference corresponds to an upwards flow in the ventilated air gap. The airflow rate is determined from the pressure difference, using the common power law relationship:

$$\dot{V} = a \cdot \Delta P^n \ \left[{}^{\mathrm{m}^3}/_{\mathrm{h}}\right] \tag{3}$$

Where $\dot{V}$ is the volumetric air flow rate , a is the cavity flow resistance coefficient and n is the flow coefficient. It should be remarked that Eq. 3 is not dimensionally homogeneous since a is not a dimensionless coefficient. The identification of the unknown coefficients of Eq. 3 has been determined experimentally by means of a variable speed fan. The air flow rate was measured with an omni directional anemometer following the procedure described by Mattson and Bloem [23]. At the same time, the pressure difference over the ventilated air gap was measured. From the data sets, coefficients a and n in Eq. 3 have been determined with the least squares technique defined by the Levenberg-Marquardt algorithm [24]. In Table 1, a summary of the obtained estimates of parameters and its confidence intervals (CI) is shown . As can be seen from the t value, the null hypothesis is not fulfilled and both parameters have enough significance.

	Estimate	Std. Error	t value	Pr (> t)	Asymptotic CI	
					2.5 %	97.5 %
a	49.979	0.569	87.83	$3.63 \cdot 10^{-9}$	48.517	51.442
n	0.535	0.012	42.46	$1.37 \cdot 10^{-7}$	0.502	0.567

Table 1: Parameters estimates of Equation 3

The coefficient of determination is $R^2 = 0.99$ and the residuals mean is around zero ($\mu_{resid} = -0.0029$). The Shapiro-Wilk test was carried out to confirm the normality of residuals (W=0.974, p-value=0,929).

2.3. Accuracy of measurements

All the type J thermocouples used in the experiments have been first calibrated at 0 °C and 100 °C. The resulting measurement accuracy was ± 0.5 °C. The thermocouples for measuring the air gap temperature were shielded from solar radiation with aluminum tape cylindrical shadings. The pyranometer was previously calibrated by the manufacturer and the declared sensitivity is 8.74 $\mu V/W/m^2$.

Regarding airflow rate measurements, two different methods were tested and compared. The first method was proposed by Mattson and Bloem [23]. Although the accuracy of the hot wire anemometer is in the range of ±3% of the reading, the overall accuracy of this method strongly depends on the selected section and on the position of the anemometer probe. A first attempt with a unidirectional probe was carried out and the measurements were not reliable, hence a omni directional probe was used instead. Another restriction concerns the measurement range of the hot wire anemometer, which is restricted to air velocities below 2.5 m/s within the duct which corresponds to very small Reynolds numbers within the air gap (Re < 3500). The second method is based on airflow measurements using a vane anemometer and a cup cone to drive the airflow. The accuracy of this vane anemometer is ±0.1 m/s. The difference between both methods was less than 3%, which assures a certain acceptability of the measurements.

The uncertainty in the measure of the airflow rate in natural convection is determined through error propagation of Eq. 3. The uncertainty of the differential manometer is ±1 % and the confidence intervals of the parameters are summarized in table 1. To calculate the error propagation considering parameters uncertainty, the Python software package developed by Lebigot E.O. [25] was used. The calculated uncertainty of the airflow measurement is $\pm 1.5\,\mathrm{m^3/h}$ which means between 10 % for low airflow rates and 6 % for higher air flow rates.

The accuracy of the PV power production measurements depends on the accuracy of the estimation of the FF. A PVMP I-V curve tracer was used to measure FF at several irradiance levels (from 500 to 800 $^W/_{m^2}$) . A correlation plot of the measured FF and the estimated ones, obtained through the expression of Marion [20] lead to a coefficient of determination of $R^2 = 0.9508$ Considering this high linear dependence this method of estimating FF can be considered acceptable and it was used to evaluate the PV electrical production.

The accuracy of the evaluation of the ECT, based on Eq. 2 , is obtained through a comparison with measurements from thermocouples placed at the rear side of the PV module at the TRE-L opening. A number of comparisons were carried out for several airflow regimes both in natural and in forced convection. The relative error (RE) has been determined as:

$$RE = \frac{ECT_{PV} - T_{PV}}{T_{PV}} \qquad [\%] \tag{4}$$

In table 2, a summary of the statistics of the RE, obtained for some representative days, is shown. Statistics for whole period of each experiment are shown in the first rows of the table, while the same statistics but for the hours when the solar irradiation is higher than 200 $^W/_{m^2}$ are shown at the bottom of the table. This lower limit is also defined in the IEC 60904-5 [21] as the validity range of Eq. 2

Date	29/07/2010	02/11/2010	04/08/2010	01/07/2013	04/07/2013
duration [h]	24	24	24	24	24
Reynolds	3000	12000	26000	free convection	free convection
mean [%]	1.31 ± 1.23	6.789 ± 1.36	6.25 ± 0.65	-1.99 ± 1.00	-0.87 ± 0.86
σ [%]	5.88	8.35	4.01	6.10	5.24
median [%]	0.11	6.97	6.36	-2.22	0.66
5_{th} percentile [%]	-5.26	-6.28	0.33	-10.37	-10.26
95_{th} percentile [%]	10.5	17.55	11.35	7.46	5.70
Incident solar Radiation $> 200\,\mathrm{W/m^2}$					
mean [%]	-1.99 ± 0.97	-0.15 ± 1.69	4.58 ± 1.24	-4.01 ± 0.97	-5.25 ± 1.17
σ [%]	3.54	6.52	4.78	4.16	3.79
median [%]	-3.60	-2.18	2.77	-4.46	-6.71
5_{th} percentile [%]	-5.37	-8.18	0.10	-9.75	-9.24
95_{th} percentile [%]	5.02	8.18	11.34	2.35	1.04

Table 2: Comparison of calculated ECT and thermocouple measurements for PV module of TRE-L. Basic descriptive statistics of relative error analysis for all the hours and for hours with solar irradiation $> 200\,\mathrm{W/m^2}$

As can be seen in Table 2, for the hours when $G > 200\,\mathrm{W/m^2}$, the average RE is always below 6 %. It can be also seen that 90 % of the RE are within the range of $\pm 11\,\%$ in all the cases. These statistics show that the accuracy of Eq. 2 is acceptable for analyzing and comparing PV temperatures.

2.4. Monitoring campaign

Two monitoring campaigns were performed at the installations of LOTCE in Lleida, Spain (local latitude of 41.6°N). The first one was oriented to analyze situations under forced regime and was extended over a one year period, lasting from August 2010 to September 2011. A sensitivity analysis was carried out by changing the PV module inclination, the ventilation regime and the rear facing material. Table 3 summarizes the forced ventilation regimes tested in the TRE-L for this first monitoring period. Three different PV module inclinations have been tested: 90°, 60° (optimized inclination for the winter period) and 30° (optimized inclination for the summer period) with respect to the horizontal plane. The experiments were carried out with the two different rear facing materials.

Volumetric air flow rate $[m^3/h]$	Cavity air velocity $[m/s]$	Reynolds number $[-]$
34	0.09	1200
51	0.13	1800
94	0.23	3000
195	0.50	7000
354	0.92	13000
560	1.46	20000
731	1.91	26000

Table 3: Ventilation regimes performed within the air cavity

In 2013 another monitoring campaign was carried out to measure the electrical and thermal performance of the same PV module under natural convection situation This monitoring campaign

was extended from 16th June 2013 to 10th March 2014. Two different inclinations were tested (optimized inclination and 60° deviation from optimal) and the black absorber was placed as the rear facing material. The two reference modules were also measured. The frequency of data gathering was the same than the forced convection monitoring period. For this monitoring period, the pyrheliometer installed at the University of Lleida (1 km from TRE-L) allowed for the measurement of all the components of solar radiation.

3. Experimental results

3.1. Effect of the rear facing material, air flow regime and inclination over the temperatures

3.1.1. Forced convection

A comprehensive analysis of the temperatures of the double skin PV system installed at the TRE-L has been carried out. A firs evaluation of the influence of the air flow regime in the temperature of the PV module is shown in Fig. 3. In this figure, the temperature difference between the PV module and the ambient air, $\triangle T_{PV-amb} = T_{PV} - T_{amb}$, is plotted against solar irradiation for several Re and for the situations with black absorber as the rear facing material. As can be seen, the behavior of the PV module does not follow a straight line in the graph; in particular, the temperature difference follows two different trends before and after solar noon because of the thermal inertia of the PV module. It can be also observed that the temperature of the PV decreases with the Re, but not linearly. Considering the same solar irradiation level, the temperature differences in laminar, Re=1.200, and in transition to turbulent flow, Re=7.000, reach similar levels while in turbulent regime, Re=26.000, the temperature differences are substantially smaller.

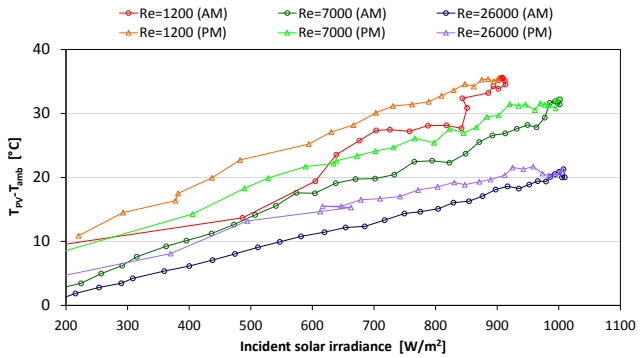

Figure 3: Temperature difference between the PV module and the ambient air versus irradiance for several Reynolds numbers. Optimized inclination and black absorber as the rear facing material

Table 4, shows the differences between $\triangle T_{PV-amb}$ of the laminar regime and of the turbulent one. Differences in $\triangle T_{PV-amb}$ have been calculated for several pairs of data with the same solar irradiation in hours before noon (AM) and after noon (PM). The mean is then calculated and shown in Table 4. As can be observed, the temperature differences between laminar and fully turbulent situations are in the range of 10-12 °C. The differences between laminar and transition are in the order of 5 °C and between transition and fully turbulent are in the range of 7 °C .

$Re_{laminar} - Re_{turbulent}$ [-]	1.200-7.000	7.000-26.000	1.200-26.000
$dif\ (\triangle T_{PV-amb,})$ (AM)-mean [°C]	4.5	6.3	10
$dif\ (\triangle T_{PV-amb,})$(PM)-mean [°C]	5.4	7.4	11.7

Table 4: Temperature difference between insulated reference PV module and PV module of TRE-L

In Fig. 3.1.1, the temperature difference between the PV module and the ambient air, $\triangle T_{PV-amb}$, versus solar radiation, is shown for the PV module of TRE-L and for the two reference PV modules. This comparison is plotted for the summer period, several *Re* numbers and with the black absorber as the rear facing material. It can be seen that for laminar situations, *Re*=3.000, the ventilated module of TRE-L is the coldest module before noon and it is in between the insulated and the free rack modules for the afternoon. In transient to turbulent airflow rates, *Re*= 7.000, the temperature of the ventilated PV module is the lowest in both morning and afternoon and in turbulent flows, *Re*= 20.000, this cooling effect is even increased.

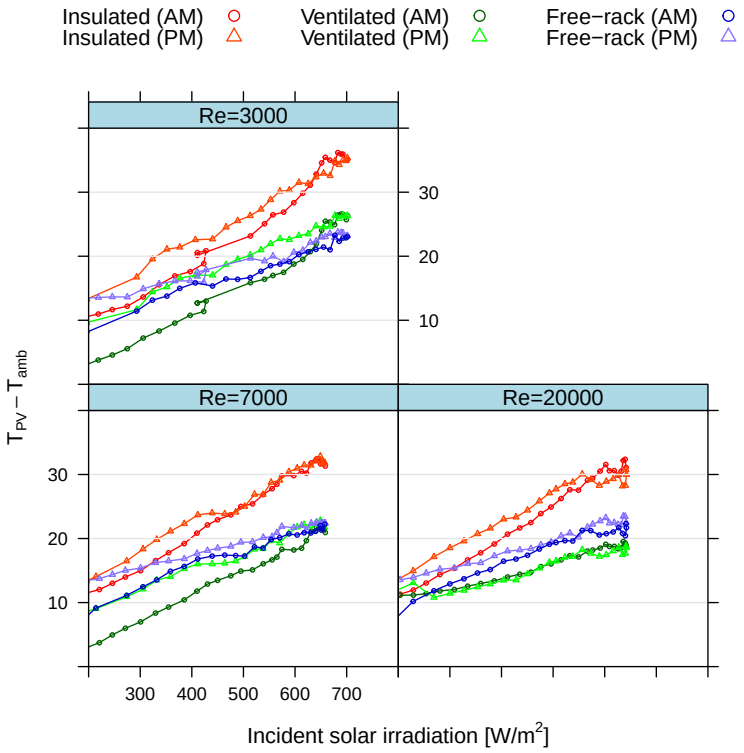

Figure 4: Comparison of average temperature differences between the PV and the ambient air versus solar irradiation for the PV module at TRE-L and the reference modules

Table 5, shows the differences between $\triangle T_{PV-amb}$ of the insulated reference module and of the ventilated PV module of TRE-L. Differences in $\triangle T_{PV-amb}$ have been calculated for 6 pairs of data with the same solar irradiation in hours before noon (AM) and after noon (PM). The mean is then calculated and shown in Table 5. As can be observed, the differences in $\triangle T_{PV-amb}$ are in between 7 and 10 °C. A temperature difference of this range may produce a decrease of the electrical efficiency of around 2-4%.

Re [-]	3.000	7.000	20.000
$dif\,(\triangle T_{PV-amb})_{insulated-TRE-L}$ (AM)-mean [°C]	10.6	8.4	8.2
$dif\,(\triangle T_{PV-amb})_{insulated-TRE-L}$ (PM)- mean [°C]	7.4	9.5	10.6

Table 5: Differences in$\triangle T_{PV-amb}$ between insulated reference PV module and PV module of TRE-L

To evaluate the effect of the rear facing material over the PV module temperature, a comparison between representative days with the same Re but with different rear facing material is carried out. In Fig. 5, the PV temperature versus solar irradiation is shown, for three different Re. Measures of one day with black absorber as rear facing material (red colors) are compared with PV temperature measures of one day with the white diffuser as rear facing material (blue colors). As previously mentioned, the hysteresis due to the thermal mass of the PV is clearly observed. In Fig. 5 in can be seen that the PV temperature is always higher for situations with the black absorber regardless the air flow regime.

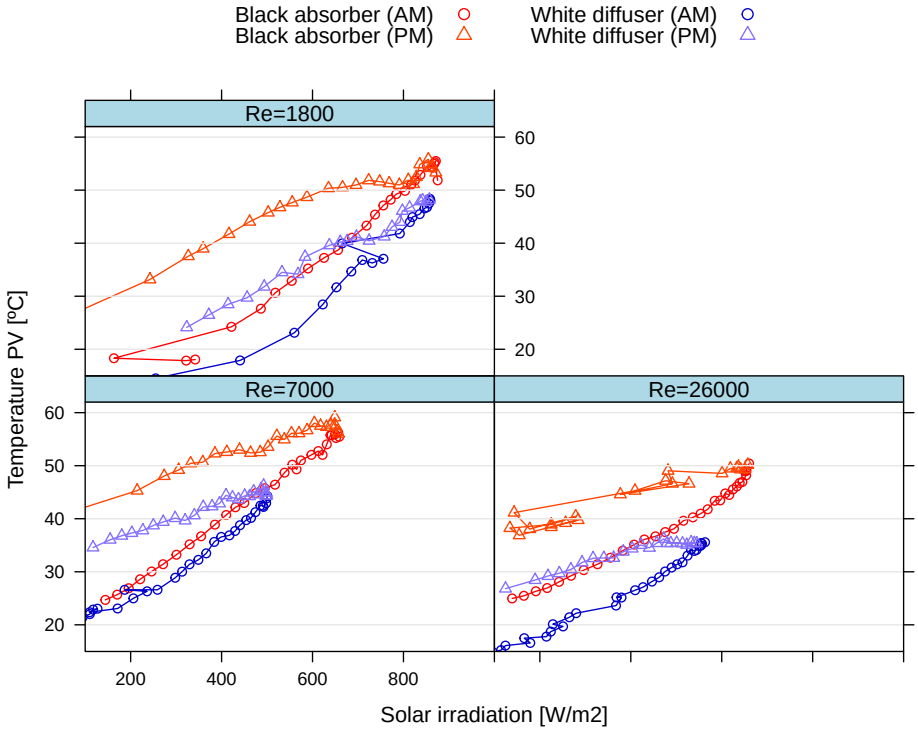

Figure 5: Effect of rear facing material in the temperature difference between the PV module and the ambient air versus solar radiation (Vertical inclination)

Table 6, shows the temperature difference between the cases with black absorber and those with white diffuser. The same average temperature differences as Table 5 have been calculated. As can be observed, the temperature difference between black absorber and white diffuser situations is around 10 °C in most of the cases. Smaller values are only found in the morning of the day with Re=7000. A temperature difference of this range may produce a decrease of the electrical efficiency of around 4%.

Re [-]	1800	7000	26000
$\overline{T}_{PV,black} - \overline{T}_{PV,white}$(AM) [°C]	9.6	4.3	10
$\overline{T}_{PV,black} - \overline{T}_{PV,white}$(PM) [°C]	10	9.5	11

Table 6: Temperature difference between rear facing materials

The temperature difference between the outlet and inlet of the air gap (ΔT_{air}), for several Re and different rear facing materials is shown in Fig. 3.1.1 and in Fig. 7. The influence of the air flow regime and of the deviation from the optimum inclination is shown in these figures. It is possible to observe that ΔT_{air} decreases when airflow rate increases and when the deviation from optimum inclination is higher. This ΔT_{air} is also higher when the black absorber is placed as the rear facing material regardless the deviation from the optimum inclination . In Fig. 3.1.1 it can be seen that the maximum registered value of ΔT_{air} is around 40°C for the situation of lowest airflow rate (Re = 1.200) and optimized inclination. In Fig. 3.1.1 b) and Fig. 7 d) it can be observed that the decrease of ΔT_{air} is not linear with the increase of the airflow rate. In addition, it is possible to observe that, especially when the PV module is 30° inclined or horizontal, ΔT_{air} reaches negative values during night (maximum values of -0.8 °C), meaning that the inlet air gets colder when passing through the PV module thus acting as a night cooling device.

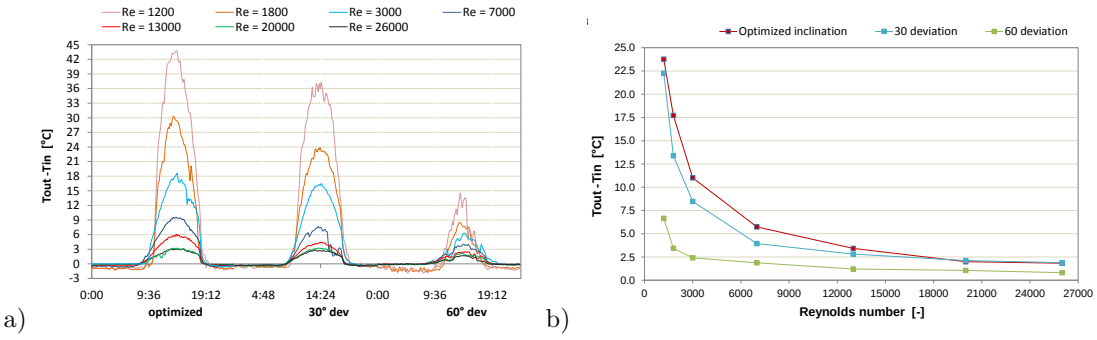

Figure 6: Temperature gain in the air gap for different ventilation velocities: effect of the deviation from the optimized inclination (black absorber as the rear facing material). a) Evolution in time; b) Averaged values

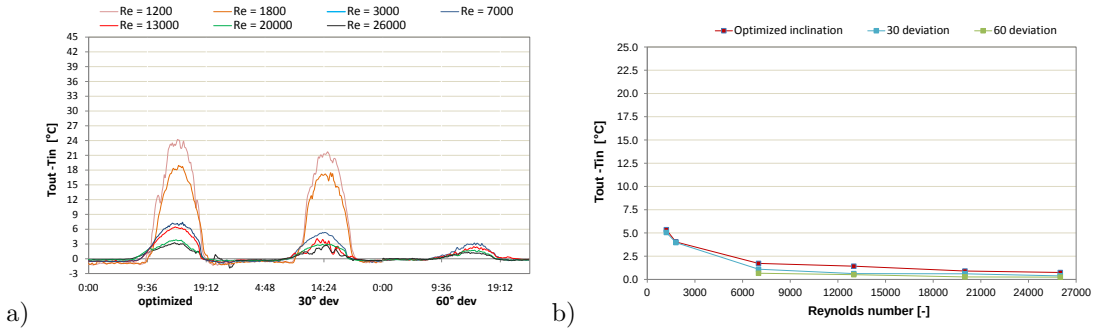

Figure 7: Temperature difference in the air gap for different ventilation velocities: effect of the deviation from the optimized inclination (white diffuse reflector as the rear facing material). a) Evolution in time; b) Averaged values

3.1.2. Natural convection

The monitoring period for natural convection comprised two periods: one summer month of 2013 (June-July) and one winter month of 2014 (March 2014). The TRE-L was positioned with two different tilt angles: vertical position in the summer, which is equivalent to 60° deviated from the optimal inclination; and a tilt angle of 60° in the winter, which is equivalent to optimal inclination. The black absorber was placed as the rear facing material.

In Fig. 8, a comparison between forced convection and natural convection situations is shown.

The temperature difference between the PV module and the ambient air is plotted against solar irradiation. As it can be seen, the temperature differences in the natural ventilation case are the highest, being even higher than the laminar situations in forced convection. That means the PV module is always warmer in natural convection than in all the ventilation regimes of forced convection.

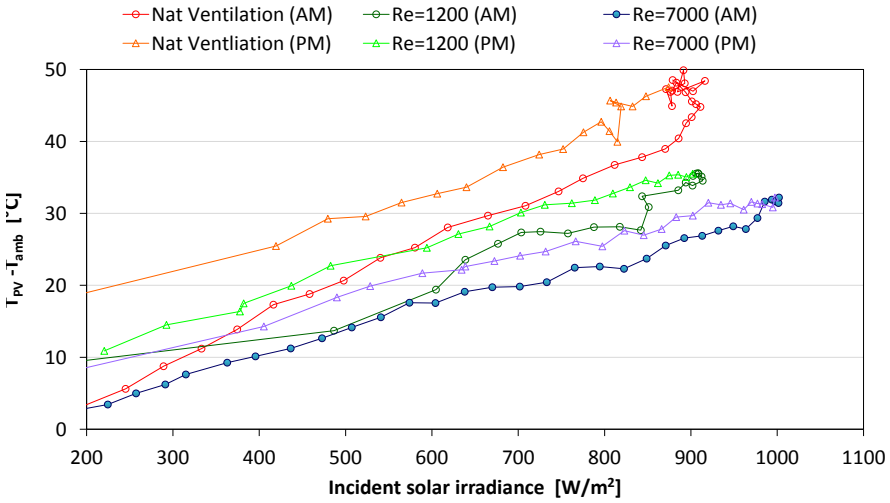

Figure 8: Comparison of natural convection and forced convection. Temperature difference between the PV module and the ambient air versus solar irradiation

Table 7, shows the differences between $\triangle T_{PV-amb}$ of case with natural ventilation and the cases with forced convection. Differences in $\triangle T_{PV-amb}$ have been calculated for several pairs of data with the same solar irradiation in hours before noon (AM) and after noon (PM). The mean is then calculated and shown in Table 7. As can be observed, the differences in $\triangle T_{PV-amb}$ are in between 7 and 12 °C. A temperature difference of this range may produce a decrease of the electrical efficiency of around 4-6% for the situations with natural convection.

Airflow regime [-]	Nat ventilation→Re=7.000
$dif\,(\triangle T_{PV-amb})$ (AM)-mean [°C]	7.4
$dif\,(\triangle T_{PV-amb})$ (PM)- mean [°C]	12.4

Table 7: Differences in$\triangle T_{PV-amb}$ between the case of natural convection and the case with transition to turbulent regime

In Fig. 3.1.2, a comparison of the difference temperature between the PV module of TRE-L (ventilated) and the reference modules (insulated and free-rack), for the cases with vertical inclination, is shown. As can be seen, the temperature ranges are very similar for the three modules and the differences are almost negligible. As was expected, the insulated PV module reaches highest temperatures for high irradiation and the ventilated PV module of TRE-L falls in between of both reference modules. This performance is very similar to the laminar situation of forced convection (see the case of Re=3.000 in Fig. 3.1.1).

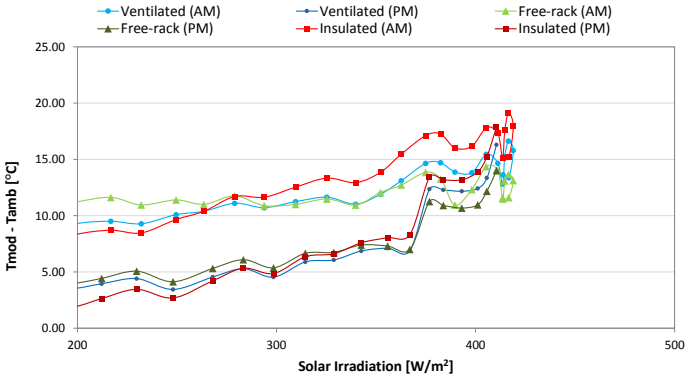

Figure 9: Natural convection. Comparison of average temperature differences between the PV and the ambient air versus solar irradiation for the PV module at TRE-L and the reference modules

The analysis of temperatures within the air gap, for natural convection, is shown in Fig. 3.1.2. The temperature of the inlet, outlet and middle sections of the air gap of TRE-L are shown for the situations with optimal inclination and for the situations with maximum deviation tilt angle (vertical inclination). As can be seen, the temperature difference between outlet and inlet decreases with the deviation from optimal tilt angle, as in the cases with forced convection. This decrease is in coherence with smaller irradiation levels because of reflection losses. In Fig. 3.1.2, it can also be observed that the gradient temperature between inlet and outlet of air gap is substantially higher than both the laminar regimes and the turbulent regimes of forced convection cases (see in Fig. 3.1.1 and Fig. 7).

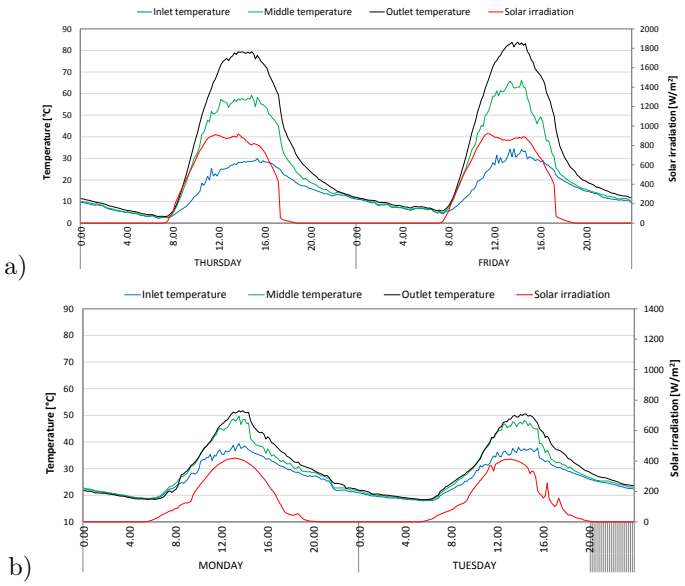

Figure 10: Air gap temperature differences in natural ventilation in two different tilt angles: a) situations with optimal inclination (5/03/2014-06/03/2014); b) situations with maximum deviation of tilt angle (01/07/2013-02/07/2013)

To analyze the effect of inclination in the air mass flow rate, the modified Rayleigh number

,$Ra_b^{'}$, will be determined for both monitoring periods and inclinations. Despite the non uniformity in wall temperatures of the PV and the rear facing materials , asymmetric Uniform Wall Temperatures (UWT) will be considered as boundary conditions to calculate the Rayleigh number. The temperature difference will be calculated based on the following equation [26]:$\triangle T = \frac{1}{2} \cdot [(T_{wh} - T_o) + (T_{wc} - T_o)]$. In Figure 11, the time evolution of air mass flow rate, $Ra_b^{'}$, temperatures of the PV module and temperature of the air at the inlet of the air gap of TRE-L, are shown for both inclinations.

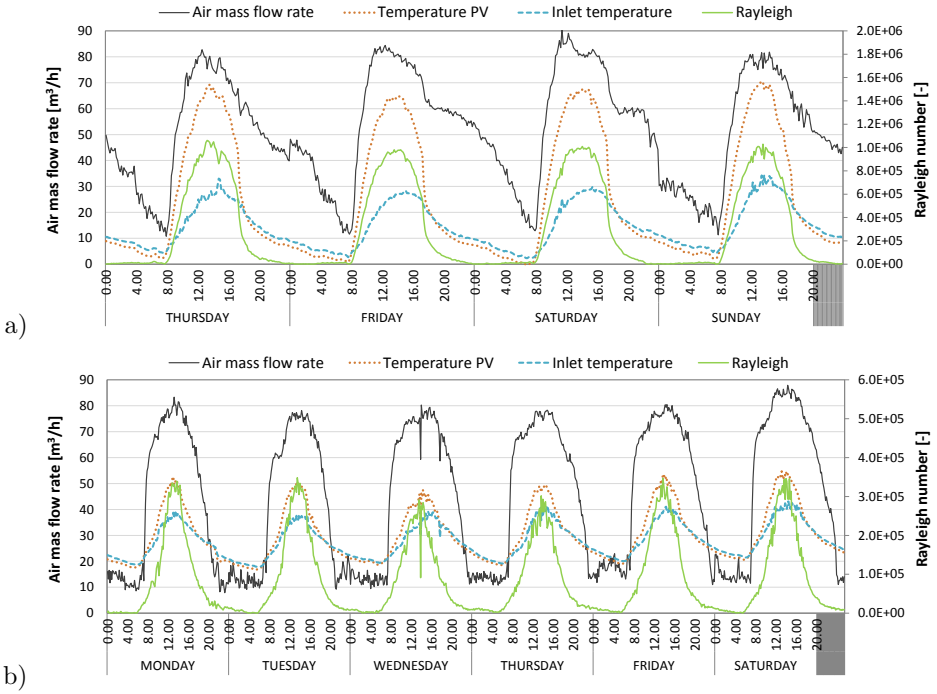

Figure 11: Rayleigh number and air mass flow rate in the air gap of TRE-L:a) Winter period (06-03-2014 to 10-03-2014) and optimal inclination; b)Summer period (24-06-2013 to 03-07-2013) and deviation from optimal of 60°

In Fig. 11 it can be seen that for the sunny hours, the case with optimal inclination receives more incident solar irradiation and hence, the $Ra_b^{'}$ number is substantially higher: maximum values of $Ra_b^{'} = 9.6 \cdot 10^5$ for the case with optimal inclination and maximum values of $Ra_b^{'} = 3.0 \cdot 10^5$ for the case of maximum deviation from optimal. This higher $Ra_b^{'}$ doesn't lead to higher volumetric air flow rates, since they reach similar maximum values. Instead, it causes a deformation in the volumetric air flow rate profile which can be appreciated in the evening hours of Fig. 11 a). This extra air flow rate can be understood as a downwards movement of air caused by the difference between the wall temperature of the PV module and the ambient temperature at the inlet (brown and blue dashed lines). It can be seen that this temperature difference is higher in the case of optimal inclination than in the case of maximum tilt deviation and this is the cause of the profile deformation of the case with optimal inclination and of the small airflow rate (around $10\,\mathrm{m^3/h}$) present in the case with maximum deviation during these hours. This effect could be considered as a night radiative cooling phenomenon.

In Fig. 11 it can also be seen that the $Ra_b^{'}$ ranges of the case with optimal inclination correspond to turbulent situations and the $Ra_b^{'}$ ranges of the case with vertical inclination correspond to the transition to turbulent region. This turbulence leads to high heat transfer processes between the

walls and the air gap, which means higher air gap temperature differences in natural convection than in forced convection, as shown in Fig. 3.1.2. The turbulence of natural convection cases is mainly related to increasing fluctuations in the temperature field rather than in the velocity field. As stated by [27], the main difference between turbulent natural convection and turbulent forced flows is that in natural convection the levels of averaged velocities are smaller, and the levels of disturbances are higher. Since in natural convection there is a high interdependence of the velocity and temperature fields, this higher velocity disturbance results in earlier effect of velocity fluctuations on the temperature field leading to higher heat transfer rates from the solid walls to the air gap, but smaller buoyancy induced air mass flow rates. This phenomenon is clearly appreciated in Fig 11 where it can be seen that the maximum air mass flow rate, achieved at noon, is around 80 m^3/h, resulting in small Reynolds number of Re =2.500, which is within the range of laminar regime of forced convection cases.

3.2. Effect of air flow rate and inclination over thermal and electrical production

In Fig. 12 thermal and electrical power of the PV module for some representative forced convection and natural convection days is presented.

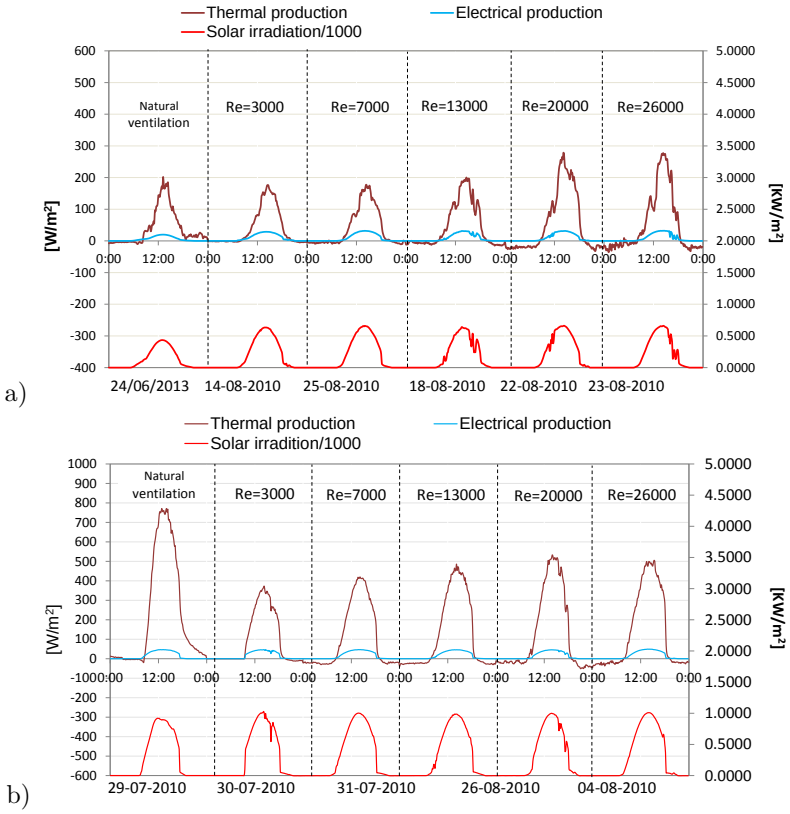

Figure 12: Thermal and electrical power per unit area in some representative days (black absorber sheet at the rear-facing surface). (a) vertical position or maximum deviation from optimal; (b) optimal inclination

Results for two different inclinations and several airflow regimes are presented. Days with the similar radiation levels, same inclination and wind speed lower than 5 m/s were selected to allow for cross comparison. It can be observed that the thermal power is the dominant power production in

both forced and natural ventilation situations. Highest electrical and thermal power are produced at optimized inclination in both airflow regimes. It can be seen that in forced convection, thermal and electrical power increase with higher air flow rates although the variation in electrical power is not so perceptible.

In Fig. 12it can be also seen that the thermal power production in natural convection is much greater than in forced convection, even exceeding forced fully turbulent situations in optimal inclination. This higher thermal production is mainly due to greater temperature differences between outlet and inlet in natural convection than in forced convection for similar air flow rates (as was stated in Fig. 3.1.2). The reason of these higher temperatures is related to the specific features of the transition to turbulent in natural convection situations, as mentioned in the previous section and clearly described in [27]. In the natural convection situations measured at the TRE-L, the transition to turbulence occurs in both thermal and dynamic boundary layers almost simultaneously, since the Prandtl number is $Pr \sim 1$. Initial velocity fluctuations rapidly cause disturbances in the temperature field and thus, high increases in the turbulent thermal diffusivity which finally leads to high heat transfer at the walls and rapid warming up of the air in the channel. This effect is confirmed by the higher values of temperature at the outlet but relatively small air flow rates (equivalent to maximum Reynold numbers of Re=2.700 in optimized inclination and Re=2.300 in maximum deviation from optimal). On the contrary, in forced convection situations, the turbulence is reached because of high turbulent viscosity due to higher Reynolds numbers. Since the thermal power depends on the air mass flow rate and the temperature gradient, high thermal power values are obtained in both air flow regimes but greater values are found in natural convection cases.

To quantify the effect of inclination and air flow rate over the thermal and electric production thermal and electrical efficiency coefficients are defined as the ratio between outgoing and incoming energy . They are calculated in a daily base and expressed by:

$$\eta_{th} = \frac{\sum Q_{th}}{\sum (G\, A_{PV} \cdot t)} = \frac{\sum \rho \cdot \dot{V} \cdot c_p \,(T_{out} - T_{in})}{\sum G\, A_{PV}}$$

$$\eta_{el} = \frac{\sum E_{el}}{\sum (G\, A_{PV} \cdot t)} = \frac{\sum P_{el}}{\sum G\, A_{PV}}$$

Where $\sum Q_{th}$ is the thermal energy produced a day within the air gap, $\sum E_{el}$ is the electrical energy produced a day by the solar PV module, and $\sum (G\, A_{PV} \cdot t)$ is the incident solar energy received by the TRE-L in a day. The negative terms of $\sum Q_{th}$ are not considered in the evaluation of this produced energy. In the cases with natural convection, the thermal power produced in night time is neither included.

In Fig. 13 and Fig. 14 daily thermal efficiencies for different air flow rates in forced convection are presented for the optimized inclination cases and the two rear facing materials. It can be seen that the thermal efficiency increases with the air flow rate. As was previously stated, this increase in thermal production is mainly caused by the increase in the air mass flow rate which balances the decrease of the temperature between outlet and inlet of the air gap, ΔT_{air}, (see Fig 3.1.1). The dependence of the thermal efficiency with the deviation from the optimized inclination is also shown in these figures. It can be observed that the thermal efficiency decreases when the deviation increases because of the angle dependence of the reflection losses of the PV module. Only in the case of very small Reynolds number and white reflector, the thermal efficiency remains almost constant regardless the inclination.

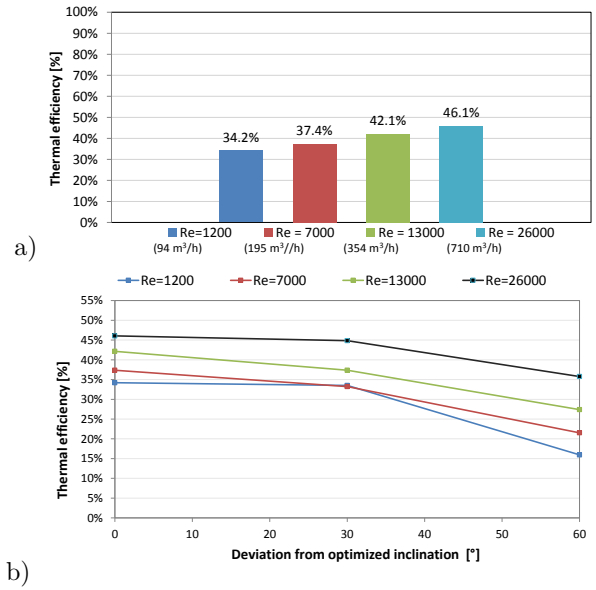

Figure 13: Forced convection. Daily thermal efficiencies with the black absorber sheet. (a) Effect of the airflow rate within the channel for the optimized inclination; (b) Dependence of the daily thermal efficiency with the deviation from the optimized inclination

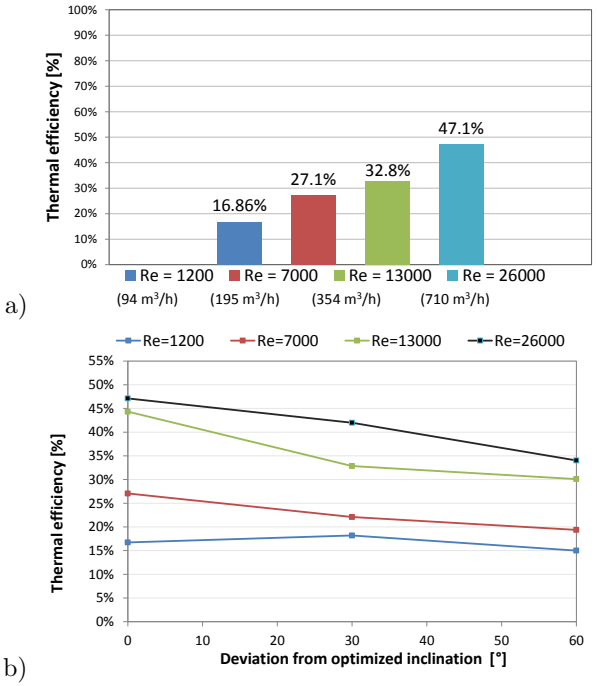

Figure 14: Daily thermal efficiencies with the white diffuse reflector. (a) Effect of the airflow rate within the channel for the optimized inclination; (b) Dependence of the daily thermal efficiency with the deviation from the optimized inclination

In Fig. 13 and Fig. 14 it can be also observed that effect of the rear material is only perceptible for laminar situations, Re $\leq$ 7.000, and deviation from optimized inclination smaller or equal to 30°. In these situations, it can be concluded that the black absorber sheet improves the thermal energy production of the system compared to the white diffuse reflector.

In Fig.15, the effect of air flow rate and inclination over electrical efficiency coefficient for the cases of forced ventilation is shown. As can be seen, the electrical efficiency remains almost invariable regardless the air flow regime and the deviation in respect to optimal inclination.

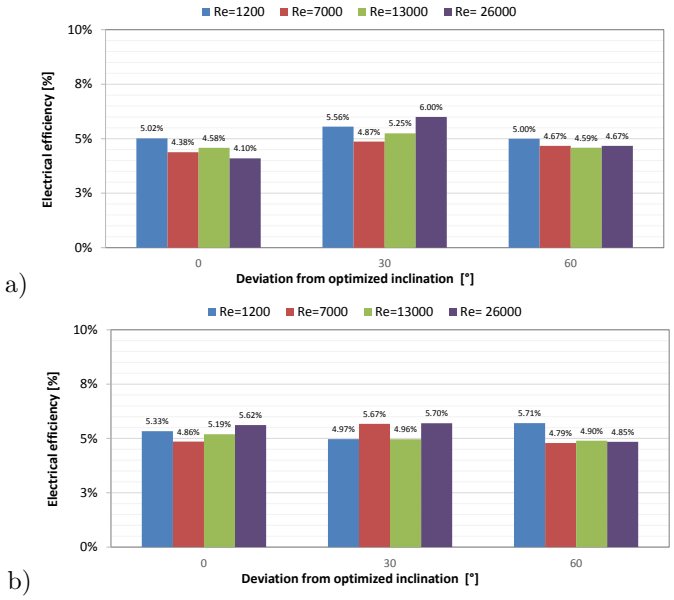

Figure 15: Effect of the air mass flow rate and inclination in the daily electric efficiencies (a) White diffuser; (b) Black absorber

In Table.8, the variation of thermal and electrical efficiency with deviation from the optimal inclination, for the situations with natural convection, is shown. As can be seen, the thermal efficiency highly decreases when the deviation increases, as in the case of forced convection situations. The electrical efficiency also decreases but to lesser extent. If thermal efficiency values of Table 8 are compared with the thermal efficiency values of Fig. 13 with the same deviation from optimized inclination, it can be observed that the situations with natural convection are substantially more energy efficient than the forced convection situations, reaching values over 80 % of energy efficiency. As was previously stated, this high thermal efficiency is due to higher turbulent thermal diffusivity of the situations with natural convection.

Deviation from optimal [°]	Thermal efficiency [%]	Electrical efficiency [%]
0	86.44	5.17
60	34.69	4.30
Variation [%]	-60	-16.76

Table 8: Variation of thermal and electrical efficiency with the deviation from the optimal inclination

4. Conclusions and further developments

An improved version of the Test Reference Environment for the analysis of building integrated PV modules has been constructed and monitored during two periods in two years. This new outdoor controlled environment, called TRE-L, allows for the parametric analysis of PV ventilated components under several air flow regimes, inclinations, and real weather conditions.

In this research, two air flow situations (natural and forced), in laminar and turbulent regime, have been combined with three different inclinations and two rear facing materials to create a set of experimental trials which allow for the evaluation of each parameter effect over the electric and thermal production and over the temperature distributions in the PV module and the air gap .

Some conclusions can be obtained regarding the experimental set up in outdoor conditions:

- Cylindrical shading protections are found to be very effective to measure air gap temperatures and to avoid harmful effects of direct solar radiation.

- The measurement of air mass flow rate constitutes the biggest challenge and is the main cause of uncertainty. In forced convection, it is convenient to use the methodology defined by Mattson and Bloem [23] for low *Re*, and a vane anemometer for bigger *Re*. In natural convection, an indirect method based on the power law relationship between the differential pressure at the inlet and outlet and the volumetric air flow rate has proved to be valid. However, due to the small height of TRE-L, which leads to low buoyancy effect, some uncertainties in finding the instant when pressure difference is null are found.

- Regarding the measurement of the PV temperatures, it was found that the use of the ECT is limited to solar irradiation levels higher than $200\,{}^{W}/_{m^2}$. This limitation and some dispersion of the calculated ECT suggest that it is preferable to install thermocouples at the rear side of the PV module and take direct measurements of temperature.

Regarding the parametric analysis, a general conclusion can be obtained: from an energy efficient perspective, natural convection is a preferable option for producing both thermal energy and electricity in ventilated PV components. Although the air mas flow rate is smaller than in turbulent forced convection situations, the higher turbulence in the temperature field causes higher sensible temperature gain within the air gap and, therefore, higher production of thermal energy. These results are in coherence with the conclusions obtained by [27] in relation to the special characteristics of transition to turbulence in natural convection situations.

Regarding the effect of the rear facing material, in situations with forced air flow, it can be concluded that the effect of the rear facing material is only perceptible for laminar situations, Re $\leq$ 7000, combined with deviations from optimized inclination $\leq$30°. In these situations, it can be concluded that the black absorber sheet improves the thermal energy production of the system, while decreases the electric production.

Regarding the effect of the air flow regime in forced convection, it is also stated that the both the thermal and electric production increase with the *Re,* although the variation in the electric power is not so appreciable .In the case of the thermal production, the decrease of the temperature difference between outlet and inlet of the air gap, is compensated by an increase of the air mass flow rate.

The effect of the inclination is the same for both natural and forced convection: the thermal and electric power, increase with inclinations close to the optimized inclination of each season. The inclination doesn't affect the air mass flow rate in natural convection, and the maximum values are the same regardless the variation of inclination.

More specific conclusions can be obtained in relation to the distribution of PV temperatures:

- In forced convection, the PV temperature decreases when airflow rate increases but not linearly, this decrease is greater in turbulent regimen than in laminar one. The temperature differences between laminar and fully turbulent situations are in the range of 10-12 °C. The differences between laminar and transition are in the order of 5 °C and between transition and fully turbulent are in the range of 7 °C .
- In natural convection, the PV temperature is always warmer than in forced convection regardless the *Re*.

The comparison of temperatures between the ventilated PV module in vertical position and the reference modules, yields to the following conclusions:

- In forced situations, the insulated module is always warmer than the ventilated PV. In laminar flows, the ventilated PV is in between the free rack and the insulated module. However, when the *Re* approaches transition to turbulent regime, the ventilated PV decreases its temperature until reaching the temperature of the free-rack mounted. In fully turbulent regime, the PV ventilated module is the coolest module, achieving temperature differences between with the insulated PV moduleof around 15 °C.
- In natural convection, the temperature differences are not very appreciable, and the ventilated PV is always in between the insulated and the free rack PV modules.

The results of the comparison of the ventilated PV with the reference modules, reflect the necessity of redefining the BIPV systems performance indicators under real operating conditions, which clearly differ from both STC and NOCT standards. These results are in coherence with the proposal for an improved and standardized test reference environment for obtaining more precise performance indicators of BIPV components in outdoor conditions, as suggested by J.J. Bloem [16].

Some conclusions can be found regarding the performance of the ventilated PV module in the night, for both natural and forced convection situation. It can be observed that the temperature of the PV rapidly decreases and even achieves lower values than the ambient temperature. This negative temperature difference produces a cooling effect over the air which enters the cavity in forced convection plus a downwards flow in natural convection. This behavior can be understood as a radiative cooling effect and could be used for passive cooling in the summer period.

The experimental work carried out in this research can also serve for the validation of complex dynamic models able to describe the system behavior in different conditions including natural convection situations. From experimental results it has been found that the effect of the PV module thermal inertia has to be taken into account in these dynamic models for a correct characterization of the BIPV system.

Further research will be oriented to perform extended monitoring campaigns with different rear facing materials, different PV modules with glass to glass or opaque configurations and to start the evaluation of dynamic models able to characterize the energy performance of BIPV components.

Nomenclature

A	area (m^2)
a	cavity flow resistance coefficient (-)
b	depth of the air gap of TRE-L (m)
H	height of the air gap of TRE-L (m)
c_p	specific heat coefficient at constant pressure (J/kgK)
D	diode thermal voltage (-)
E	electricity production (W)

FF	fill factor (-)
G	solar irradiance (W/m^2)
I_{SC}	short circuit current (A)
k	thermal conductivity (W/mK)
$\dot{m}$	air mass flow rate (kg/s)
n	flow coefficient (-)
n_s	number of solar cells (W)
P	PV power production (W)
$\dot{Q}$	output thermal power (W)
Ra'_b	modified Rayleigh number for uniform wall temperature (-),$Ra'_b = (\rho^2 g \beta c_p \Delta T b^4)/\mu k H$
T	temperature ($^\circ C$)
t	time step (h)
V_{OC}	open circuit voltage (V)
$\dot{V}$	Volumetric air flow rate (m^3/s)

Greek symbols

β	temperature coefficient of the open circuit voltage (mV/ºC)
ΔT	temperature difference [K]
η	efficiency (-)
ρ	density [kg/m^3]
μ	dynamic viscosity [Pas]

Subscripts

a	ambient air
air	air gap
$black$	black absorber
$dest$	destroyed
el	electrical
in	inlet
out	outlet
oc	open circuit
PV	photovoltaic module
SC	short circuit
STC	standard conditions
th	thermal
$white$	white reflector

References

[1] European Parliament. *Directive 2010/31/EU of the European Parliament and of the Council of 19 May 2010 on the energy performance of buildings.* 2010.

[2] Jordi Cipriano, Guillaume Houzeaux, Daniel Chemisana, Chiara Lodi, and Jaime Martí-Herrero. Numerical analysis of the most appropriate heat transfer correlations for free ventilated double skin photovoltaic façades. *Applied Thermal Engineering*, 57(Issues 1-2):57–68, August 2013.

[3] IEC-61215. *Crystalline Silicon Terrestrial Photovoltaic (PV) modules - Design Qualification and Type Approval.* 2005.

[4] T.Y.Y. Fung and H. Yang. Study on thermal performance of semi-transparent building-integrated photovoltaic glazings. *Energy and Buildings*, 40:341–350, 2008.

[5] M. Sandberg and B Moshfegh. Buoyancy-induced air flow in photovoltaic facades effect of geometry of the air gap and location of solar cell modules. *Building and Environment*, 37:211–218, 2002.

[6] E.J. Bakker. *Ecobuild research: full-scale testing of innovative technologies for energy efficient houses*. The Netherlands: Report ECN RX-04-005, 2004.

[7] Y. Chen, A.K. Athienitis, and K. Galal. Modeling, design and thermal performance of a BIPV/T system thermally coupled with a ventilated concrete slab in a low energy solar house: Part 1, BIPV/T system and house energy concept. *Solar Energy*, 84:1892–1907, 2010.

[8] S.O. Jensen. Results from measurements on the PV-VENT systems at lundebjerg. Technical Report Report SEC-R-14, Danish Technological Institute, Energy Division, 2001.

[9] A. Lloret, O. Aceves, L. Sabata, J. Andreu, J. Merten, M. Chantant, and U. Eicker. Lessons learned in the electrical system design, installation and operation of the mataro public library. In *Proceeding of 14th European Photovoltaic Solar Energy Conference*, Barcelona, 1997.

[10] J.R. Bates, U. Blieske, J.J. Bloem, J. Campbell, F. Ferrazza, R.J. Hacker, P.A. Strachan, and Y. Tripanagnostopoulos. Building implementation of photovoltaics with active control of temperature. In *Proceedings of the 17th European Photovoltaic Solar Energy Conference*, Munich, 2001.

[11] J.J. Bloem. Evaluation of a PV-integrated building application in a well-controlled outdoor test environment. *Building and Environment*, 43:205–216, 2008.

[12] J. Marti-Herrero and M.R. Heras-Celemin. Dynamic thermal simulation of a solar chimney with PV modules. pages 891–896, 2005. cited By (since 1996)4.

[13] L.M. Candanedo, A. Athienitis, and K.W. Park. Convective heat transfer coefficients in a building-integrated Photovoltaic/Thermal system. *Journal of Solar Energy Engineering ASME*, 133:021002–1–021002–14, 2011.

[14] K. E. Park, G. H. Kang, H. I. Kim, G. J. Yu, and J. T. Kim. Analysis of thermal and electrical performance of semi-transparent photovoltaic (PV) module. *Energy*, 35(6):2681–2687, June 2010.

[15] L. Olivieri, E. Caamaño-Martin, F .Olivieri, and J. Neila. Integral energy performance characterization of semi-transparent photovoltaic elements for building integration under real operation conditions. *Energy and Buildings*, 68, Part A:280–291, 2014.

[16] J.J. Bloem, C. Lodi, J. Cipriano, and D. Chemisana. An outdoor test reference environment for double skin applications of building integrated PhotoVoltaic systems. *Energy and Buildings*, 50:63–73, 2012.

[17] C. Lodi, J. Cipriano, J.J. Bloem, and D. Chemisana. Design and monitoring of an improved test reference environment for the evaluation of BIPV systems. In *Proceedings of the 25th European Photovoltaic Solar Energy Conference*, page 5135–5140, Valencia, 2010.

[18] C. Lodi, J. Cipriano, P. Bacher, and H. Madsen. Modelling the heat dynamics of a monitored test reference environment for BIPV systems through deterministic and stochastic approaches. Technical University of Denmark, Lyngby, Denmark, May 2011.

[19] C. Lodi, P. Bacher, J. Cipriano, and H. Madsen. Modelling the heat dynamics of a monitored test reference environment for building integrated photovoltaic systems using stochastic differential equations. *Energy and Buildings*, 50:273–281, July 2012.

[20] B. Marion. A method for modeling the current–voltage curve of a PV module for outdoor conditions. *Progress in Photovoltaics: Research and Applications*, 10(3):205–214, 2002.

[21] International Electrotechnical Commission (IEC). IEC-60904-5.Photovoltaic devices – part 5: Determination of the equivalent cell temperature (ECT) of photovoltaic (PV) devices by the open-circuit voltage method, February 2011.

[22] D.L. King, J.A. Kratochvil, and W.E. Boyson. Temperature coefficients for PV modules and arrays: measurement methods, difficulties, and results. In *Photovoltaic Specialists Conference, 1997., Conference Record of the Twenty-Sixth IEEE*, page 1183–1186, 1997.

[23] M. Mattson and J.J Bloem. *Measuring air flow in a ventilation duct by traversing an anemometer*. Internal report, JRC Ispra, 1998.

[24] J. J. Moré. The levenberg-marquardt algorithm: implementation and theory. *Lecture Notes in Mathematics: Numerical Analysis, G.A. Watson (Ed.),Springer-Verlag: Berlin*, (630):105–116, 1978.

[25] Eric O. Lebigot. Uncertainties: a python package for calculations with uncertainties. http://pythonhosted.org/uncertainties/. revised BSD license.

[26] W Aung, L. S Fletcher, and V Sernas. Developing laminar free convection between vertical flat plates with asymmetric heating. *International Journal of Heat and Mass Transfer*, 15(11):2293–2308, November 1972.

[27] Martinenko Oleg G. and Khramtsov Pavel P. *Free-Convective Heat Transfer*. Springer-Verlag Berlin Heidelberg, Netherlands, 2005.

Evaluation of a multi-stage guided search approach for the calibration of building energy simulation models

J. Cipriano[a]*, G. Mor [a], D. Chemisana[b], D. Pérez[c], G. Gamboa[c], X. Cipriano[c]

[a] *Centre Internacional de Mètodes Numèrics a l'Enginyeria (CIMNE), Building Energy and Environment Group,CIMNE-UdL classroom c/Pere de Cabrera s/n , 25001, Lleida, Spain*

[b] *Applied Physics Section of the Environmental Science Department, University of Lleida, c/Jaume II 69, 25001 Lleida, Spain*

[c] *Centre Internacional de Mètodes Numèrics a l'Enginyeria (CIMNE), Building Energy and Environment Group, c/Rambla St Nebridi 22 , 08222 Terrassa, Spain*

* *Corresponding author: Centre Internacional de Mètodes Numèrics a l'Enginyeria (CIMNE), Building Energy and Environment Group. CIMNE-UdL Classroom. c/Pere de Cabrera s/n. CREA building. Office 1.15, 25001. Lleida, Spain. e-mail: cipriano@cimne.upc.edu, phone: +34 973003574, fax: +34 973003575*

Abstract

This paper is focused on increasing the knowledge on methods for calibrating BES models and to get more insights of different approaches for the optimization of the calibration process. The paper will be centered in the evaluation of a multistage guided search approach. It defines an iterative optimization procedure which starts with the assignment of probabilistic density functions to the unknown parameters, followed by a random sampling and running batch of simulations. It then finishes with an iterative uncertainty and sensitivity analysis combined with a re-assignment of the ranges of variation of the strong parameters. The procedure converges when no new influencing parameters are found. This method is applied to a real case study consisting of an unoccupied office building located in Lleida (Spain). The measured indoor temperature has been used to determine the uncertainty and precision of the method. The effect of the size of the sampling, of the number of iterations and of the parameters of the global sensitivity method are analyzed in detail. The results of this paper exemplify the degree of accuracy of multistage guided search approaches, and illustrate the reasons how these analyses can contribute to the improvement of more refined calibration methods.

Keywords: Latin Hypercube Monte Carlo method (LHMC), Chi-square method, Sensitivity Analysis, Building Energy Simulation (BES) models, Calibration of simulations

1. Introduction

The calibration of forward Building Energy Simulation (BES) models plays a fundamental role in building energy performance analysis and is a critical factor for proper evaluation of energy savings produced by energy conservation measures . In order for BES models to be used with any degree of confidence, it is necessary that the existing model closely represents the actual behaviour of the building under study. Therefore, the purpose of model calibration is to reduce the discrepancies between building energy simulation (BES) and measured building energy performance. The need for calibration of building models is not an indication of the limited capacity of prediction of buildings models; it is ,instead, a manifestation of the limited knowledge that the model developer has on the operational parameters of the building, as well as on the stochastic nature of the

building-users behavior and on the lack of control of the pathologies generated in construction or operation of the buildings. Calibration can be understood as the process of "fine-tuning" the values of the unknown parameters of a model in order to minimize the differences between the predicted outputs and the observed data. Due to the large number of unknown input parameters in a detailed BES model, calibration is a complex procedure characterized by a non-unique solution [1] and high uncertainties. In many engineering fields, a model is usually calibrated by implementing a maximization/minimization of one of the statistical indicators of goodness of fit, through a computer code, and by exploring the input space until convergence is reached. However, this can be cumbersome and complicated, especially in the case of complex and/or over parameterized models [2] such as BES. Unfortunately, there is substantial work associated with the detection of influencing parameters in over parameterized models and this cannot be done in a straightforward manner. As highlighted by Reddy T. and Maor I., [3], it is almost impossible to identify the exact solution to the calibration problem of BES models. Under this particular circumstance, there is a need to look for alternative strategies which can be more appropriate for these models and that can give the users additional information to better understand the insights of BES models.

A review of current literature on this topic has revealed that there is no generally accepted method for calibration of BES following other approaches. Some authors [4], [5] addressed calibration methodologies based on manual refinement of the BES models. These methodologies followed clearly defined standards [6, 7] for laying down the maximum tolerances of residuals and for measuring and verification of energy savings, however, the refinement of the BES models was addressed based on the experience of the analyst and no systematic approach was taken into account.

Recently, the calibration of BES models has been included in a more formal framework due largely in part to the advances in the fields usually known as UA (Uncertainty Analysis) and SA (Sensitivity Analysis) that are seen more and more as prerequisites for any field that makes extensive use of model predictions. Sensitivity analysis applied to BES models calibration can help in understanding the relative influence of input parameters in the output [8]. The combination of random sampling trials and sensitivity analysis of the parameters seemed to be a good approach to perform BES calibration. Several sensitivity analyses can be used, Tian W. [9] divided the methods for sensitivity analysis into local and global approaches, considering the global approach as the more reliable one for BES calibration. In 2006, Reddy and Maor [3] defined a detailed procedure to afford calibration of BES models based on the Latin Hypercube Montecarlo (LHMC) method and global sensitivity analysis. The proposed methodology involved four main steps: i) identification of a set of influential input parameters along with their better estimates and their range of variation; ii) a coarse grid search using LHMC simulation to identify a sub-set of the most sensitivity parameters; iii) a fine grid calibration to further refine the feasible solutions and iv) predictions of energy savings using a small number of the top feasible solutions. This methodology was applied over three case study office buildings using monthly energy consumption data as the basis for calibration. Many doubts related to this methodology remained unclear and [3] also highlighted the need for further research in issues such as minimum sampling size evaluations, selection of one-stage or multi-stage procedures and also if the fine grid calibration was necessary or not. Corrado and Mechri [10] applied uncertainty and global sensitivity approaches to analyze the energy performance of a family house in Turin, Italy. A widespread list of 129 input data was identified and probability density functions (PDF) were assigned to each parameter. A comprehensive review of available PDF was provided and the causes of data variability were also discussed. The LHMC method was applied to generate random samplings and the Morris technique was applied to perform a sensitive analysis and to obtain the dominant parameters. This research concluded that a very small group of unknown parameters were the ones which were affecting the energy consumption of the building. In this previous research study, as well as in others [11] , LHMC sampling has been used because of its efficient stratification properties which allow the extraction of a large amount of sensitivity information with a relatively

small sample size [12]. In [13] it has been proved that, for the same number of simulations, the LHMC method produces a more robust result compared to the stratified method, which in turn produces a more robust result compared to the simple method. It was also concluded that the Monte Carlo uncertainty analysis in typical building simulations should use about 100 runs and simple random sampling. In 2011, Coakley et al [14] suggested a novel methodology to calibrate BES based on LHMC sampling combined with a regional sensitivity analysis using Monte Carlo Filtering approach, as described by A. Saltelli [15]. The overall methodology is outlined and the first stages of the proposed calibration methodology are applied to a $700\,m^2$ naturally-ventilated library building using short-term monitored BMS and sensor data. The paper concludes with a discussion of how this methodology differs from existing approaches and the benefits it offers over traditional calibration technique. It also highlights the need of iterative regional sensitivity analysis for those situations in which goodness of fit falls out of accepted ranges. More recently [16], a very detailed review of existing sampling techniques and sensitivity analysis was carried out in for uncertainty analyses of BES with a large number of unknown parameters ($\approx$ 1,000). The balance between computation time and accuracy of the LHMC method and of the quasi-random sampling method was analyzed, leading to the conclusion that the second one has faster convergence. This is a crucial issue in calibrations with such large number of parameters. In addition to this, an input-output sensitivity analysis, followed by a decomposition to quantify which intermediate processes were contributing the most to this uncertainty, were performed. This type of analysis, including the decomposition, is valuable for identifying which subcomponents of a model need more attention during building design or model calibrations. The same author, [17] used the results of the previous analyses to perform a methodology for meta-model optimization in BEMS . A full meta model was created and an energy performance optimization has been carried out. The creation of full order or reduced order meta-models can be understood as one step forward to the guided coarse grid search outlined by [3] since it not only leads to an improvement of the calibration, but also allows for the implementation of many different cost functions or optimization algorithms without repeating time-intensive energy simulations. The above mentioned studies highlighted that meta-models are powerful and promising approaches to allow for permanent commissioning of buildings, fault detection and control optimization, however, some of these previous studies fails in a lack of detailed analysis of the effect of the range of variation of the input parameters and of performing the coarse grid search limited to a single stage random sampling, which clearly conditions the subsequent meta model, as stated by [3]. In the previous studies, the range of variation of parameters are often arbitrarily chosen, which may of course, influence the output uncertainty as well.

In this research, a contribution to achieve more insights of the coarse grid search stage analysis is proposed for buildings in non occupied periods. This procedure has many similarities with the methodology defined by [3], however some changes are implemented. First of all, the new procedure will be used to calibrate BES models of real buildings under free floating conditions and not under real energy consumption situations. Considering that in these situations the number of unknown parameters is substantially smaller, and assuming that the uncertainty of data coming from monitored indoor temperature is also smaller than the data coming from monthly energy consumption measurements, both the goodness of fit criteria and the parameters for the sensitivity analysis are re-defined to become more demanding than those defined in [3]. The suggested Goodness of Fit (GOF) criteria is twice as stringent as the value proposed by [3]. A multi stage procedure based on LHMC method is also used in this paper, however, in stead of fixing the strong parameters to discrete values, as proposed by [3], a re-assignment of their estimates and range of variation is carried out after each iteration. In order to reduce the uncertainty of the method, a detailed evaluation of the effect of the LHMC sampling size and the number of iterations, over the strong parameters detection and over the deviation with the monitored data, is also carried out and some conclusions are obtained. The proposed methodology is recommended for use as a method to evaluate the

energy savings achieved by retrofitting measures and as the first step of a more refined calibration stage since it reduces the number of input parameters to a manageable few and also narrows their individual range of variability.

2. Methodology

This study proposes an multi stage guided search approach for the calibration of detailed Building Energy Simulation (BES). To avoid an over-reliance on analyst knowledge, this methodology follows a clear structure and proven statistical methods which can be broken down into the following steps:

1. Gather building description and monitored data for the calibration and validation periods
2. Construct initial BES model including known and unknown input parameters
3. Definition of the best estimates for the unknown parameters and application of probability density functions to define their range of variation
4. Generation of a set of vectorial samplings for the unknown input parameters using LHMC method.
5. Run the set of simulations for all the vectorial samplings of input parameter vectors
6. Performance of Goodness of Fit calculations and rank solutions
7. Performance of a regional sensitivity analysis to test statistical significance of unknown parameters
8. Assignment new estimates to the strong parameters by narrowing the range of variation
9. Iterative process performance until regional sensitivity analysis doesn't detect new strong parameters

This multi-stage calibration process is presented in Fig. 1. A detailed description of the most important steps of the proposed methodology is presented below.

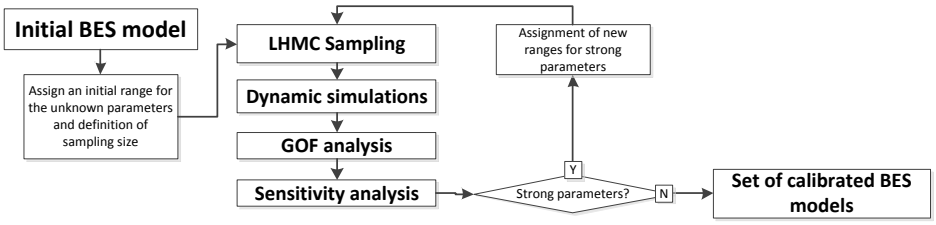

Figure 1: Multi-stage calibration process

2.1. Assignment of best values and range of variation of the parameters

This stage starts with the assignment of best estimates and range of variation of the unknown parameters to reduce the dimensionality of the search space. The assignment of best-guess estimates is usually based on the prescriptions of each manufacturer, on the data from the energy audit and on values coming from national normative. The assignment of the ranges of variation of the parameters consist in applying a probabilistic density function to each parameter. In [10] a criteria

to assign these probabilistic functions, depending on the classification of the unknown parameter, is suggested. Although some parameters can be discrete values, a uniform distribution, limited by minimum and maximum values, is applied to avoid a mixture between continuous and discrete distributions. The amplitude of the range of variation clearly determines the LHMC generation and, consequently, the global sensitivity analysis. To avoid outliers, these ranges of variation are characterized by probability density functions bounded by upper 95^{th} and lower 5^{th} probability threshold values.

2.2. Latin Hypercube Monte Carlo sampling and dynamic simulations

After assigning the probabilistic density functions to each range of variation of the parameters, a random sampling Latin Hypercube Monte Carlo (LHMC) is used to identify potential regions of local optima [15]. Monte Carlo random sampling was developed to generate a distribution of collections of parameter values from a multidimensional distribution. A square grid containing possible sample points is a Latin square if there is only one sample in each row and each column. A Latin hypercube is the generalization of this concept to an arbitrary number of dimensions. When sampling a function of k variables, the range of each variable is divided into n equally probable intervals; n sample points are then drawn such that a Latin Hypercube is created. This involves a generation of a sample from each probability density function and then, an evaluation of the model for each element of the sample.

The software package used to generate the LHMC sampling is R statistical package (http://www.r-project.org/). This program generates a LHMC by creating random permutations of the first n integers in each of k columns and then transforming those integers into n sections of a standard uniform distribution. Random values are then sampled from within each of the n sections. In order to avoid outliers, the standard uniform distribution is bounded by upper 95^{th} and lower 5^{th} probability threshold values. Once the sample is generated, the uniform sample from a column can be transformed to any distribution by using the quantile functions.

The LHMC trials will constitute the input parameters of BES model created with EnergyPlus [18]. Several batch simulations are carried out using jEPlus software [19], which allows a systematic running of parallel simulations and efficient collection of the outputs generated. These set of simulation trials will constitute the basis for further comparison with the monitored data and for detection of weak and strong parameters which can influence in the outputs.

2.3. Uncertainty analysis

Since calibration is a highly under determined problem, more than one solution may satisfy the objective function. In addition, it is erroneous to assume that a solution that satisfies the objective function is therefore implicitly correct. This is due to the many degrees of freedom that may produce good calibration overall even though the individual parameters may be incorrectly identified. Therefore, this step involves ranking the solutions based on statistical goodness-of-fit (GOF) criteria. This GOF is related to the calculation of the following dimensionless indices for each model [6].

- Normalized Mean Bias Error (NMBE):

$$NMBE = \frac{\sum(y_i - \hat{y}_i)}{n * \bar{y}} * 100 \quad [\%] \tag{1}$$

- Coefficient of Variation of the Root Mean Square Error (CVRMSE)

$$CVRMSE = \frac{\sqrt{\frac{\sum(y_i - \hat{y_i})^2}{n}}}{\bar{y}} * 100 \quad [\%] \tag{2}$$

Where $\hat{y_i}$ is the simulation predicted datum, y_i is the measured or monitored datum and n is the number of parameters in the model. Since the paper is centered in the calibration of buildings under free-floating situations, the measured datum is the indoor temperature and the predicted datum is predicted indoor temperature obtained from EnergyPlus simulation under free-floating conditions. According to [3], the considered overall goodness of fit (GOF) indicator will be the following:

$$GOF = \frac{\sqrt{2}}{2} * \sqrt{NMBE^2 + CVRMSE^2} \quad [\%] \tag{3}$$

Using these indices, we can filter out parameter vectors that result in high GOF numbers. Simulation trials with lower GOF numbers represent parameter vectors that provide a closer match to the measured data.

2.4. Sensitivity analysis to identify strong and weak parameters

The objective of a sensitivity analysis in our context is to identify the parameters that are strong (i.e. those that influence the statistical goodness-of-fit criteria denoted by equation 3) and those that are weak among the influential parameter sets that meet the prescribed satisfactory criteria. A systematic procedure to perform the sensitive analysis is developed and programmed within the R statistical package (http://www.r-project.org/). The Pearson chi square $\left(\chi^2\right)$ test [20]will be used to compare the parameter vectors distributions. The procedure is broken down in the following stages:

- Selection of the parameter vectors from the sets of simulations which fits the minimum GOF threshold. Since the chi square test accuracy is influenced by the sizes of the distributions to be compared, a filter to avoid that the number of "best candidates" overpass the 20% of the overall sampling size, is fixed.

- Calculation of the histograms of frequencies of the parameter vectors belonging to both the whole LHMC sampling and the set of best candidates. There is no optimal choice for the bin width of the histogram. For the chi-square approximation to be valid, the expected frequency should be at least 5 [21].

- Comparison of parameter vectors distributions using the Person chi square $\left(\chi^2\right)$ test. This χ^2 test is a statistical test applied to sets of categorical data to evaluate how likely any observed difference between the sets arose by chance (null hypothesis). In our case, it will be used to determine if the distribution of frequencies of the each parameter belonging to the best candidates is similar to the distribution of frequencies of the whole parameters vector. The null hypothesis is rejected when the *p*-value is smaller than a significance level (usually 5-1 %)

The parameters which are rejected from the null hypothesis are considered as strong parameters.

2.5. Re-assignment of new ranges of variation for strong parameters

Once the strong parameters are identified, a re-assignment of their probabilistic density functions is carried out by narrowing their range of variation an by assigning a new mean value, and another iteration starts. The method followed to re-assign these new ranges will respect the initial probabilistic density function assigned to each parameter at the beginning of the calibration procedure (see 1). The new ranges of variation will be obtained from the distribution of the parameter vectors belonging to the set of simulations which fitted the GOF threshold (best candidates). These new ranges, as well as the corresponding new mean values, will become the new input parameter for the next iteration. The iterative procedure is running until no new strong parameter is found.

3. Case study

3.1. The building and model

The case building is part of a project of retrofitting of old barracks placed in the Food and Agriculture Technological Scientific Park "PCiTAL" of Lleida in Spain (see Fig. 2). It consisted in the intervention in three existing buildings which were restructured as research offices for the University and for several food and agriculture firms. Each building has a H shape with three storeys. Before the retrofitting, the space among the buildings was formed by an atrium with trees. One of the main important actions has consisted in covering this connecting spaces with three glass green houses with shading and evaporative cooling devices. In Fig. 2, several pictures of the retrofitting process are shown.

One of the storeys of the second H-shaped buildings was selected as the reference office space where the calibration is performed. Within this storey, an office room which comprises half of the overall surface was equipped with the necessary monitoring equipment.

Figure 2: Gardeny office buildings. Inner view of the patio once they are covered by the glass green house structure, detail of the isolation layer and details of the solar shadings devices

In Fig. 3.1 the building energy simulation model is shown. It was created with EnergyPlus [18] and the OpenStudio graphical plug-in for SketchUp.

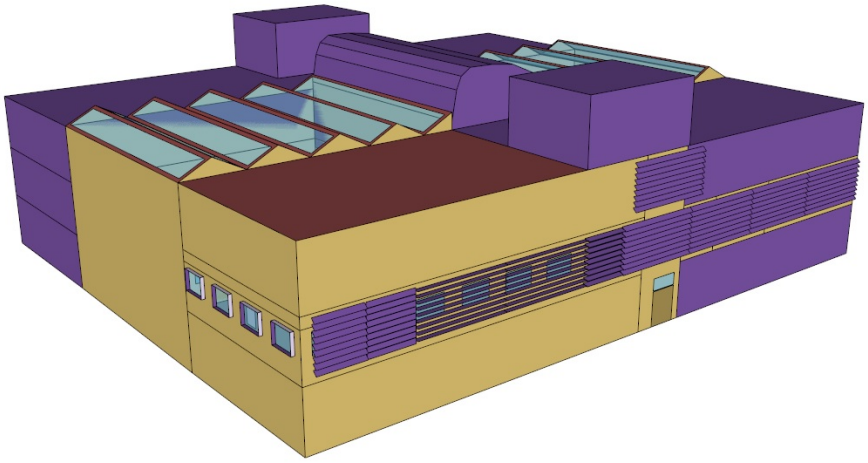

Figure 3: Building Energy model

The whole H shaped building was drawn in 3D (see Fig. 3.1), however, the defined thermal zones where limited to those corresponding with the storey where the reference office is located and its nearby and surrounding spaces. In total, 26 thermal zones were defined for the analysis. Since the office was unoccupied, no internal gains were defined and the external louvers were fixed to the position they were at the beginning. The boundary conditions of the adjacent spaces were simulated by imposing schedules to the indoor temperature of this zones, in coherence with the temperature gathered by the monitoring equipment.

3.2. Monitoring set-up

The reference office was equipped with a monitoring infrastructure for measuring indoor air temperature in several positions (see Figure 4).

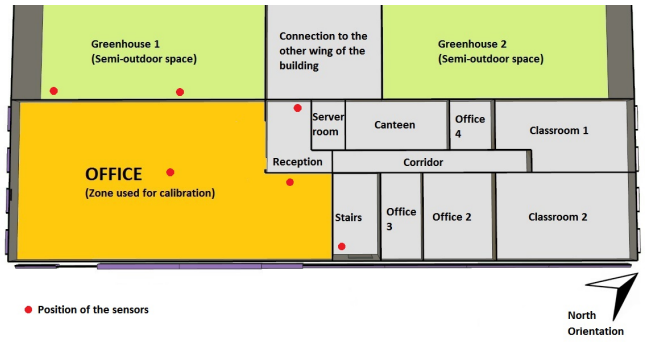

Figure 4: Building first floor plan and thermal zoning of the model

The data loggers Hobo U12-006, equipped with PT 100 thermo resistances and relative humidity sensors have been used. Fig. 4 shows the position of the sensors in the reference office floor plan and the thermal zoning. Each red point in Fig.4 represents a temperature sensor positioned at 1.5 m height. The temperatures of the adjacent storeys have been also measured: one temperature sensor was placed at the ground floor and one in correspondence of the second floor . The indoor air temperature has been logged at 15 min intervals and averaged hourly values are calculated. The office was unoccupied for a period of one month and this period was selected for monitoring purposes.

Weather data from a nearby meteorological station has been used: global horizontal solar radiation, outdoor dry-bulb temperature, dew point temperature, relative humidity, barometric pressure, daily rainfall, wind direction and speed have been collected at hourly values.

3.3. Monitoring period

The monitoring period comprises 30 days, from 11th October 2012 to 11th November 2012. The Fig. 3.3 shows the global horizontal radiation, the outdoor dry bulb temperature and the measured indoor temperature for this monitoring period.

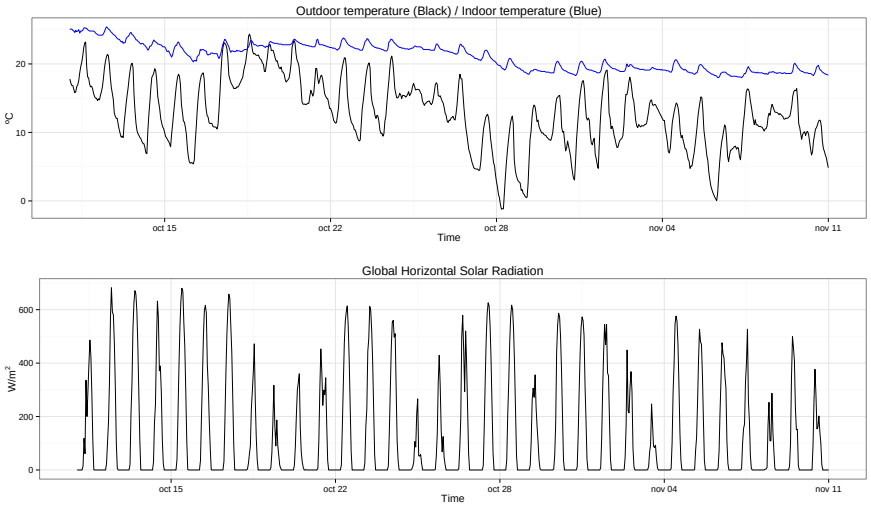

Figure 5: Monitored data of the calibration period

3.4. Assignment of best estimates to the unknown parameters

This paper is more centered in calibration of BES models based under free floating conditions, therefore, the main unknown parameters are related to air infiltration rate, physical and optical properties of the envelope materials and windows and internal mass due to furniture.

Two attempts for calibrating the BES have been performed: the first attempt defined a number of 49 unknown input parameters and the second attempt increased the number up to 53 parameters. The extra 4 parameters are related to the definition of the infiltration air flow rate. In the first attempt, a constant best estimate value of air changes per hour (ACH) was defined in all the thermal

zones. In the second attempt, the infiltration air flow rate was defined following the basic equation of [22]:

$$I = I_{design} \cdot \left[A + B \cdot |T_{zone} - T_{out}| + C \cdot (V_w) + D \cdot \left(V_w^2\right)\right] \quad (4)$$

In eq. 4, the variables A,B, C and D correspond to the extra parameters (50 to 53) of the second attempt. The parameter 44 varies from the fixed ACH in the attempt 1 to the design value, I_{design}, in attempt 2.

Number	PDF	Description	Coefficient of Variation (CV)
1 to 8	Normal	Thickness of the materials of the envelope (fabric, ceramic, plasterboard, rock wool...)	0.06 to 0.33
9 to 16	Normal	Conductivity of the materials of the envelope	0.05 to 0.2
17 to 24	Normal	Density of the materials of the envelope	0.03 to 0.17
25 to 32	Normal	Specific heat of the materials of the envelope	0.05 to 0.17
33	Normal	Thermal resistance of the south-west façade wall	0.06
34	Normal	Thermal resistance of the north-west façade wall	0.06
35 to 40	Normal	Equivalent surface of the internal mass	0.09 to 0.25
41 to 43	Normal	Specific power of electric equipment	0.08 to 0.4
44	Uniform	Air infiltration rate in "Office" Zone (I_{design} in attempt 2)	Min: 0.001ACH Max: 0.5 ACH CV: 0.22
45 to 46	Normal	Conductivity of window frame and glazing	0.2 and 0.11
47	Discrete (uniform)	Typology of window pane (4/13/4)	Min: 1.0 Max: 5.0 CV: 0.38
48	Discrete (uniform)	Thickness of air gap	Min: 0.006 Max: 0.012 CV: 0.19
49	Normal	Thermal absorptivity of gypsum	0.03
50	Uniform	Constant Term Coefficient (A in attempt 2)	Min: 0.0 Max: 1.0 CV: 0.58
51	Uniform	Temperature term coefficient (B in attempt 2)	Min: 0.0 Max: 1.0 CV: 0.58
52	Uniform	Velocity term coefficient (C in attempt 2)	Min: 0.0 Max: 1.0 CV: 0.58
53	Uniform	Velocity Squared term coefficient (D in attempt 2)	Min: 0.0 Max: 1.0 CV: 0.58

Table 1: Best estimates and range of variation of the unknown input parameters

The best guess values of the parameters and their corresponding probability density functions (PDF) are shown in Table 1. As it can be seen, different PDF are assigned to the parameters. Following the criteria defined by [10], normal distribution functions were applied to the physical characteristics of building materials, uniform distribution functions are assigned to air infiltration coefficients and a set of discrete values with the same likelihood is applied to both window panes typologies and air gap width. In the case of windows, they are all assumed as double pane windows (4/13/4 mm). The discrete value (1 to 5) corresponds to 5 glasses with different spectral properties which are placed in the outer or in the inner pane.

3.5. Latin Hypercube Montecarlo analysis

In a Monte Carlo analysis, a large number of evaluations of the model are performed with randomly sampled model input parameters [15]. These randomly input parameters are obtained from the PDF of Table 1. The combination of the randomly input parameters produces an input matrix with the following dimensions:

$$M = \begin{bmatrix} z_1^{(1)} & z_2^{(1)} & \dots & z_r^{(1)} \\ z_1^{(2)} & z_2^{(2)} & \dots & z_r^{(2)} \\ \dots & \dots & \dots & \dots \\ z_1^{(N-1)} & z_2^{(N-1)} & \dots & z_r^{(N-1)} \\ z_1^{(N)} & z_2^{(N)} & \dots & z_r^{(N)} \end{bmatrix} \tag{5}$$

Where z represents the random value of the parameters, r is the number of parameters ($r = 49$ for the first attempt and $r = 53$ for the second attempt), N is the sample size of trials and M is the corresponding vector solution matrix. Once the vector solution matrix is generated, batch Energy Plus simulations (using jEPlus [19]) are run for each of the LHMC trials. This generates the desired output vector, Y, for each row of matrix (5):

$$Y = \begin{bmatrix} y^{(1)} \\ y^{(2)} \\ \dots \\ y^{(N-1)} \\ y^{(N)} \end{bmatrix} \tag{6}$$

In order to facilitate a detailed analysis of the effect of the sample size over the accuracy of the results, several sample sizes have been generated: N=100; 200; 300, 400, 600, 800 and 1000.

3.6. Uncertainty analysis

A GOF below 11 % is recommended in [6] for trials acceptance, however, since free floating calibration require more demanding criteria, in this paper, a GOF $< 3\%$ is suggested to be considered for trials acceptance. Once the LHMC batch run is completed, the GOF index is computed for each trial. From here we can weed out those parameters vectors which result in GOF$<$ 3 %. The information contained in these "best" or feasible parameters vectors are then used to identify the strong parameters through a sensitivity analysis.

3.7. Sensitivity analysis

Following the methodology defined in Section 2, the Pearson chi square $\left(\chi^2\right)$ test [20]will be used to compare the parameter vectors distributions. The trials of parameters which fits the GOF criteria are compared with the overall sample population. The histograms of frequencies of both populations will be generated with the same number of bins (8 bins). The null hypothesis is rejected

when the p-value is smaller than a 5 % in the first attempt and smaller than 1 % in the the second attempt.

3.8. Re-assignment of new ranges of variation for strong parameters

For strong parameters which follow a normal distribution, the new values of mean and standard deviation will be the ones of the population formed by the random values generated with the LHMC which fit the threshold for the GOF ($< 3\%$). For strong parameters which follow a uniform distribution (parameter 44), the new values of maximum and minimum will be defined as the estimates of the 90 % quantile and of the 10% quantile of the population formed by the random values generated with the LHMC. In case of parameters which are discrete (parameters 47 and 48), the new discrete values generated with the LHMC will be limited to those achieving a frequency or probability over 60 % of the average probability of the sampled parameter population.

4. Discussion of the results

4.1. Evaluation of the strong parameters

The scope of this section is to evaluate the accuracy of the methodology to determine those parameters which influence in the output of the dynamic building simulation, namely the strong parameters. To evaluate this accuracy, the following factors of the methodology have been varied:

- The LHMC sampling size has been varied from 100 to 1000 trials
- The number of unknown parameters have been varied from 49 parameters to 53 parameters (see section 3.4)
- In the χ^2 test, the p-value threshold to select a parameter as strong has been varied. In attempt 1,the null hypothesis of the χ^2 test is rejected with a $p < 0.05$, while in attempt 2, it is rejected with a $p < 0.01$.

In Table 2, the detected strong parameters found in each attempt and for each sampling size, are summarized.

Sampling size	Attempt 1 (p-value < 0.05)		Attempt 2 (p-value < 0.01)	
	Strong parameters	Iterations	Strong parameters	Iterations
100	44	2	—	1
200	42,44	2	44	2
300	44	3	44,51	4
400	19,35,44	2	44,51	4
600	4,23,42,44	3	22,44,51	6
800	44,45	3	15,44,51	7
1000	6,7,31,36,44	4	6,7,15,30,44,51,53	16

Table 2: Strong parameters found in the attempt 1 and attempt 2

As it can be observed in Table 2, there is one clear strong parameter regardless the sampling size and the variation in the parameters of the sensitivity analysis, the parameter 44, which is related to the air infiltration rate in both attempts. Regarding the new parameters included in attempt 2, it can be seen that parameters 50 and 52 are not detected as strong parameters, therefore, their existence don't affect the calibration process. The parameter 51 is a very strong parameter and,

in coherence with equation 4, it follows the same performance than parameter 44. The parameter 53 is detected as strong parameter only in the highest sample size, which means that it is not so strong than parameter 51. These results, show that the air infiltration rate should include a temperature dependent factor (parameter 51) and, optionally, it can include a term affected by the squared power of the wind velocity (parameter 53). The effect of these two new parameters is not significant regarding the detection of other strong parameters and regarding the number of iterations needed to converge. They affect in the sample size because the addition of more unknown parameters increases the number of potential combinations and therefore, higher sample sizes are needed to achieve a more representative sampling population. In Table 2, it can also be seen that, for the same sample size, the number of iterations is greater in attempt 2 than in attempt 1, indicating that lower p-values clearly increase the precision in the detection of strong parameters by extending the number of iterations required to achieve the p-value threshold.

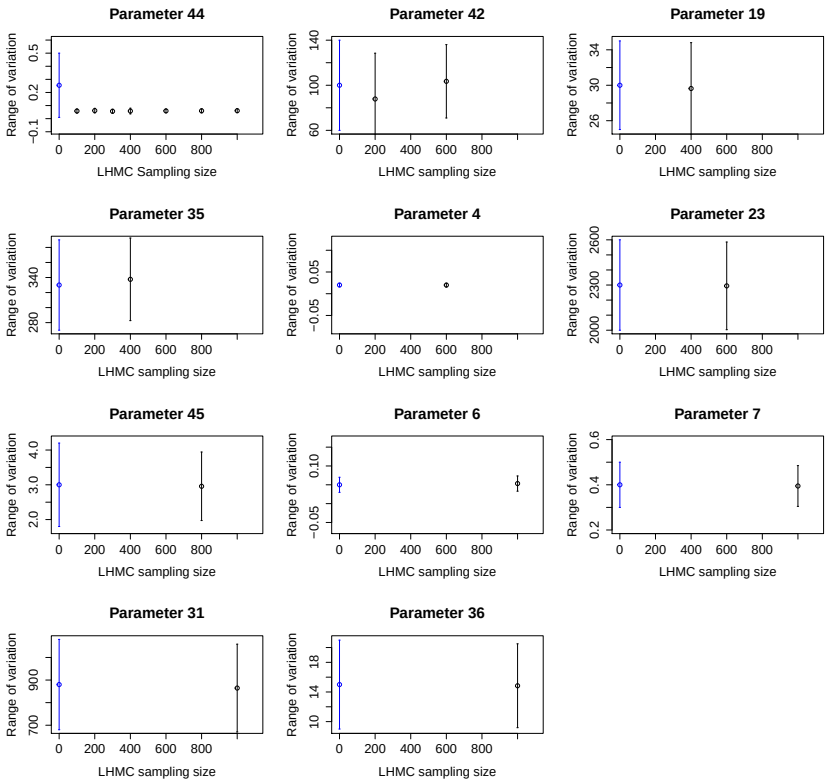

Figure 6: Ranges of variation of the strong parameters of attempt 1 versus the sampling size

In Table 2 more conclusions regarding the strong parameters detection can be obtained. It can be observed that in attempt 1, higher number of strong parameters are found, however, some of them are detected as strong in small sample sizes but they are not detected in higher sample sizes (parameters: 4, 23, 42, 19, 35, 45). They are even found in only one sample size. This behaviour is not repeated in attempt 2 and less strong parameters are found. Besides, in attempt 2, only

parameter 22 is found in only one sample size. The reason of this behaviour is related to the robustness of the χ^2 test. In attempt 1, the p-value threshold is higher than in attempt 2 and, although the difference is not very high, it causes this incongruence in the results of attempt 1.

In fig.4.1 and in fig.4.1 the variational range obtained for each strong parameter in the last iteration of each sampling size is shown. The variational range is limited by the minimum and maximum values of the PDF in those parameters with uniform distribution and by two times the standard deviation in those parameters with normal distribution. As can be seen in fig.4.1, most of the parameters of attempt 1 which are detected as strong in the sensitivity analysis, suffer almost no variation compared to its initial best estimated range. Only parameter 44 changes its range of variation. This lack of change in the range of variation means that these parameters are not really affecting the goodness of fit of the simulations since they remain as they were initially estimated and, in fact, they are performing as weak parameters.

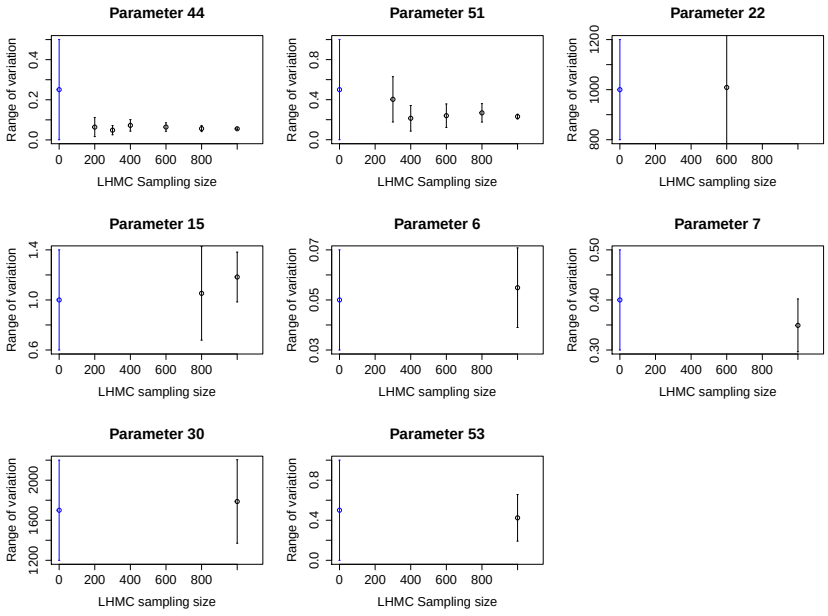

Figure 7: Ranges of variation of the strong parameters of attempt 2 versus the sampling size

In fig.4.1, it can also be observed that in many cases, the standard deviation of the strong parameter is higher than the initial best estimates and, consequently, the range of variation too. This is because in the stage of re-assignment of ranges of variation over the strong parameters, the initial PDF is applied in each new iteration regardless the probabilistic distribution followed by the parameter in the set of best trials. An improvement of the procedure would be to change the PDF to be assigned over the detected strong parameters in function of the real probabilistic distribution of the parameter values of the best trials. In fig.4.1 it can be seen that in the attempt 2, the behaviour is slightly different and almost all the detected strong parameters show narrowed ranges of variation. Only parameter 22 presents no change in the range of variation and, as happened in the first attempt, its range of variation is higher than in the initial best estimate. In fig.4.1 it can

also be observed that when the p-value threshold is reduced, a minimum sample size of 800-1000, or 15-19 times the number of unknown parameters, is needed to detect all the potential strong parameters.

Some conclusions regarding the strong parameters can be obtained:

- If the χ^2 test is used in the sensitivity analysis, the threshold of the p-value should be around 1 %.

- A minimum sample size of 15-19 times the number of unknown parameters is required to detect all the potential strong parameters.

- When a strong parameter is found, an evaluation of its change in the range of variation is needed to confirm its degree of strength.

- The air infiltration rate parameter (parameter 44) is an influencing parameter in both attempts and, from attempt 2, it can be concluded that two more terms are necessary for a proper air infiltration rate modeling: a temperature dependent term (parameter 51) and a term dependent on the squared power of the wind velocity (parameter 53). The addition of these two terms don't affect the strong parameters detection process but lead to an increase of the sample size since the number of potential combinations of parameters increases.

4.2. Evaluation of the goodness of fit

The effect of the sampling size over the GOF and the NMBE for each attempt is shown in fig.4.2 and in fig.4.2. As can be seen, the decrease of GOF and NMBE with the sampling size differs from attempt 1 to attempt 2. There is a more clear tendency of reduction in the attempt 2 and the final GOF and NMBE values are significantly smaller. It can also be seen that the whiskers of the box plots have little variation in the attempt 1 while they narrow very quickly with the sampling size in the attempt 2. This performance is mainly due to the change of the p-value criterion. The higher p-value criterion in the sensitivity analysis of the attempt 1 causes less precision in the strong parameters detection leading to the detection of "false" strong parameters and thus a wrong narrowing of parameters which are not really influencing parameters. This clearly affects the calculation of the GOF and causes this small variation of this indicator in the attempt 1.

Regarding the new parameters included in attempt 2, as previously mentioned, from the 4 new added parameters, only two are strong ones. The effect of the inclusion of these two parameters improves the GOF values of attempt 2 at the same level than other strong parameters. However, a detailed quantification of the isolated effect of this two parameters is not possible because this methodology of calibration, based on random sampling creation as variation of all the parameters at the same time, is not able to quantify the isolated effect of a single strong parameter or of a couple of them.

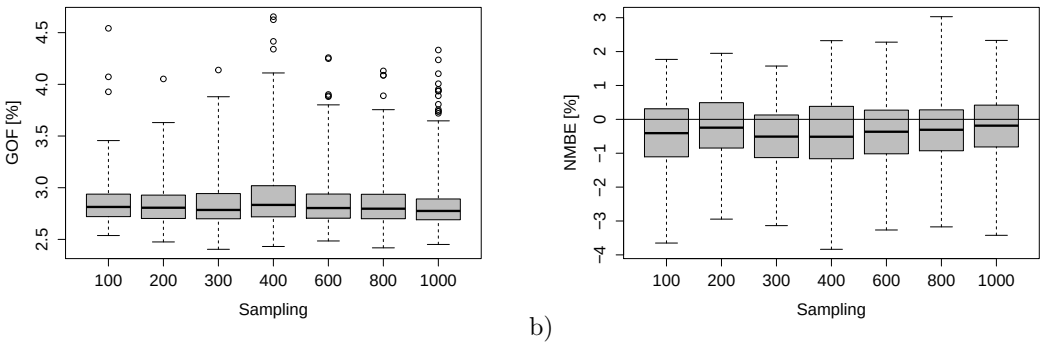

a) b)

Figure 8: Attempt 1: a) box plots of the variation of GOF with the sampling size; b) boxplots of the variation of NMBE with the sampling size

Analyzing more in detail the attempt 2, it can clearly be seen that the influence of the sample size is determinant to achieve low values of NMBE and GOF. The interquartile range (IQR) of the GOF varies from 10.4 % with a sampling size of 100 trials, to 0.13 % for a sampling size of 1000 trials. In the case of the NMBE, the IQR varies from 10.1 % for a sampling size of 100 trials to 0.88 % for sampling size of 1.000 trials. These higher NMBE and GOF values for the first sample size (100), are due to the fact that this sample size is too small to detect strong parameters and only one iteration was run in the calibration process. In fig.4.2 it is clearly appreciated that a minimum size of sampling is needed to assure a proper goodness of fit of the simulated results. The sample size should be in the range of 15-18 times the number of unknown parameters (as in section 4.1), however, if the computational resources are limited, a sample size of 6-11 times the number of unknown parameters would be enough to achieve the GOF criteria of 3 %.

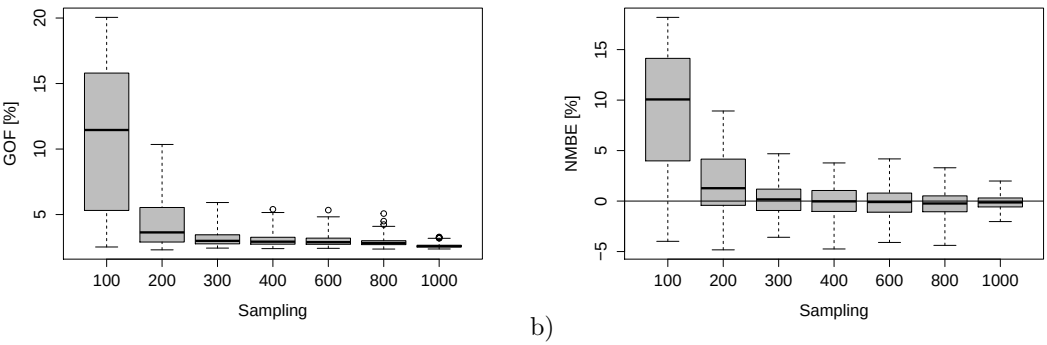

a) b)

Figure 9: Attempt 2: a) box plots of the variation of GOF with the sampling size; b) boxplots of the variation of NMBE with the sampling size

In Fig.4.2, density functions and qq-plots of the NMBE for all the trials of each sample size of attempt 2 are shown. The red line represents the theoretical normal distribution of the trials. The first sample size of 100 trials can be understood as non-calibrated solution since only 1 iteration was performed and no strong parameters are found. It can be seen that from sampling size of 800, the NMBE follows a standard normal probabilistic distribution function, meaning that the distribution of errors is symmetric and that the calibration of the BES fits with the goodness of fit criteria defined for free floating situations.

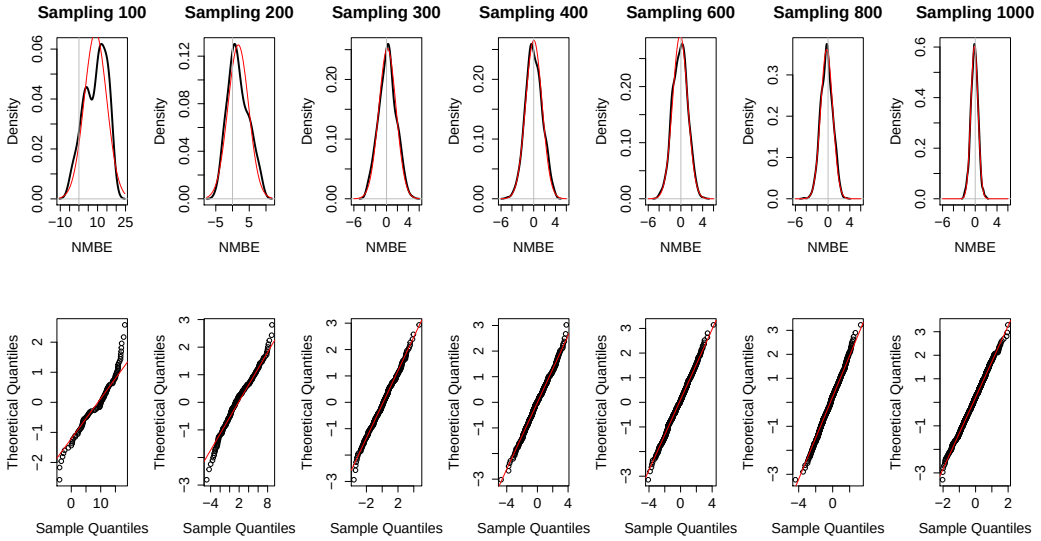

Figure 10: Density functions and QQ-plots of NMBE for each sample size of attempt 2. The red line is the theoretical normal distribution

4.3. Comparison between measured and simulated indoor temperature time series data

From the previous sections it is clear that the attempt 2 achieves better results than the attempt 1, therefore, the following analysis will be centered only on this attempt. In Fig.4.3 hourly time series plots of the predicted and measured indoor temperature are shown for all the sample sizes of attempt 2. The red line corresponds to the measured data in the monitoring period, the blue line corresponds to the mean of the set of trials of each sampling size and the gray shaded area corresponds to the 95^{th} probabilistic threshold range of solutions.

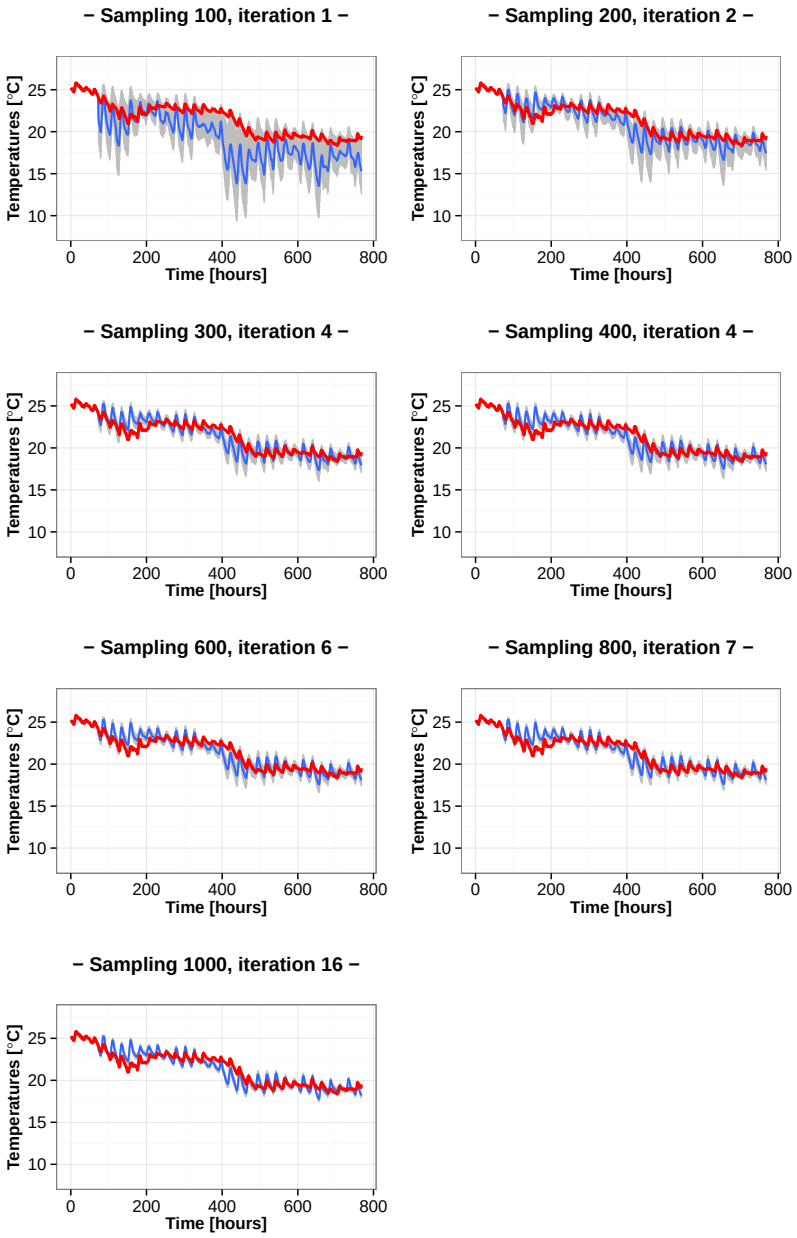

Figure 11: Hourly time series plots of the indoor temperature for all the sample sizes of attempt 2

In Fig.4.3 in can be seen that the difference between monitored and predicted results is much higher in the first sample (non-calibrated solution) than in the higher sample size (1.000). It can also be seen that from sample size 400, the main differences are related to the dispersion of the solutions of the trials, being greater in sample size of 400 than in sample size of 1000. However,

the mean values of the trial solutions (blue line) remain very similar from sample size 600 which is in coherence with the evolution of the GOF and NMBE. Looking at these figures, it can also be concluded that, although the goodness of fit criteria is achieved in great precision, the dynamics of the building is not captured well enough. It can be seen that the errors in some periods can reach values of around 3 °C and that this error is repeated in several times lags.

4.3.1. Residual analysis

In section 4.2. it was shown that the set of trials of the higher sampling sizes of BES are able to achieve the defined goodness of fit criteria; however, to determine the accuracy of the BES model as well as its capacity to capture the dynamics of the building with statistical significance, residual analysis will be carried out. The following tests will be performed: to check that the residuals are normally distributed with zero mean, that their variances do not vary with the effects being modeled and that the residuals are uncorrelated. These tests will be based on analysis of the plots of the residuals. The tests will be applied over all the sample sizes and the differences among them will evaluated. Assuming that for each sample size and time step there will be a number of residuals equivalent to the number of trials of the sample size, the mean of this residual vector will be calculated for every time step and the tests will be applied over this mean value of each sample size.

In Fig.4.3.1 the mean of residuals of each sample size is plotted versus time. As it can be observed, the residuals decrease with the increase of sampling size although the differences are almost negligible from sample size of 600 trials. It can also be seen that there are some peaks in the curves which reach error values of +2.7 °C and -2.5 °C and that these peaks are repeated in several time lags. This performance indicates a high probability of autocorrelation of the residuals.

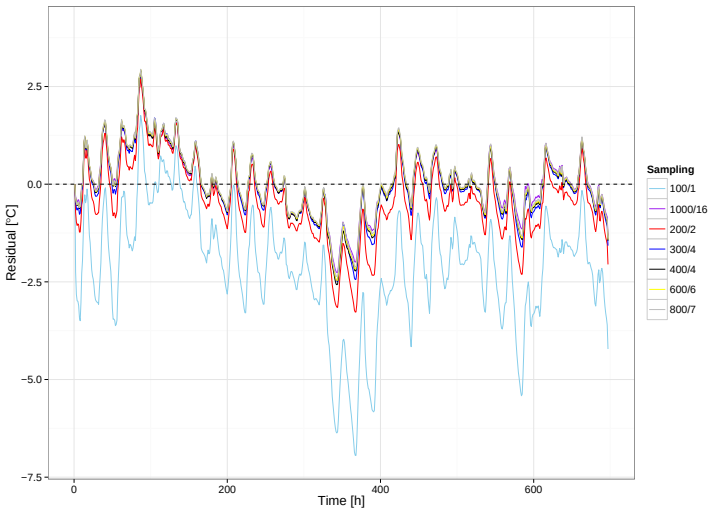

Figure 12: Plots of the mean of residuals versus time for each sample size of attempt 2

In Fig. 4.3.1 histograms of the means of residuals of each sampling size, as well as qq-plots of them, are shown. The red line of the upper figures represent the density function of the theoretical

normal distribution. As can be seen, from sampling size 300, the mean of the residuals means is zero, meaning that the means of residuals are well balanced over time. However, it is also clearly shown that they don't strictly follow a normal distribution since there is more density of residuals with very small values. This lack of normality in the residuals states, again, that the hypothesis of white noise will not be fulfilled.

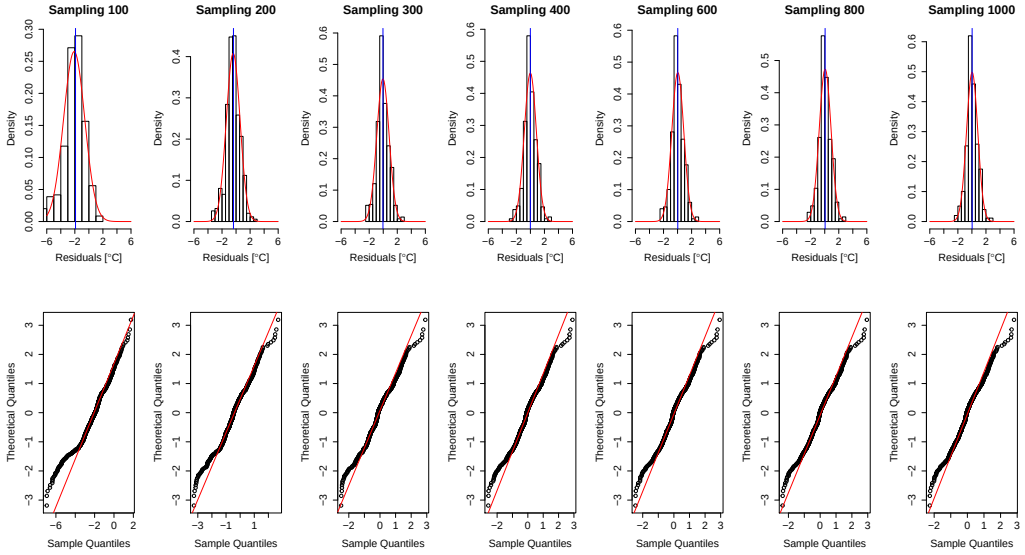

Figure 13: Histograms of residuals means for each sample size of attempt 2

In Fig. 4.3.1 the correlation plot between means of residuals and predicted indoor temperature is shown for each sample size. As it can be seen, the residuals are heteroscedastic since there are sub-populations that have different variabilities from others. It can be seen that the variability of residuals improves compared to the the initial situation (sampling of 100), however the pattern of data points shows some concentrations of residuals in between 18-20 °C and 22-24 °C, meaning that the error variance is correlated with the independent variable (regression error). In such a way, variance is said to be conditional (not constant) and its value depends on error itself. That is, conditional heteroskedasticity.

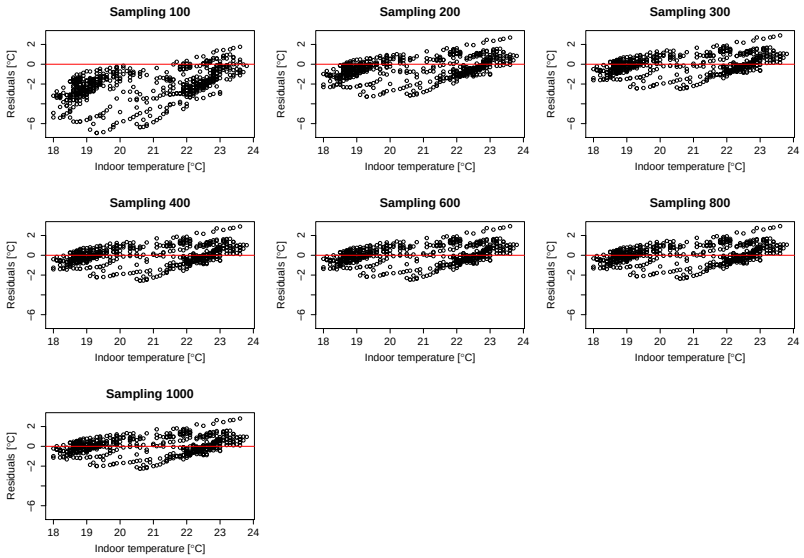

Figure 14: Plots of the mean of residuals of each sample size versus predicted indoor temperature

The last test to verify that the model is able to describe the dynamics of the system properly consists in analyzing if the residuals are autocorrelated. This will be done with the auto-correlation functions (ACF) plotted in Fig.4.3.1. Confidence bands of approximately 95% under the hypothesis that the residuals are white noise are also shown in blue. The ACF of the mean of residuals of each sample size clearly shows that the residuals are correlated and that white noise assumption is rejected.

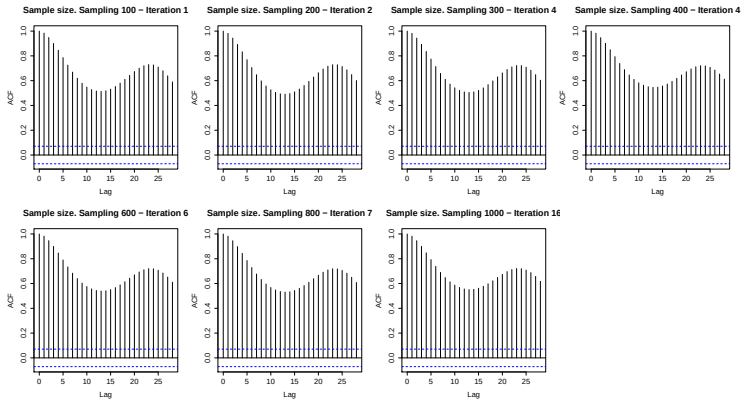

Figure 15: Auto correlation function of the mean residuals for each sample size of attempt 2

The tests performed in the previous figures clearly state that the BES model is not able to capture the dynamics of the building with enough statistical significance. This is in coherence with the requirements underlying the calibration methodology, which are more centered in determining the influencing parameters and achieving a GOF criteria rather than on capturing the real dynamics of the building.

To analyze potential outliers or systematic dependencies of the residuals on inputs, states or sampling size, correlation plots are obtained. The Fig. 4.3.1 shows the scatter plots among means of residuals, sampling sizes with the number of iterations per sample (sample/iteration) , global horizontal solar radiation (GHSRad), outdoor temperature (OutTemp) and wind velocity (WindVel). It can be seen that from sample size 600, the means of residuals are totally correlated between consecutive sampling sizes, meaning that there is almost no variation in their distribution, as was stated in previous sections. In Fig.4.3.1, it can also be seen that there is a strong correlation between means of residuals and outdoor temperature, while the correlation with wind and direct solar radiation is negligible. This result reveals that further model improvements should be implemented in the model to include this dependency with the outdoor temperature.

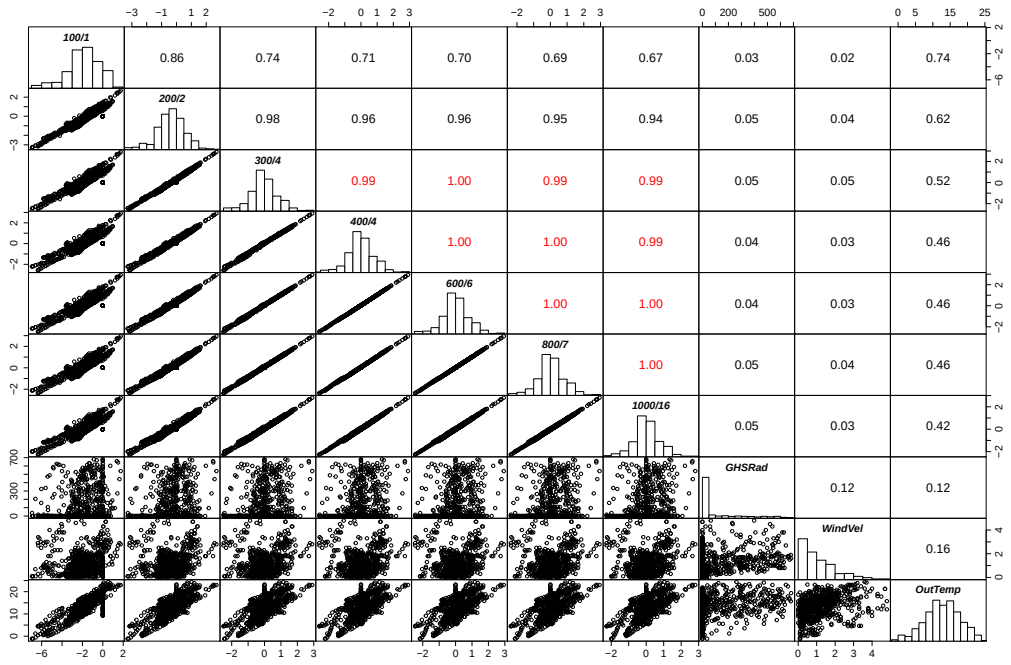

Figure 16: Correlation plots of the means of residuals among sampling size and number of iterations, direct solar radiation (*GHSRad*), wind velocity (*WindVel*) and outdoor temperature (*OutTemp*)

5. Conclusions

A multi-stage calibration method based on the combination of the Latin Hypercube Monte Carlo method (LHMC) and sensitivity analysis, is presented for application to guided coarse grid search

methods for calibrating BES under free floating situations. The method is useful for determining strong unknown input parameters and to obtain a set of top parameter combinations able to achieve a very precise goodness of fit criteria with the measured data.

Regarding the strong parameters detection, it can be concluded that the parameters related to the air infiltration are clearly influencing parameters (strong) and the inclusion of two parameters depending on the outdoor temperature and on the wind velocity are preferable for a better modeling this physical phenomenon. Other influencing parameters, which are not so strong, are those related to the conductivity and the specific heat of the envelope materials.

Another main conclusion is that the initial best estimated range of variation applied to the input parameters clearly constrains the results. A weak parameter can become strong if the initial range is extended or moved to other values, therefore, the result that a parameter is weak or strong should not be generalized but limited to the initial variational ranges. In addition to the re-assignment of narrowed ranges of variation over the strong parameters after each iteration, the PDF which is applied plays a crucial role in the sensitivity analysis precision. More flexible approaches allowing an adaptation of this PDF to the real probabilistic distribution of the strong parameters should be implemented as a further improvement of the methodology.

Regarding the sensitivity analysis, some more conclusions can be obtained: in cases where the Pearson χ^2 test is used as the sensitivity analysis, the threshold of the p-value should be around 1 %, since a small variation in this criterion has a big impact in both the detection of the strong parameters and in the goodness of fit of the simulations. The criteria to select a parameter as strong should also include a new test based on the level of change of the range of variation of the parameters after each iteration. In other words, to select a parameter as strong the posterior distribution, compared to the prior distribution, should have a considerable variation.

Regarding the optimal LHMC sample size, it can be concluded that a minimum sample size of 15-19 times the number of unknown parameters is necessary to detect all the potential strong parameters and to achieve the minimum number of iterations which guarantee acceptable GOF ranges.

The multi-stage guided search approach for the calibration of BES models presented in this paper, has also demonstrated a great precision in achieving minimum GOF criteria for a set of best trials, however it fails to capture the dynamics of the buildings. This approach is not able to fulfill the criteria of white noise for the residuals with enough statistical significance and presents some problems with autocorrelation of residuals. This lack of precision in capturing the building dynamics limits the application of this approach to analyses which aim at evaluating the influence of some building parameters such as the evaluation of the influence of renovation measures. This calibration methodology can also become the first step of a more precise building performance analysis methodology based on meta models development [17], and could improve the precision of the detection of the strong parameters of the meta model . In case the designers are interested in building dynamic analyses, other methods based on stochastic inverse modeling such as those developed by [23] and [24] are preferable.

Some further improvements will be oriented towards evaluating other sensitivity analysis methods such as some of those summarized in [9]. These sensitivity methods should be less sensitive to the sampling size, to the p-value threshold and should allow for a better ranking of the strength of the influencing parameters. Another main improvement will be centered in clustering some unknown related parameters to reduce the overall number parameters and to improve the control over the sensitivity analysis. A methodology similar to the one implemented by Calleja and Carrillo[25], but with multi-stage iteration processes, could be followed to limit the number of unknown parameters.

Nomenclature

n	number of parameters in the model (-)
y_i	measured indoor temperature (°C)
$\hat{y}_i$	predicted indoor temperature (°C)
$\bar{y_i}$	mean indoor temperature (°C)
z	random value of the parameters (-)
r	is the number of parameters (-)
N	is the sample size of trials (-)
M	vector solution matrix (-)
V_w	velocity of the wind (m/s)

References

[1] Carroll W. and Hitchock R.J. Tuning simulated building descriptions to match actual utility data: methods and implementation. *Ashrae Transactions, 99*, page 928.

[2] Francesca Campolongo, Jessica Cariboni, and Andrea Saltelli. An effective screening design for sensitivity analysis of large models. *Environmental Modelling & Software*, 22(10):1509–1518, October 2007.

[3] T. Reddy and I. Maor. Procedures for reconciling computer-calculated results with measured energy data. ASHRAE research project 1051 -, RP. Philadelphia, PA, 2006.

[4] A. Pedrini, F.S. Westphal, and R. Lamberts. A methodology for building energy modelling and calibration in warm climates. *Building and Environment*, 37:903–912, 2002.

[5] Yiqun Pan, Zhizhong Huang, and Gang Wu. Calibrated building energy simulation and its application in a high-rise commercial building in shanghai. *Energy and Buildings*, 39(6):651–657, June 2007.

[6] ASHRAE. *ASHRAE Guideline 14, Measurement of Energy and Demand Savings.* ASHRAE Standards Committe, 2002.

[7] International performance measurement and verification protocol (IPMVP). volume vol 1. 2002.

[8] K.L. Lomas and H. Eppel. Sensitivity analysis techniques for building thermal simulation programs. *Energy and Buildings*, 19:21–44, 1992.

[9] Wei Tian. A review of sensitivity analysis methods in building energy analysis. *Renewable and Sustainable Energy Reviews*, 20:411–419, April 2013.

[10] V. Corrado and H. E. Mechri. Uncertainty and sensitivity analysis for building energy rating. *Journal of Building Physics*, 33(2):125–156, 2009.

[11] F.S. Westphal and R. Lamberts. Building simulation calibration using sensitivity analysis. pages 1331–1338, 2005.

[12] J.C. Helton, J.D. Johnson, C.J. Sallaberry, and C.B. Storlie. Survey of sampling-based methods for uncertainty and sensitivity analysis. *Reliability Engineering & System Safety*, 91:1175–1209, 2006.

[13] I.A. Macdonald. Comparison of sampling techniques on the performance of montecarlo based sensitivity analysis. Glasgow, 2009.

[14] Daniel Coakley, Paul Raftery, Padraig Molloy, and Gearóid White. Calibration of a detailed BES model to measured data using an evidence-based analytical optimisation approach. In *Proceedings of 12th Conference of International Building Performance Simulation Association (IBPSA)*, 2011.

[15] Andrea Saltelli, Marco Ratto, Terry Andres, Francesca Campolongo, Jessica Cariboni, Debora Gatelli, Michaela Saisana, and Stefano Tarantola. *Global sensitivity analysis: the primer*. John Wiley & Sons, 2008.

[16] Bryan Eisenhower, Zheng O'Neill, Vladimir A. Fonoberov, and Igor Mezić. Uncertainty and sensitivity decomposition of building energy models. *Journal of Building Performance Simulation*, 5(3):171–184, 2012.

[17] Bryan Eisenhower, Zheng O'Neill, Satish Narayanan, Vladimir A. Fonoberov, and Igor Mezić. A methodology for meta-model based optimization in building energy models. *Energy and Buildings*, 47(0):292 – 301, 2012.

[18] B. Drury Crawley, L. K. Lawrie, O. Pedersen, and F. C. Winkelmann. Energy plus: Energy simulation program. *Ashrae Journal*, 42. nº 4:49–56, 2000.

[19] Y. Zhang. "Parallel" energyplus and the development of a parametric analysis tool. In *IBPSA 2009 - International Building Performance Simulation Association 2009*, pages 1382–1388, 2009. cited By (since 1996)6.

[20] Karl Pearson. X. on the criterion that a given system of deviations from the probable in the case of a correlated system of variables is such that it can be reasonably supposed to have arisen from random sampling. *Philosophical Magazine Series 5*, 50(302):157–175, 1900.

[21] NIST/SEMATECH e-handbook of statistical methods.

[22] CW Coblentz and PR Achenbach. Field measurements of air infiltration in ten electrically-heated houses. *ASHRAE Jounal*, 5(7):69–74, 1963.

[23] P. Bacher and H. Madsen. Identifying suitable models for the heat dynamics of buildings. *Energy and Buildings*, 43:1511–1522, 2011.

[24] C. Lodi, P. Bacher, J. Cipriano, and H. Madsen. Modelling the heat dynamics of a monitored test reference environment for building integrated photovoltaic systems using stochastic differential equations. *Energy and Buildings*, 50:273–281, 2012.

[25] Gloria Calleja Rodríguez, Antonio Carrillo Andrés, Fernando Domínguez Muñoz, José Manuel Cejudo López, and Yi Zhang. Uncertainties and sensitivity analysis in building energy simulation using macroparameters. *Energy and Buildings*, 67:79–87, December 2013.

Integrated development and calibration of a dynamic model for natural ventilated photovoltaic components

J. Cipriano[a]*, G. Houzeaux [b], G. Mor [a], J. Carbonell [c], S. Danov [c], J. Marti-Herrero[c]

[a] *Centre Internacional de Mètodes Numèrics a l'Enginyeria (CIMNE), Building Energy and Environment Group,CIMNE-UdL classroom c/Pere de Cabrera s/n , 25001, Lleida, Spain*

[b] *Barcelona Supercomputing Center (BSC-CNS),08034, Barcelona, Spain*

[c] *Centre Internacional de Mètodes Numèrics a l'Enginyeria (CIMNE), Building Energy and Environment Group, c/Rambla St Nebridi 22 , 08222 Terrassa, Spain*

* *Corresponding author: Centre Internacional de Mètodes Numèrics a l'Enginyeria (CIMNE), Building Energy and Environment Group. CIMNE-UdL Classroom. c/Pere de Cabrera s/n. CREA building. Office 1.15, 25001. Lleida, Spain. e-mail: cipriano@cimne.upc.edu, phone: +34 973003574, fax: +34 973003575*

Abstract

For the last years, many authors have been working in the evaluation of the energy performance of ventilated PV components. Many theoretical models have been developed. All these detailed studies have lead to an increase in the knowledge of the heat transfer processes that occur within these complex PV components, however, there are still many unclear fields: the selection of the best convective heat transfer coefficients; the evaluation of the internal solar reflections and of the air mass flow rate in turbulent flows.Furthermore, very few studies addressed the calibration of the models following a systemic approach which could be further replicated. There is also a lack of studies which addressed, based on semi-automated approaches, the identification of strong and weak parameters of the model. In this research, a contribution to achieve deeper knowledge in the energy performance of ventilated PV components is proposed by the development of a very flexible dynamic simulation model and the integration of a calibration methodology previously developed and validated. A systemic approach to identify strong and weak parameters of the model is also adapted to the specific conditions of these components. This calibration methodology is recommended for use as a method to evaluate mid to long term predictions of the thermal and electrical energy produced by ventilated PV components and to achieve high goodness of fit with the measured data.

1. Introduction

For the last years, many authors have been working in the field of double skin ventilated façades with and without building integrated photovoltaics (BIPV). Since the 1990's Hans Bloem, [1, 2, 3, 4] has been carrying out an intensive characterization of PV ventilated façades, with and without ventilated air gaps. Some European funded projects have been actively supporting this work, PASSLINK, PV-HYBRIDPAS and IMPACT [5]. Between 1999 and 2000, Mei et. [6] undertook the theoretical analysis and monitoring of the Mataro's public library building, which had the first PV ventilated façade in Europe. More recently, the treatment of the induced flow and the heat transfer at the air gap and the surfaces of a natural ventilated double skin façade has been progressively refined by Brinkworth [7, 8, 9, 10]. Concerning to the mathematical model to define the energy performance of such façades, simplified methods have been proposed by Ursula Eicker [11]and Li Mei [6] More sophisticated models for double skin façades have bee also developed by Debora Faggembau [12] and Dirk Saelens [13, 14]. All these authors have assumed forced flow correlations for the convection heat transfer coefficient and they didn't consider the

effect of the asymmetry in the laminar boundary conditions. Saelens [15] also made a review of several ways to model the air channel and he concluded that a single volume model with linear variation of the average temperature has he same accuracy than finite difference schemes. In parallel, Yun et. [16] used the software ESP-r to model the overall energy performance of a ventilated PV façade and defined a new index of effectiveness which included the reduction in artificial lighting, the thermal energy and the electrical energy produced. In this study, a parameter optimization has been performed but without a contrast with experimental measures.

Although these detailed studies have lead to an increase in the knowledge of the heat transfer processes that occur within semi transparent natural ventilated PV components, there are still many unclear fields such as: the selection of the best convective heat transfer coefficients; the evaluation of the internal reflections of the direct solar radiation and the evaluation of the air mass flow rate in non-developing turbulent flows. To get more insights in these unclear items, some authors have combined the development of transient simulation models with optimization and calibration techniques. Remi Charron et. [17] implemented a one-dimensional finite-difference thermal model with an algorithm that iteratively determined which convective heat transfer coefficient correlation to use for each surface. More recently,Yang et. [18] performed a study of the design options of BIPV/T and analyzed the effect of adding multiple inlets. They developed a dynamic model based on lumped capacitance simplification and calibrated the results with a stationary solar simulator. However, comparison or calibration with real outdoor conditions has been carried out Very recently, Assoa et. [19] performed a dynamic study of a new design of a hybrid PV/T system. They developed a transient model, based on TRNSYS, and a validation with real outdoor measurements has been carried out. Although the comparison was very detailed, no systematic approach was suggested an the calibration process remained dependent on the experience of the developer.

From these experiences it becomes evident that there is a lack of detailed studies on how to properly fill the gap between the results of theoretical models and the measured real energy performance of these complex BIPV components. Besides, very few studies addressed the analysis of the parameters which have more influence in the energy performance of ventilated PV components, following a systemic approach which could be further replicated with other configurations and working conditions.

In this research, a contribution to achieve deeper knowledge in the energy performance of ventilated PV components is proposed by the developing and implementation of a very flexible dynamic simulation model. Previously developed and validated systemic approaches to identify strong and weak parameters of the model [20], will be adapted to the specific conditions of ventilated PV components and will be integrated in an overall calibration procedure. This calibration methodology is recommended for use as a method to evaluate mid to long term predictions of the thermal and electrical energy produced by ventilated PV components and to achieve high goodness of fit with the measured data.

2. Dynamic simulation model

2.1. Energy transfer within the ventilated PV component

The figure 1 shows the energy transfer processes which occurs when a ventilated PV component is exposed to the solar radiation.

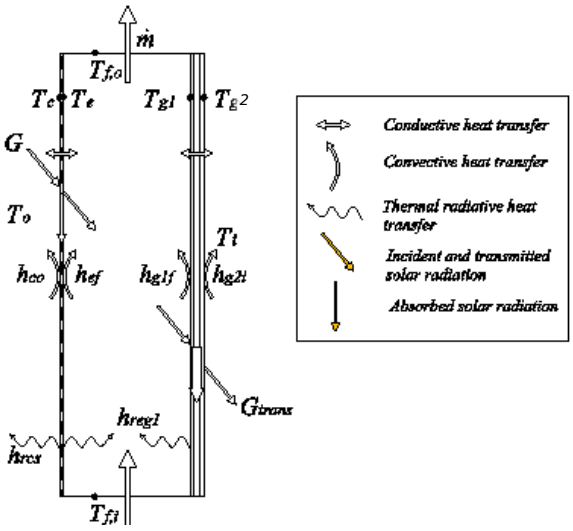

Figure 1: Energy transfer within the ventilated PV component

Air enters the ventilated PV component from the bottom inlet with an average inlet temperature ($T_{f,i}$), which is assumed equal to the ambient temperature (T_a). Warm air exits from the top of the chimney at outlet average temperature ($T_{f,o}$). Within the PV module, two average temperatures are considered as boundary temperatures:(T_c) for the front side of the PV module and (T_e) for the back side. The rear facing material is formed by a single layer and two average temperatures are defined: the average temperature of the front side, which is contact with the air gap (T_{g1}), and the average temperature of the back side(T_{g2}).

2.2. Programming modules

TRNSYS 16[21] is the software chosen to program the dynamic model to simulate the energy performance of the ventilated PV component. Three TRNSYS types, programed following Fortran 90 language, have been set up and integrated within the TRNSYS environment :

1. The PV laminate type (Type 154): It is a transient numerical one-dimensional heat conduction scheme with three numerical domains corresponding with the three layers of the PV module (front glas layer, PV cells layer, back layer of Tedlar).
2. The air channel type (Type 157): It is based on a stationary energy and mass balance over a single volume formed by the 2D geometry of the air channel.
3. The rear facing material type (Type 159): It is a transient numerical one-dimensional heat conduction scheme with a single numerical domain corresponding to the rear facing material.

All the types are dynamically coupled by the TRNSYS sequentially solver: the heat convection sources obtained from the first and third types ($q"_{ef}$ and $q"_{g1f}$) are transferred to the second type as uniform heat flux boundary conditions (UHF). Once the heat transfer coefficients, the air mass flow rate and the average wall temperatures (T_e and T_{g1}) are obtained within this type, they are returned back to the first and third types. Within the third and first types, the wall temperatures and the heat conduction sources are calculated. The heat convection sources towards the air channel are again calculated adding or subtracting the radiative heat flux ($q"_{reg1}$) . This is an iterative process which converges each time step.

2.3. Conduction heat transfer

Conduction heat transfer within the PV laminate

The semitransparent PV laminate is formed by three layers: the exterior layer is clear glass, the middle layer is divided between the PV cells and the EVA and the third layer is Tedlar or glass.

The governing equation is the energy conservation equation within a solid. Assuming the Fourier law for the thermal diffusive term and considering the thermal capacitance of the PV cells and the glass in the transient term, the governing equation is defined as :

$$\rho c_p \frac{\partial T}{\partial t} - \nabla \cdot (k \nabla T) = Q \tag{1}$$

The boundary conditions are a combination of Dirichlet and Robin conditions:

$$T = T_e \text{ in } x = e_{PV}$$

$$k \nabla T \cdot \mathbf{n} = \overline{h}_{ca} (T_a - T_c) + h_{rcs} (T_s - T_c) \text{ in } x = 0$$

If we express the equation 1 in their integral form, we apply the Galerkin approximation with the weight function (υ), and the divergence theorem, we obtain:

$$\int_\Omega \rho c_p \frac{\partial T}{\partial t} \cdot \upsilon d\Omega + \int_\Omega k (\nabla T \cdot \nabla \upsilon) d\Omega = \int_\Omega Q d\Omega + \int_{\Gamma_N} \upsilon \cdot (K \nabla T \cdot \mathbf{n}) d\Gamma \tag{2}$$

The temporary term is discretized as an implicit upwards finite difference scheme and varies between an Euler scheme for the first time step, and a Cranck-Nicholson scheme for the following time steps:

$$\frac{dT}{dt} = \frac{T^{n+\theta} - T^n}{\theta \delta t} \tag{3}$$

Where n is the number of time step and θ is the temporary coefficient ($\theta = 1$ for Euler scheme; $\theta = 0.5$ for the Cranck-Nicholson). Substituting the equation 3 in the equation 2:

$$\int_\Omega \rho c_p \frac{T^{n+\theta} - T^n}{\theta \delta t} \cdot \upsilon d\Omega + \int_\Omega k \left(\nabla T^{n+\theta} \cdot \nabla \upsilon\right) d\Omega = \int_\Omega Q^{n+\theta} d\Omega + \int_{\Gamma_N} \upsilon \cdot \left(k \nabla T^{n+\theta} \cdot \mathbf{n}\right) d\Gamma \tag{4}$$

To solve the equation 4, a one dimension finite element mesh (FEM), formed by linear elements, is proposed. An scheme of the finite element mesh is shown in the figure 2.

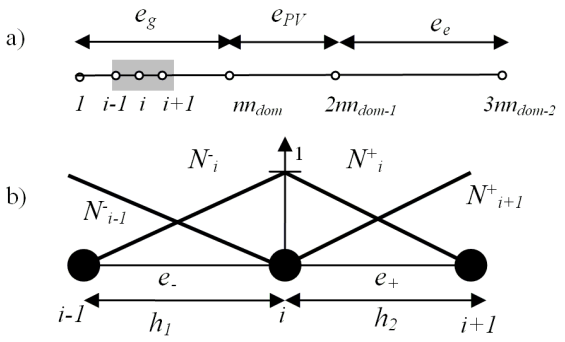

Figure 2: a) Mesh of the PV laminate. b) Node i of the Finite Elements Mesh

In the figure 2, nn_{dom} is the number of nodes in each layer. If we apply the equation 4 over each finite element and we substitute v by the linear shape functions (N_i^+ ,N_i^-, N_{i-1}^-, N_{i+1}^+) ,showed in the figure 2, we can obtain a discretized system of equations defined as:

$$[C] \cdot \left[T^{n+\theta}\right] = \left[r^{n+\theta}\right] \tag{5}$$

Where $[C]$is the coefficients array, $\left[T^{n+\theta}\right]$is the array of the temperatures at time step $n+\theta$ and $\left[r^{n+\theta}\right]$ is the residuals array. The array $[C]$ is a non linear three-diagonal array, formed by three vectors: $[a_i]$ is the lower diagonal $[b_i]$ is the middle diagonal and $[c_i]$ is the upper diagonal. The values of the terms in each array depend on the layer. For the nodes which are within each layer we have the general expression:

$$\left(\frac{\rho_i c_{p_i} h_i}{6\theta\delta t} - \frac{k_i}{h_i}\right) T_{i-1} + \left(\frac{\rho_i c_{p_i} 2h_i}{3\theta\delta t} + \frac{2k_i}{h_i}\right) T_i + \left(\frac{\rho_i c_{p_i} h_i}{6\theta\delta t} - \frac{k_i}{h_i}\right) T_{i+1} \tag{6}$$

The volumetric heat source has two different expressions, depending on the layer. If $i = nn_{dom} + 1 \,\text{to}\, 2nn_{dom} - 2$ or $i = nn_{dom}$ then:

$$Q_i = \frac{1}{h_i}\left(S_{gi} - q_e"\right) \tag{7}$$

If $i = 2 \,\text{to}\, nn_{dom} - 1$ and $i = 2nn_{dom}$ to $3nn_{dom} - 3$ or $i = 2nn_{dom} - 1$ then:

$$Q_i = \frac{S_{gi}}{h_i} \tag{8}$$

The properties of the second layer (PV cells and EVA) are affected by the packing factor (P). It can be defined as the ratio between the equivalent surface of PV cells and the equivalent surface of the semi transparent spaces between the PV cells:

$$P = \frac{A_{PV}}{A_T};\; A_{tr} = A_T\,(1 - P) \tag{9}$$

The terms for the nodes which are in the borders ($i = nn_{dom} \,\text{or}\, i = 2nn_{dom} - 1$) have the following general expression:

$$\begin{aligned}\left(\frac{\rho_{i-1} c_{p_{i-1}} h_{i-1}}{6\theta\delta t} - \frac{k_{i-1}}{h_{i-1}}\right) T_{i-1} + \left(\frac{\rho_{i-1} c_{p_{i-1}} h_{i-1}}{3\theta\delta t} + \frac{\rho_i c_{p_i} h_i}{3\theta\delta t} + \frac{k_i}{h_i} + \frac{k_{i-1}}{h_{i-1}}\right) T_i \quad + \\ + \left(\frac{\rho_i c_{p_i} h_i}{6\theta\delta t} - \frac{k_i}{h_i}\right) T_{i+1} + \frac{\rho_{i-1} c_{p_{i-1}} h_{i-1}}{6\theta\delta t} T_{i-1}^n + \\ + \left(\frac{\rho_{i-1} c_{p_{i-1}} h_{i-1}}{3\theta\delta t} + \frac{\rho_i c_{p_i} h_i}{3\theta\delta t}\right) \frac{1}{3} T_i^n + \frac{\rho_i c_{p_i} h_i}{6\theta\delta t} \frac{1}{6} T_{i+1}^n\end{aligned} \tag{10}$$

The boundary conditions affect the first and last nodes of the arrays. For the first node ($i = 1$):

$$[c_1] = \frac{\rho_1 c_{p_1} h_1}{6\theta\delta t} - \frac{k_1}{h_1} \tag{11}$$

$$[b_1] = \frac{\rho_1 c_{p_1} h_1}{3\theta\delta t} + \frac{k_1}{h_1} + \overline{h}_{ca} T_a + h_{rsc} T_s \tag{12}$$

Where the subindex $_1$ corresponds to the first node of the outer clear glass layer. For the last node ($i = 3nn_{dom} - 2$):$[b_{3n-2}] = 1; [r_{3n-2}] = T_e$.

The system of equations is solved using a direct three-diagonal algorithm (TDMA). Once the temperatures of each node are obtained, the conduction heat flux of the element which is contact

with the air channel ($q"_{e,cond}$), is calculated as:

$$q"_{e,cond} = k_{3nn_{dom}-2} \frac{T^{n+\theta}_{3nn_{dom}-3} - T_e}{h_{3nn_{dom}-2}} \quad (W/m^2) \tag{13}$$

Conduction heat transfer within the rear facing material

The rear facing material can be formed by an opaque or a transparent solid sheet. The governing equation which defines the heat conduction within this material is the equation 4. The implemented FEM discretization is the same as the PV module (see equations 5,6 and 10), with the volumetric heat source expressed as the equation 8. The boundary conditions will be the opposite of the PV laminate (Dirichlet in $x = 0$ and Robin in $x = e_g$; with e_g being the thickness of the rear facing material).

Once the temperatures of each node are obtained, the conduction heat flux of the element which is contact with the air gap ($q"_{g1,cond}$) , is calculated with the equation 13 but substituting the temperature $T^{n+\theta}_{3nn_{dom}-3}$ by the temperature of the second node, and the temperature T_e by the temperature T_{g1}.

2.4. Heat and mass transfer within the ventilated air gap

The air channel is modeled through a stationary one-dimensional volume with a linearly temperature variation in the vertical direction. The boundary conditions at the walls are uniform convection heat fluxes. Three different working conditions are possible:symmetric UHF ($q"_{ef} = q"_{g1f}$), asymmetric UHF ($q"_{ef} \neq q"_{g1f}$) and asymmetric UHF with one adiabatic wall: ($q"_{ef}\,; q"_{g1f} = 0$). The determination of the convection heat fluxes depends on the conduction heat fluxes (see equation 13) and the thermal heat radiation fluxes between the back side of the PV laminate and the front side of the rear facing material: $q"_{ef} = q"_{e,cond} + q"_{rg1e}$; $q"_{g1f} = q"_{e,cond} + q"_{reg1}$

The sub indexes $_{g1e}$ and $_{eg1}$ point out the direction of the radiative heat flux. The positive or negative signs depends on the balance between the temperature of last node of the PV laminate (T_e) and the temperature of the first node of the rear facing material (T_{g1}) .

The governing equation which defines the heat transfer within the air gap is the conservative energy equation for incompressible flows:

$$\rho c_p \left(\frac{dT}{dt} + \mathbf{u} \cdot \nabla T \right) - \nabla \cdot (k \nabla T) = Q \tag{14}$$

Assuming a stationary situation within each time step and uniform UHF boundary conditions, we can obtain the following expression:

$$\dot{m} c_p dT = (q"_{ef} + q"_{g1f})\, W dy \tag{15}$$

The equation 15 can be integrated at a determined height to obtain the cross average of the air temperature at this height:

$$\int_{T_{f,i}}^{T_{f,y}} \dot{m} c_p dT = \int_0^y (q"_{ef} + q"_{g1f})\, W dy \tag{16}$$

$$\dot{m} c_p \left(T_{f,y} - T_{f,i}\right) = (q"_{ef} + q"_{g1f})\, W y \tag{17}$$

$$T_f(y) = T_{f,i} + \frac{(q"_{ef} + q"_{g1f})\, W y}{\dot{m} c_p} \tag{18}$$

The outlet and mid height temperatures are then determined as:

$$T_f = T_{f,i} + \frac{(q"_{ef} + q"_{g1f})\,WH}{2\dot{m}c_p}$$

$$T_{f,o} = T_{f,i} + \frac{(q"_{ef} + q"_{g1f})\,WH}{\dot{m}c_p}$$

Assuming the Newton law of cooling for the heat convection sources, and making some arrangements, the average temperatures of the back side of the PV component (T_e) and of the front side of the rear facing material (T_{g1}), can be obtained with the following mathematical expressions:

$$T_e = T_{f,i} + \frac{q"_{ef}}{\overline{h}_{ef}} + \frac{(q"_{ef} + q"_{g1f})\,WH}{2\dot{m}c_p} = T_f + \frac{q"_{ef}}{\overline{h}_{ef}} \tag{19}$$

$$T_{g1} = T_{f,i} + \frac{q"_{g1f}}{\overline{h}_{g1f}} + \frac{(q"_{ef} + q"_{g1f})\,WH}{2\dot{m}c_p} = T_f + \frac{q"_{g1f}}{\overline{h}_{g1f}} \tag{20}$$

Convection heat transfer coefficients

The average convection heat transfer coefficients of the equations 19 and 20 are derived from the average Nusselt numbers $\left(\overline{Nu}\right)$:$\overline{h} = \frac{\overline{Nu}\cdot k}{D_h}$. The air flow situation is assumed as natural convection. Since the boundary conditions change every time step, a combination of laminar and turbulent regimes can occur within each simulation period. Besides, the boundary conditions at the walls of the air gap also vary, meaning that the condition of hot or cold wall is assigned every time step.

In [22] a detailed study of the more suitable heat transfer correlations for laminar regime and several boundary conditions is carried out. Following the conclusions of this research, the $\overline{Nu}$ correlations which are implemented in the dynamic model are summarized in the Table 1. These correlations will be applied to both walls alternatively depending on the combination of UHF boundary conditions of every time step.

Authors	Proposed correlation	Comments
Symmetric UHF		
[23]	$\overline{Nu}_b = \left[\left(\overline{Nu}_{fd}\right)^{-3.5} + \left(\overline{Nu}_{plate}\right)^{-3.5}\right]^{-1/3.5}$ $\overline{Nu}_{fd} = 0.29\,(Ra_b")^{1/2}$ $\overline{Nu}_{plate} = c\overline{H_l}\,(Ra_b")^{1/5}$ $\overline{H_l} = \frac{6}{5}\left(\frac{Pr}{4+9\sqrt{Pr}+10Pr}\right)^{1/5}$	$c = 1.15$
Asymmetric UHF with adiabatic wall		
[23]	$\overline{Nu}_b = \left[\left(\overline{Nu}_{fd}\right)^{-3.5} + \left(\overline{Nu}_{plate}\right)^{-3.5}\right]^{-1/3.5}$ $\overline{Nu}_{fd} = 0.29\,(Ra_b")^{1/2}$ $\overline{Nu}_{plate} = c\overline{H_l}\,(Ra_b")^{1/5}$ $\overline{H_l} = \frac{6}{5}\left(\frac{Pr}{4+9\sqrt{Pr}+10Pr}\right)^{1/5}$	$c = 1.07$
Asymmetric UHF		
[24]	$\overline{Nu}_{wh} = \frac{30q_{wh}+30q_{wc}}{6q_{wh}+q_{wc}}$ $\overline{Nu}_{wc} = \frac{30q_{wh}+30q_{wc}}{q_{wh}+6q_{wc}}$	correlations developed for forced convection and asymmetric UHF

Table 1: Correlations of $\overline{Nu}$ for laminar free convection and UHF boundary conditions

In the analysis carried out by [22], it was found that the situations of turbulent free convection perform as single isolated vertical plates since there is very few interaction between the boundary

layers of the walls. The correlation of [25] has been implemented in the dynamic model for the turbulent situations regardless the asymmetry in the boundary conditions:

$$\overline{Nu}_H = \left(0.825 + 0.328 Ra_H^{1/6}\right)^2 \tag{21}$$

In the case of situations with regime in the transition to turbulent and asymmetric UHF, the correlation of Churchill [25]will be applied to the hot wall and the correlation of Rohsenow [23], originally obtained from laminar situations, wil be applied to the cold wall.

Air mass flow rate

Pure natural ventilation regime is considered for the dynamic model and no wind effects are taking into consideration in the calculation of the air mass flow rate. The dynamic model includes two different procedures to determine the air mass flow rate within the ventilated air gap.

The first procedure is based on the studies of the air mass flow rate within natural ventilated cavities carried out by [26] and it follows the next equation:

$$\dot{m} = C_d \frac{\rho_{f,o} A_o}{\sqrt{1 + \frac{A_o}{A_i}}} \sqrt{\frac{2gH\left(T_f - T_a\right)}{T_a}} \tag{22}$$

The second procedure is based on the methodology developed by [8, 10, 9, 7]. In this research, the flow-rate is obtained by equating the sum of the pressure differences which drive the flow (wind and buoyancy) with that of those opposing it (hydraulic and friction losses). The result of this methodology is a dimensionless polynomial equation. For the situations of pure free convection, the polynomial can be expressed as:

$$B\left(H^+\right)^3 - \frac{1}{2}\left[\left(f_{app} Re_{Dh}\right) H^+ + \sum K_h\right] = 0 \tag{23}$$

The apparent friction factor has a different mathematical expression depending on the air flow regime. In laminar regime, its mathematical expression is obtained from [27]:

$$f_{app} Re_{Dh} = 96 + \frac{0.674}{H^+} \tag{24}$$

In turbulent regime, the apparent friction coefficient can be obtained from the mathematical expression obtained by Blasius [28]:

$$f_t Re_{Dh} = 0.184 \left(\frac{H}{2bH^+}\right)^{0.8} \tag{25}$$

Once all the terms are determined and substituted within the equation 23 a Newton Raphson method is used to solve it, and the mass flow rate is determined as:

$$\dot{m} = \frac{H \rho \nu W}{4bH^+} \tag{26}$$

2.5. Convection heat transfer with the surroundings

The evaluation of the average convective heat transfer coefficient of the PV module with the outdoor environment $\left(\overline{h}_{ca}\right)$ depends on the wind velocity, the wind direction and the buoyancy effect produced by the gradient between the temperature of the glass of the PV module and the ambient temperature.

A review of current literature on this topic starts with the research carried out by Mc Adams [29], who performed some experimental studies of the air flowing around boxes in a wind tunnel and found that the convective heat transfer coefficient had a linear dependency with the wind velocity. Watmuf [30] improved this correlations with the introduction of the buoyancy and the radiation effects. In parallel to these studies, Azevedo [31], also performed and extensive analysis of the air flowing around naphthalene boxes in a wind tunnel and obtained complementary non-linear correlations of the variation of the convective heat transfer coefficient with the wind velocity and the wind attack angle. In 1984, Sharples [32]performed real scale measurements over the exterior surfaces of high-rise buildings and found that the linear regressions fit well for large surfaces. More recently, the same author, [33] , carried an outdoor measurement campaign of the convective heat transfer coefficient in solar panels and he concluded that both the correlations of Azevedo[31], and Watmuf [30]are both valid for these solar components. Based on these previous studies, a linear correlation is implemented in the dynamic model. It has the following general expression:

$$\overline{h}_{ca} = a + c\mathbf{V}_{wind} \tag{27}$$

The value of the buoyancy coefficient, a, and the wind coefficient, c, depend on the angle of attack. Sharples [33] , determined two mathematical correlations:

$$\overline{h}_{ca} = 3.72 + 1.16 \cdot \mathbf{V}_{wind,surface} \text{ if } \theta_{wind} < 90^{\circ} \ (\mathrm{W/m^{2}{}^{\circ}C}) \tag{28}$$

$$\overline{h}_{ca} = 1.8 + 1.92 \cdot \mathbf{V}_{wind,surface} \text{ if } \theta_{wind} > 90^{\circ} \ (\mathrm{W/m^{2}{}^{\circ}C}) \tag{29}$$

The wind velocity at the PV module surface,$\mathbf{V}_{wind,surface}$, is obtained in function of the nearest weather station. To include some local terrain effects, the following empirical equation is used:

$$\mathbf{V}_{wind,surface} = \frac{1}{H} \frac{\mathbf{V}_{wind}\omega}{10^{z}\omega_{m}\left(\frac{y_m}{10}\right)^{z_m}} \left(\frac{(y_i + H)^{z+1}}{z+1} - \frac{y_i^{z+1}}{z+1} \right) \tag{30}$$

Where z and ω are terrain constants which vary between 0.47 to 1.0 and 0.15 to 0.35 respectively.

2.6. Solar radiation

The semitransparent PV module is modeled as a an equivalent opaque surface (A_{PV}), formed by the sum of the PV cells surface and an equivalent semitransparent surface (A_{PV}), formed by the sum of the spaces among the PV cells. Each equivalent surface has different optical properties and the packing factor defined in equation 9 will become the connection between these surfaces.

The equivalent opaque surface is modeled as a composite formed by an external glass layer and by a the layer formed by the EVA and the PV cells. The product tau-alpha ($\tau\alpha$) of this composite, based on the superposition of the single ($\tau\alpha$) of each layer, is the optical property to be determined. The PV manufacturers usually provide graphical drawings of the variation of the absorptivity of the PV cells with the solar radiation wavelength. In order to obtain the hemispherical value of $\tau\alpha$ of the composite, the software OPTICS [34, 35] has been used. The angular dependence of composites with PV cells as bottom layers has been deeply analyzed by Parretta [36, 37]. He concluded that the equivalent reflection has two components: a specular reflection produced at the air/glass interface and a diffuse reflection produced at the other interfaces. Both components have an opposite angular dependence: while the specular radiance increases with the incidence angle, the diffuse radiation decreases. Thus, in the case of vertical ventilated PV components (incidence angles between 40-60°), the specular reflection will be dominant. This conclusion leads to the definition of an equivalent refractive index, higher than the glass refractive index, able to include both terms. This refractive index varies from 2.5 for smooth glasses with anti reflective coating (ARC) to 3 for textured glasses without ARC. Since the reflection at the interface EVA/PV cell is diffuse, the PV absorptance will be independent of the incidence angle

and the angular dependence will only affect the transmittance of the glass and EVA combination. To determine this angular dependence, the incidence angle modifier (IAM), for each component of the solar radiation, will be used [38]:

$$IAM_{PV} = \frac{(\tau\alpha)_{PV,\theta}}{(\tau\alpha)_{PV,n}} = \frac{G_b \frac{(\tau\alpha)_{PV,b}}{(\tau\alpha)_{PV,n}} + G_{d,h} \frac{(1+cos\beta)}{2} \frac{(\tau\alpha)_{PV,d}}{(\tau\alpha)_{PV,n}} + G_h \frac{(1-cos\beta)}{2} \frac{(\tau\alpha)_{PV,g}}{(\tau\alpha)_{PV,n}}}{G} \tag{31}$$

In the equation 31 the terms related to the $(\tau\alpha)$ are treated separately for the direct and for the diffuse and reflected solar radiation:

- In the case of the direct radiation, two methodologies have been implemented:
  - Using Fresnel equations of the air/glass interface [39] with the equivalent refractive index obtained by Parretta [36, 37]
  - Using some mathematical expressions of the variation of the tau-alpha with the incident angle, obtained by Barker and Norton [40].
- In the case of the diffuse and reflected solar radiation components, the equivalent incident angles of Brandemuehl and Beckman [38] has been used as the inputs for the previous defined two methodologies.

Concerning to the equivalent semitransparent surface of the PV module, an overall hemispherical value has been obtained from the spectral dependency of each layer (glass, EVA and Tedlar). Ray tracing techniques implemented within the OPTICS software [34, 35] has been used. To determine the angular dependence of the optical properties, the same methodology than the equivalent opaque surface of the PV module will be followed.

The optical properties, including its angular dependency, of the rear facing material are obtained from the database of TRNSYS software .

The angular dependence of the optical properties of the materials must also include the reflections between the semitransparent surface of the PV laminate and the rear facing material, in case it is transparent. To determine these reflections, the net radiation method [41, 39] has been implemented. This method defines a positive component (G^+) and a negative component (G^-) of the incident solar radiation over each surface. The positive component for each layer is the fraction transmitted of the incident solar radiation plus the fraction reflected from the negative component of the opposite layer. The incident value of the first layer is set as the unity and the value of the flux coming from the room which is in contact with the ventilated PV component is set to 0, hence a system of equations for each layer is defined. Once the equations are solved, the total reflectivity and solar transmittance of the overall ventilated PV component is found as:

$$\rho_{\text{façade}} = G^-_{tr} = \rho^f_{tr} + \frac{\tau^2_{tr}\rho^f_g}{1-\rho^f_g\rho^b_{tr}} \tag{32}$$

$$\tau_{\text{façade}} = G^+_{room} = \frac{\tau_{tr}\tau_g}{1-\rho^f_g\rho^b_{tr}} \tag{33}$$

The absorptivity of each layer of the equivalent semitransparent surface of the PV module, and of the rear facing material be also determined as:

$$\alpha_{tr,\text{façade}} = (\alpha_{gPV} + \alpha_{EVA} + \alpha_{tedlar}) \left(1 + \frac{\tau_{tr}\rho^f_g}{1-\rho^f_g\rho^b_{tr}}\right) \tag{34}$$

$$\alpha_{g,\text{façade}} = \alpha_{g1} \left(\frac{\tau_{tr}}{1-\rho^f_g\rho^b_{tr}}\right) \tag{35}$$

Once the optical properties are obtained, the absorbed solar radiation of the front glass layer (S_{g1}), of the PV cells layer (S_{g2}), of the Tedlar layer (S_{g3}) and of the rear facing material (S_{g4}), can be determined with the following equations:

$$S_{g1} = P\alpha_{gtr,n} IAM_{tr} G_t + (\alpha_{gtr,\text{façade},n} IAM_{tr} G_t)(1-P) \tag{36}$$

$$S_{g2} = P(\tau\alpha)_{PV,n} IAM_{PV} G_t + (\alpha_{EVA,\text{façade},n} IAM_{tr} G_t)(1-P) \tag{37}$$

$$S_{g3} = (\alpha_{tedlar,\text{façade},n} IAM_{tr} G_t)(1-P) \tag{38}$$

$$S_{g4} = (\alpha_{g1,\text{façade},n} IAM_{tr} G_t)(1-P) \tag{39}$$

2.7. Thermal radiation

The thermal radiation, between the semitransparent surface and the rear facing material is determined by solving the net heat transfer between two infinite gray parallel plates:

$$q"_{rg1e} = -q"_{reg1} = h_{rg1e}(T_{g1} - T_e) \tag{40}$$

The thermal radiation between the glass of the PV laminate and the sky follows the same expression than the equation 40, but with the corresponding linearized radiation heat transfer coefficient (h_{rsc}) and the temperatures of the glass (T_c) and of the sky(T_s). The sky temperature is obtained from the Bliss correlation [38]. The thermal radiation between the back side of the rear facing material and the room in contact follows the same expression than the equation 40, but with the corresponding linearized radiation heat transfer coefficient (h_{rg2i}) and the temperatures of the last node (T_{g2}) and of the average walls temperature temperature (T_{ri}). This last temperature is obtained through the star scheme developed within TRNSYS [21].

2.8. Electricity generated by the PV

The electricity generated by the PV cells must be expressed as:

$$q_e" = (\tau\alpha)_{PV,n} IAM_{PV} G_t P\eta_{PV} \tag{41}$$

The PV efficiency is depending on the PV cells temperature and on the incident radiation. To consider these two factors, a linear variation model has been adopted [42].

2.9. Overall energy balances

The figure 2.9 shows the overall energy balances which will be obtained with the dynamical model.

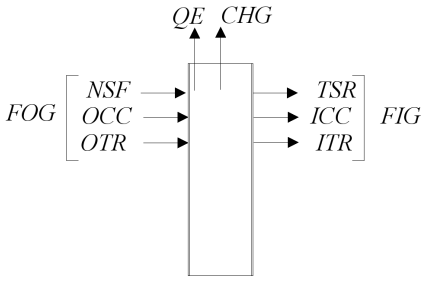

Figure 3: Overall energy balances.

The overall balances are divided in four categories: energy gains/losses from the outside (*FOG*), energy gains/losses from the inside (*FIG*), enthalpy gains within the ventilated air gap (*CHG*)

and electricity produced by the PV (QE). A global energy balance of the whole component is achieved as:

$$FOG = FIG + CHG + QE \quad (W/m^2) \tag{42}$$

The energy gains/losses from the outside are divided in:

$$FOG = NSF + OCC + OTR \quad (W/m^2) \tag{43}$$

Where:

$$\begin{aligned}
NSF = &\quad \text{Absorbed solar radiation in the façade} \\
&= S_{g1} + S_{g2} + S_{g3} + S_{g4} \quad (W/m^2) \\
OCC = &\quad \text{Convective heat transfer with the outside} \quad = h_{ca}\,(T_a - T_c) \quad (W/m^2) \\
OTR = &\quad \text{radiative heat transfer with outside} \quad = h_{rsc}\,(T_s - T_c) \quad (W/m^2)
\end{aligned}$$

The enthalpy gains within the ventilated air gap are defined as:

$$CHG = mc_p\,(T_{f,o} - T_{f,i}\dot{)} = q_{ef}" + q_{g1f}" \quad (W/m^2) \tag{44}$$

The energy gains/losses from the outside are divided in:

$$FIG = TSR + ICC + ITR \quad (W/m^2) \tag{45}$$

Where:

$$\begin{aligned}
TSR = &\quad \text{Transmitted solar radiation} \quad = \tau_{\text{façade}} G_t\,(1 - P) \quad (W/m^2) \\
ICC = &\quad \text{Convective heat transfer with the inside} \quad = h_{ig2}\,(T_i - T_{g2}) \quad (W/m^2) \\
ITR = &\quad \text{Radiative heat transfer with the outside} \quad = h_{rig2}\,(T_{ri} - T_{g2}) \quad (W/m^2)
\end{aligned}$$

3. Calibration of the dynamic model

The calibration of the forward dynamic model is a crucial process to determine the accuracy of the model. It is also a requirement to fix the range of variation of the best estimates for the unknown parameters and to identify which are those parameters with have more influence in the results. Besides, in this research, the calibration plays a crucial role because it will be the mechanism to select the combination of correlations and coefficients, among the wide variety which is implemented, which better fit the experimental results. As previous authors highlighted, [43, 44], due to the large number of unknown input parameters in the detailed dynamic model developed, the calibration will be characterized by a non-unique solution. In stead of looking for a single and optimal solution for the estimates of the unknown parameters, a set of solutions as the best possible combination, will be searched. The multi stage calibration methodology described in [20] will be used for this purpose. This multi stage calibration methodology defines an iterative optimization procedure which starts with the assignment of probabilistic density functions (PDF) to the unknown parameters, followed by a random sampling and running batch of simulations. It then finishes with an iterative uncertainty and sensitivity analysis combined with a re-assignment of the ranges of variation of the strong parameters. The procedure converges when no new influencing parameters are found. In this case, the following hypothesis for the calibration will be assumed:

1. The average air temperature at the outlet of the air gap ($T_{f,o}$) will be used to calibrate the model with the monitored measurements because it is the air temperature which has been measured and because it directly affects the air mass flow rate and the wall temperatures calculation.

2. The goodness of fit criteria will be determined as a combination of the Normalized Mean Bias Error (NMBE) and the Coefficient of Variation of the Root Mean Square Error (CVRMSE), as stated by [20, 43].
3. Following the requirements defined by [20, 43], the trials over which the sensitivity analysis will be performed, will be the ones with a goodness of fit (GOF) criteria smaller than 10 %.
4. The minimum size of the sampling will be of 16 times bigger than the number of parameters, as stated in [20].

3.1. Measurements of the energy performance of a natural ventilated PV component in outdoor conditions

The experimental results of an extensive monitoring campaign on a ventilated double skin with integrated photovoltaic system are detailed in [45]. The measurements have been carried out at the facilities of the Outdoor Test Reference Environment of Lleida (TRE-L), in Spain (local latitude of 41.6°N) . In Fig. 4 the measurement set-up of the TRE-L is schematically shown.

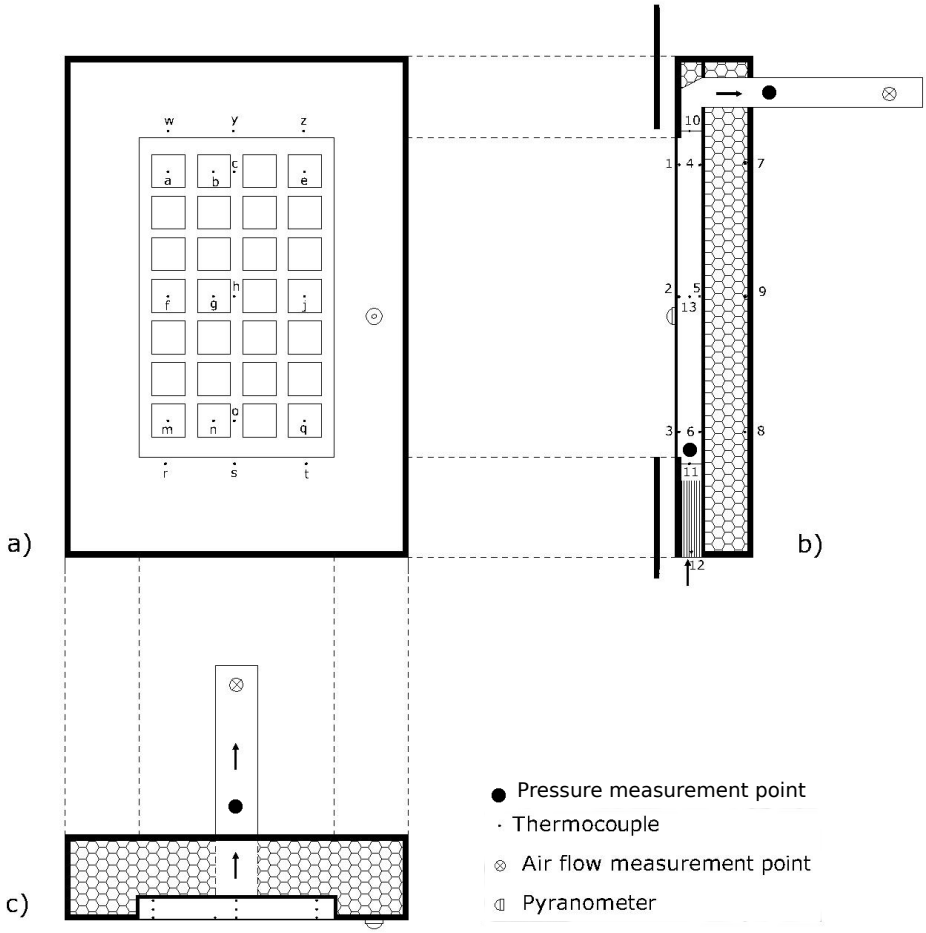

Figure 4: TRE-L measurement set-up: positioning of the sensors. (a) Front view; (b) cross view; (c) top view

The TRE-L is composed by a wooden box (206 x 236 x 37 cm and thickness of 2.2 cm) and a support structure which allows any inclination to be tested. To achieve adiabatic conditions at the back side of the PV system, the TRE-L is filled in with an insulation layer of 20 cm thick of expanded polystyrene (EPS) ($k = 0.031^{\mathrm{W}}/_{\mathrm{m}^{\circ}\mathrm{K}}$). The TRE-L has a south-oriented opening where a semi transparent glass-Tedlar PV module (with dimensions of 97.6 x 150.7 cm) was positioned. The tested PV module is formed by 28 mono crystalline silicon (m-Si) solar cells ($P = 0.46$). An air channel with the same height as the PV panel and 11.5 cm width, (aspect ratio of 13.6) is constructed at the backside of the PV module and allow the air to flow upwards. The air enters from the bottom and goes out through a PV tube (12.5 cm diameter), which is placed at the top back side of the TRE-L.

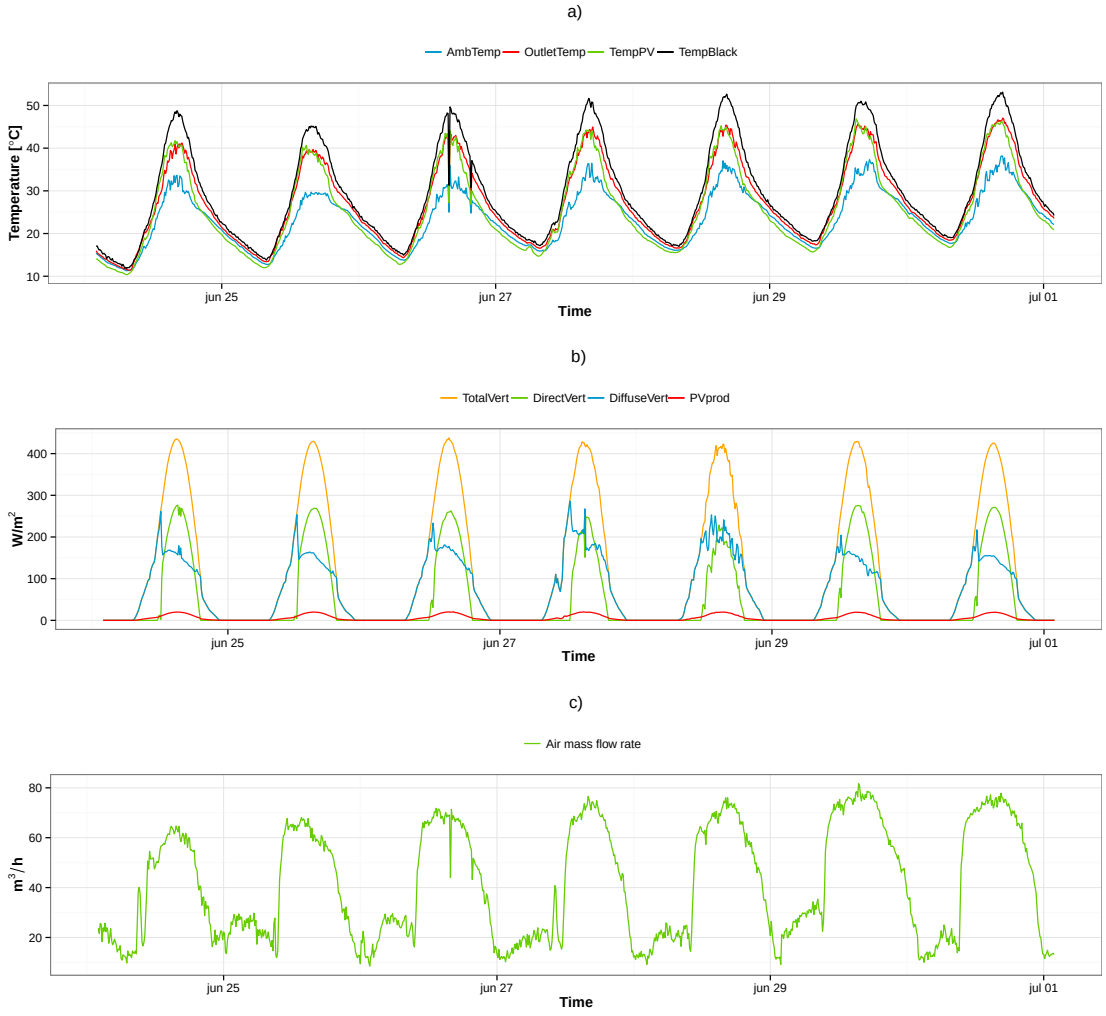

Figure 5: Measured data: a) temperatures: ambient, outlet, PV module, rear facing material; b) Solar radiation and electricity production; c) air mass flow rate

The temperature of the back side of the PV module, of the rear facing material and of the air gap, are measured with type J thermocouples (accuracy of ± 0.5 °C). The air flow is measured through an indirect method based on measuring the readings of a differential pressure manometer (see Fig. 4). The air mass flow rate is obtained using the power law relationship between the pressure difference and the volumetric air flow rate (accuracy of ± 10 %).

The incident solar radiation is measured with a pyranometer installed in the south face of the

TRE-L. A weather station measures the ambient temperature, wind velocity, wind direction and the relative humidity.

During the experiments the rear facing material has the ALANOD-Mirotherm, with a solar absorption of 95 $\pm$ 1 % (in the range of wavelength between 380 and 1650 nm) and a thermal emission of 5 $\pm$ 2 % (in the range of wavelength between 3 and 20 $\mu\, m$).

From 16$^{\text{th}}$ June 2013 to 10$^{\text{th}}$ March 2014, a monitoring campaign was carried at the installations of LOTCE in Lleida, Spain (local latitude of 41.6°N). Two different inclinations were tested (optimized inclination and vertical inclination). The Fig 5 shows the temperatures, the solar radiation and the electricity produced by the PV module, measured at the TRE-L, during the monitoring campaign with vertical inclination. The first 60 hours of this time series data will be used for the calibration of the dynamic model.

3.2. Assignment of best estimates to the unknown parameters

The dynamic model has 69 parameters. Some of them have been excluded from the calibration process, such as those related to the geometry, because there is a very few uncertainty in their definition.

Since wind velocity was very small in the monitoring period, [45], the external convection coefficient is assumed as constant and the related parameters are excluded from the calibration too. Finally, 43 unknown parameters are selected to be included in the calibration methodology.

The best guess values of these parameters and their corresponding probability density functions (PDF) are shown in Table 2. Following the criteria defined by [44], normal distribution functions were applied to the physical characteristics of building materials and uniform distribution functions are assigned to the parameters related to the air mass flow rate and Nusselt number correlations.

3.3. Latin Hypercube Monte Carlo sampling and dynamic simulations

After assigning the probabilistic density functions to each range of variation of the parameters, a random sampling Latin Hypercube Monte Carlo (LHMC) is used to identify potential regions of local optima[46]. Following the criteria defined in [20], a sampling size of 700 trials has been selected. The software package used to generate the LHMC sampling is R statistical package (http://www.r-project.org/).

Number	PDF	Description	Coefficient of Variation (CV) ($St.dev/mean$)
1 to 4	Normal	Physical properties of the glass of the PV module (density, specific heat, conductivity and thickness)	0.06 to 0.25
5 to 7	Normal	Physical properties of the PV cells (density, specific heat, conductivity)	0.06 to 0.17
8	Normal	Solar absorptivity of the PV cells at normal angle	0.04
9-12	Normal	Physical properties of the EVA (density, specific heat, conductivity and thickness)	0.05 to 0.24
13-16	Normal	Physical properties of the Tedlar (density, specific heat, conductivity and thickness)	0.07 to 0.25
17-18	Normal	Thermal emissivity of the front and back of the PV module	0.05 to 0.06
19 to 24	Normal	Transmittances of the transparent layers of the PV module	0.05 to 0.1
25 to 30	Normal	Physical properties of the ALANOD-Mirotherm (density, specific heat, conductivity, thickness,thermal emissivity)	0.06 to 0.17
31	Normal	Solar absorptivity of the ALANOD-Mirotherm	0.03
32	Uniform	discharge coefficient of equation 22	0.38
33	Uniform	coefficient $\overline{H_l}$ of correlation of Rohsenow [23], from Table 1	0.37
34-37	Uniform	Coefficients and exponents of equation 21	0.21 to 0.41
38-43	Uniform	coefficients and exponents of correlation of Rohsenow [23], from Table 1	0.23 to 0.52

Table 2: Best estimates and range of variation of the selected unknown parameters

The LHMC trials will constitute the input parameters of the dynamic model created with TRNSYS [21]. Several batch simulations are carried out using jEPlus software [47], which allows a systematic running of parallel simulations and efficient collection of the outputs generated.

3.4. Uncertainty analysis

A GOF below 10 % will be assumed for trials acceptance. Once the LHMC batch run is completed, the GOF index is computed for each trial. From here we can weed out those parameters vectors which result in GOF$<$ 10 %. The information contained in these "best" or feasible parameters vectors are then used to identify the strong parameters through a sensitivity analysis.

3.5. Iterative process of sensitivity analysis and re-assigment of ranges of variation to the strong parameters

Following the methodology defined [20], the Pearson chi square $\left(\chi^2\right)$ test [48] is used to compare the parameter vectors distributions. The trials of parameters which fits the GOF criteria are compared with the overall sample population. The histograms of frequencies of both populations have been generated with the same number of bins (8 bins). The null hypothesis is rejected when the p-value is smaller than 1 %.

Once the strong parameters are identified, new ranges of variation of their PDF are assigned and a new iteration of the LHMC sampling generation and batch running of simulations starts. The process converges when no strong parameters are detected. In this case, for the set of 700 trials, 24 iterative steps were necessary to achieve the converge.

4. Results

4.1. Evaluation of the strong parameters

In Fig. 6, the variational ranges obtained for each strong parameter after each iteration, once they are re-assigned, are shown. As can be seen in Fig. 6, all the detected strong parameters narrow their range of variation, meaning that they can all be assumed as influencing parameters. Furthermore, it can be seen that the strong parameter are those related to the transmittances of the transparent surfaces of the PV laminate (parameters 20, 22, 24), the absorptivities of the the PV cells and the rear facing material (parameters 19, 31), the discharge coefficient of the air mass flow rate correlation (parameter 32) of equation 22), the exponents of correlation for $\overline{Nu}$ of Churchill [25] of Table 1 (parameters 36, 37) and some of the coefficients and exponents of the correlation for $\overline{Nu}$ of Rohsenow [23] of Table 1 (parameters 33, 40, 41, 42, 43). Besides, it can be seen that there are two clear strong parameters: the equivalent transmittance of the semi transparent surfaces of the PV module, parameter 24, and the discharge coefficient of the air mass flow rate, parameter 32.

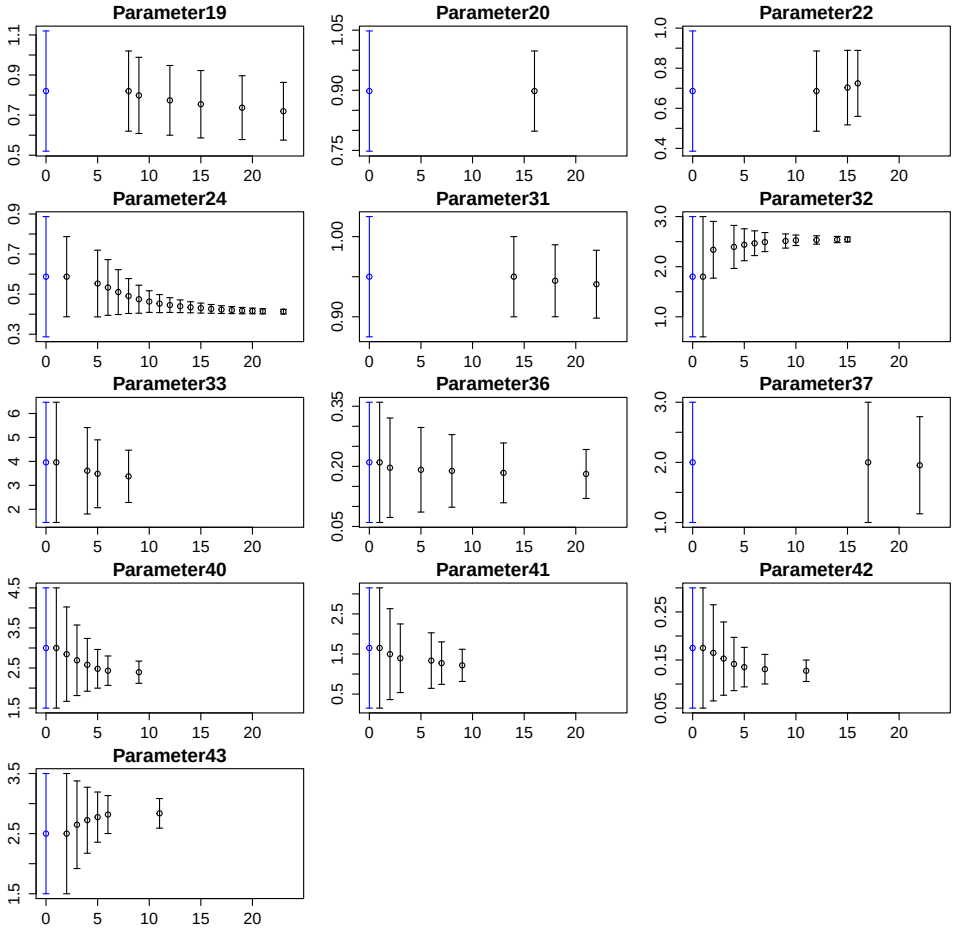

Figure 6: Ranges of variation of the strong parameters in each iteration

From the analysis of the strong parameters, some conclusions regarding the heat and mass transfer within the ventilated air gap, can be obtained:

1. The more precise correlation to be used for determining the air mass flow rate is the correlation of Bansal et. [26](see equation 22), with a discharge coefficient with the following

range of variation: $C_d = 0.41 \pm 0.02$. This result is in coherence with the conclusions obtained by [49, 50], for similar studies with solar chimney devices.

2. The air flowing within the air gap varies from laminar to turbulent regime, however, since the detected strong parameters belong to the correlations of Churchill [25] and Rohsenow [23] , it can be concluded that the periods with transition from laminar to turbulent are more frequent and predominant (see section 2.4) than the other ones. This conclusion is in coherence with the experimental results obtained in [45]. The correlations for this situation can adjust their coefficients and exponents with the identified ranges of variations of the corresponding strong parameters. In Table 3, the correlations with the new coefficients and exponents are shown. The parameters which are not so strong, (weak) remain with the nominal values suggested by the authors :

Authors	Proposed correlation	*Parameter ranges*
	Transition to turbulent regime	
[23]	$\overline{Nu}_b = \left[\left(\overline{Nu}_{plate}\right)^{-p_{40}} + \left(\overline{Nu}_{fd}\right)^{-p_{40}}\right]^{-1/p_{43}}$	
	$\overline{Nu}_{fd} = p_{38} \cdot (Ra_b")^{p_{39}}$	$p_{33} = 3.30 \pm 0.85$
	$\overline{Nu}_{plate} = p_{41} \cdot p_{33} \cdot (Ra_b")^{p_{42}}$	$p_{38} = 0.29$ *(weak)*
		$p_{39} = 0.5$ *(weak)*
		$p_{40} = 2.37 \pm 0.22$
		$p_{41} = 1.19 \pm 0.4$
		$p_{42} = 0.12 \pm 0.02$
		$p_{43} = 2.85 \pm 0.19$
[25]	$\overline{Nu}_H = \left(p_{34} + p_{35} \cdot Ra_H^{p_{36}}\right)^{p_{37}}$	
		$p_{34} = 0.82$ *(weak)*
		$p_{35} = 0.32$ *(weak)*
		$p_{36} = 0.17 \pm 0.05$
		$p_{37} = 1.89 \pm 0.64$

Table 3: New coefficients for the correlations of $\overline{Nu}$ in transition to turbulence regime

4.2. Evaluation of the goodness of fit

The evolution of the GOF and NMBE with the number of iterations is shown in Fig. 7. In this figure, it can clearly be seen that the influence of number of iterations is determinant to achieve low values of both NMBE and GOF. The interquartile range (IQR) of the GOF varies from 11.4 % for the first iteration, to 0.29 % for the last iteration. In the case of the NMBE, the IQR varies from 9.24 % for the first iteration, to 0.54 % for the last iteration. These ranges of GOF and NMBE are clearly within the limits to achieve the criteria of GOF < 10 %, defined as requirement in this research. They are also within the limits defined by [43, 20] and within the limits defined in the ASHRAE guidelines [51]. That means, the dynamic model can be assumed as calibrated for the set of trials defined in the last iteration (iteration 24).

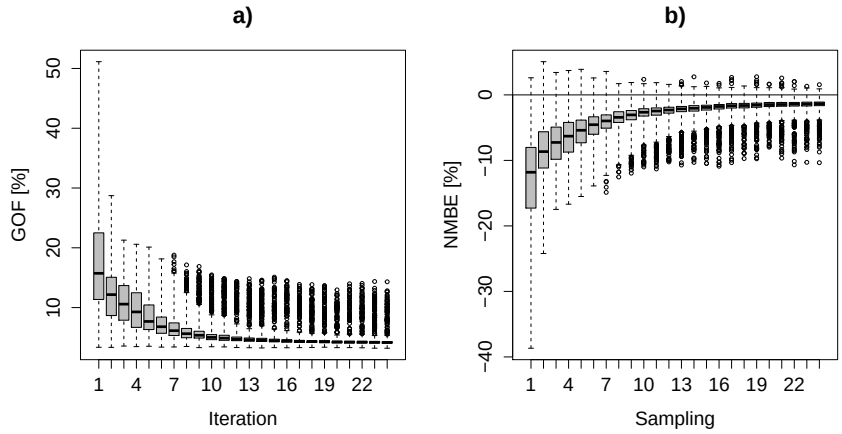

Figure 7: a) box plots of the variation of the GOF with the number of iterations; b) boxplots of the variation of the NMBE with the number of iterations

4.3. Comparison between measured and simulated time series data

In Fig.8 hourly time series plots of the predicted and measured air temperature at the outlet of the air gap, are shown for some of the iterations. The red line corresponds to the measured data in the monitoring period, the blue line corresponds to the mean of the set of trials of each iteration and the gray shaded area corresponds to the 95^{th} probabilistic threshold range of solutions.

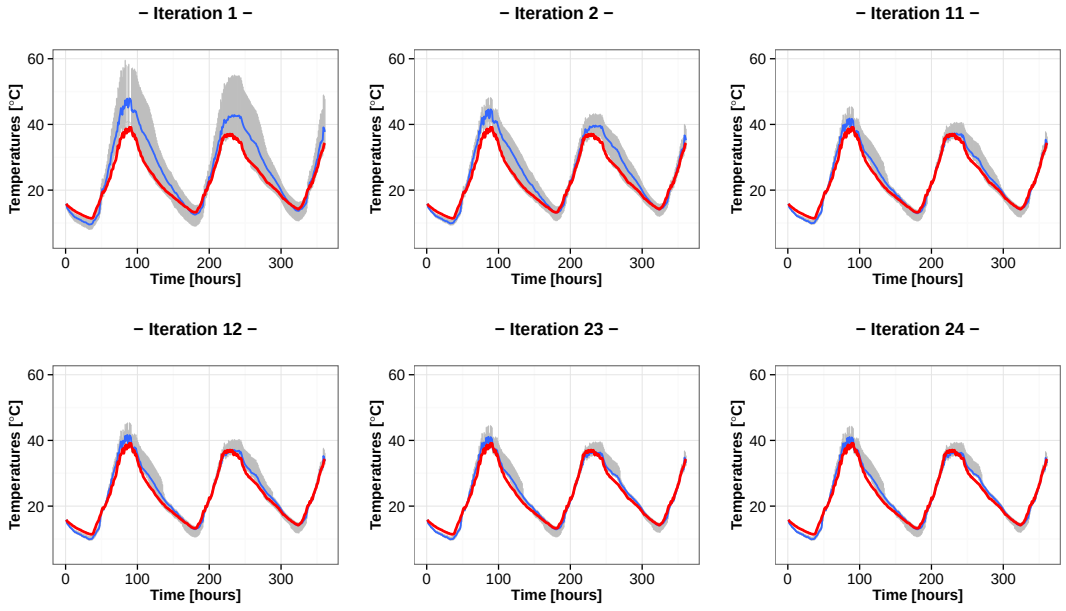

Figure 8: Hourly time series plots of the indoor temperature for first, middle and latest iterations

In Fig.8 in can be seen that the difference between monitored and predicted results is much higher in the first iteration (non-calibrated solution) than in higher iterations. It can also be seen that from iteration 12 the main differences are related to the dispersion of the solutions of the trials, being greater at this iteration than at the latest one. However, the mean values of the trial solutions (blue line) remain very similar from this iteration to the latest one. This evolution is in coherence with the evolution of the GOF and NMBE of Fig. 7.

Residual analysis

To determine more accurately the precision of the dynamic model as well as its capacity to capture the dynamics of the model, residual analysis will be carried out. The following tests will be performed: to check that the residuals are normally distributed with zero mean, that their variances do not vary with the effects being modeled, and that the residuals are uncorrelated. These tests will be based on analysis of the plots of the residuals. The tests will be applied over all the iterations although only some of them will be drawn and the differences among them will evaluated. Assuming that for each iteration and time step there will be a number of residuals equivalent to the number of trials of the sampling (700 trials), the mean of this residual vector will be calculated for every time step and the tests will be applied over this mean value of each iteration. In Fig.9 the mean of residuals of each iteration is plotted versus time. As it can be observed, the residuals decrease for higher iterations although the bigger reductions occur from the first iteration to the iteration 12. It can also be seen that in the last iteration there are still some peaks in the curves which reach error values of +3.45 °C and -2.9 °C and that some of these peaks are repeated in several time lags. This performance indicates a high probability of autocorrelation of the residuals.

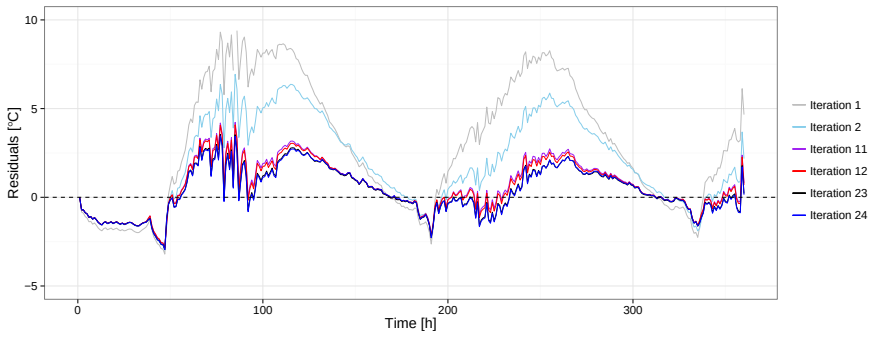

Figure 9: Plot of the mean of residuals versus time for first, middle and latest iterations

In Fig. 10, histograms of the means of residuals of some of the iterations, as well as qq-plots of them, are shown. The red line of the upper figures represent the density function of the theoretical normal distribution. As can be seen, in the latest iterations the residuals mean is very close to zero, meaning that the means of residuals are well balanced over time.

Looking at the qq-plot graphs of the latest iterations, it can be seen that the improvement is very important compared to the initial iterations and their distribution is not strictly normal but very close to it.

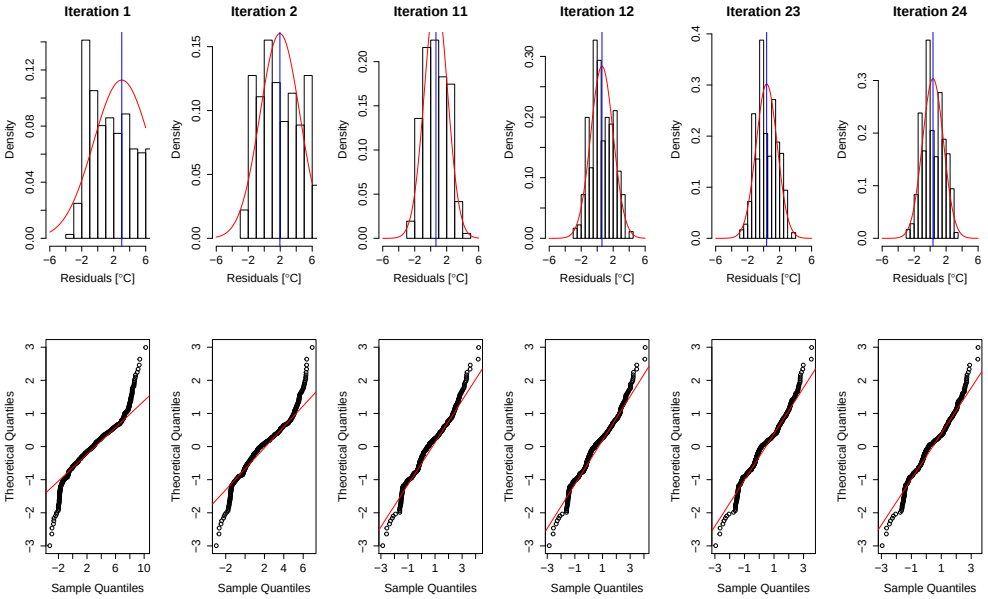

Figure 10: Histograms and q-q plots of means of residuals for first, middle and latest iterations

In Fig. 11, the correlation plot between means of residuals and the predicted air temperature at the outlet of the air gap is shown for each iteration.

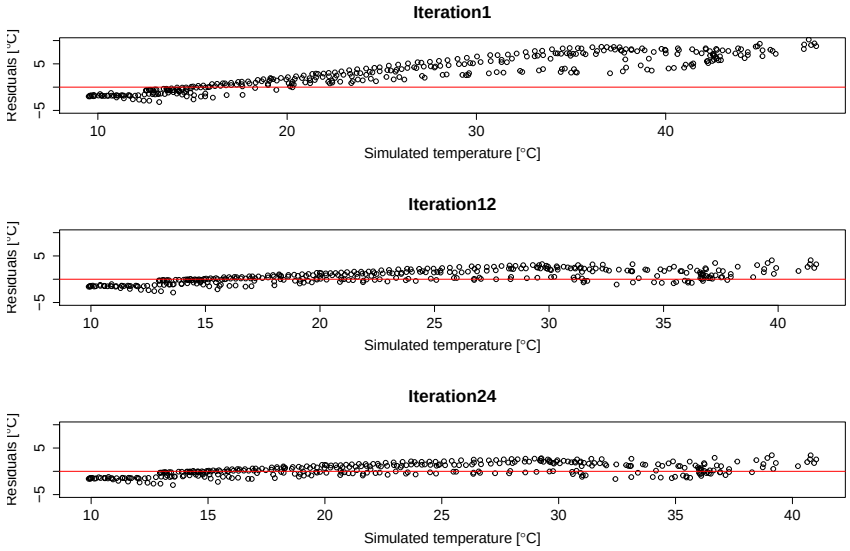

Figure 11: Plots of the means of residuals, for the first, middle and last iterations, versus predicted air temperature at the outlet of the air gap

In Fig. 11, it can be seen that the variability of residuals improves compared to the the initial situation (Iteration 1), however the pattern of data points shows small negative concentrations

of residuals in between 10-25 °C and small positive tendency from 15-30 °C, meaning that the error variance is a little correlated with the independent variable (regression error). In such a way, variance is said to be conditional (not constant) and its value depends on error itself. That means the residuals variance follow a conditional heteroskedasticity.

The last test to verify that the model is able to describe the dynamics of the system properly, consists in analyzing if the residuals are autocorrelated. This will be done with the auto-correlation (ACF) and partial autocorrelation functions plotted in Fig.12. Confidence bands of approximately 95% under the hypothesis that the residuals are white noise are also shown in blue. The ACF of the mean of residuals clearly shows that the residuals are non-stationary and have seasonal dependence. From the PACF graph, in iteration 24 it can be seen that there are three main spikes at time lags 1,5 and 145, meaning that the there is a degree of 3 in the autocorrelation. It must be highlighted that the input data of the model (ambient temperature and Solar radiation) also follow a periodic pattern, therefore, the periodicity of the residuals means that the model is not able to decouple the residuals from the inputs. This means the residuals are not independent and the white noise assumption for the residuals should be rejected.

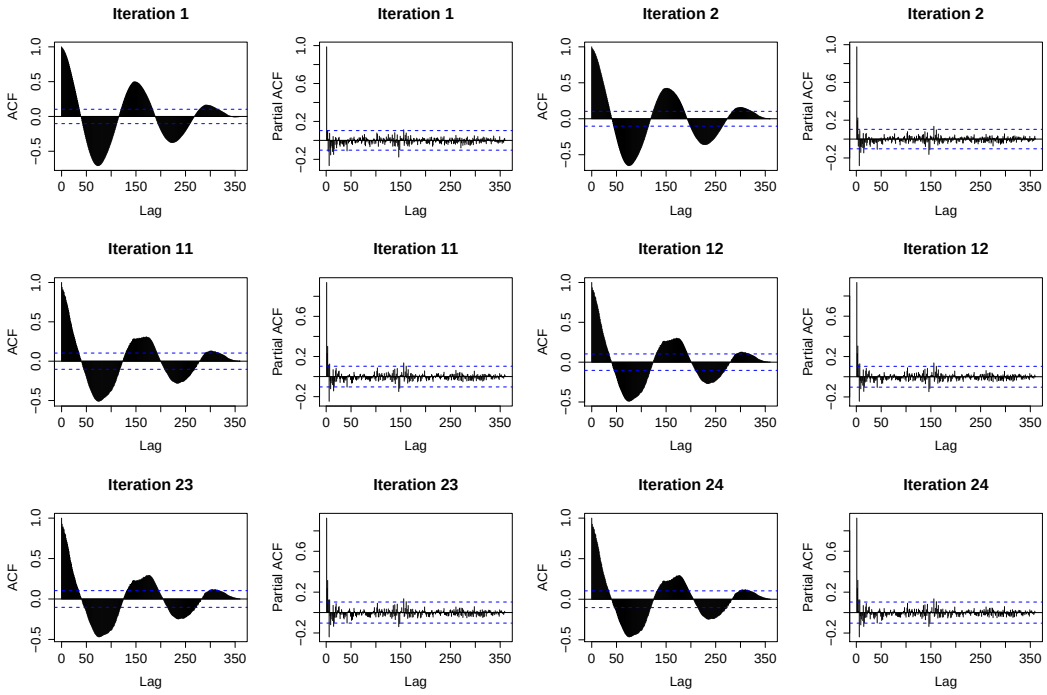

Figure 12: ACF and PACF of the mean of residuals for initial, middle and latest iterations

The tests performed in the previous figures clearly state that the dynamic model is not able to capture the dynamics of the ventilated PV component with enough statistical significance. This is in coherence with the requirements underlying the calibration methodology, which are more centered in determining the influencing parameters and achieving a GOF criteria rather than on capturing the real dynamics of the building.

To analyze potential outliers or systematic dependencies of the residuals on inputs, states or number of iterations, correlation plots are drawn. The Fig. 13 shows the scatter plots among means of residuals, iteration number incident global solar radiation (GTotVert), ambient temperature (AmbTemp) and wind velocity (WindVel). It can be seen that from iteration 12, the

means of residuals are totally correlated between consecutive iterations, meaning that there is almost no variation in their distribution, as was reflected in the evolution of the GOF.

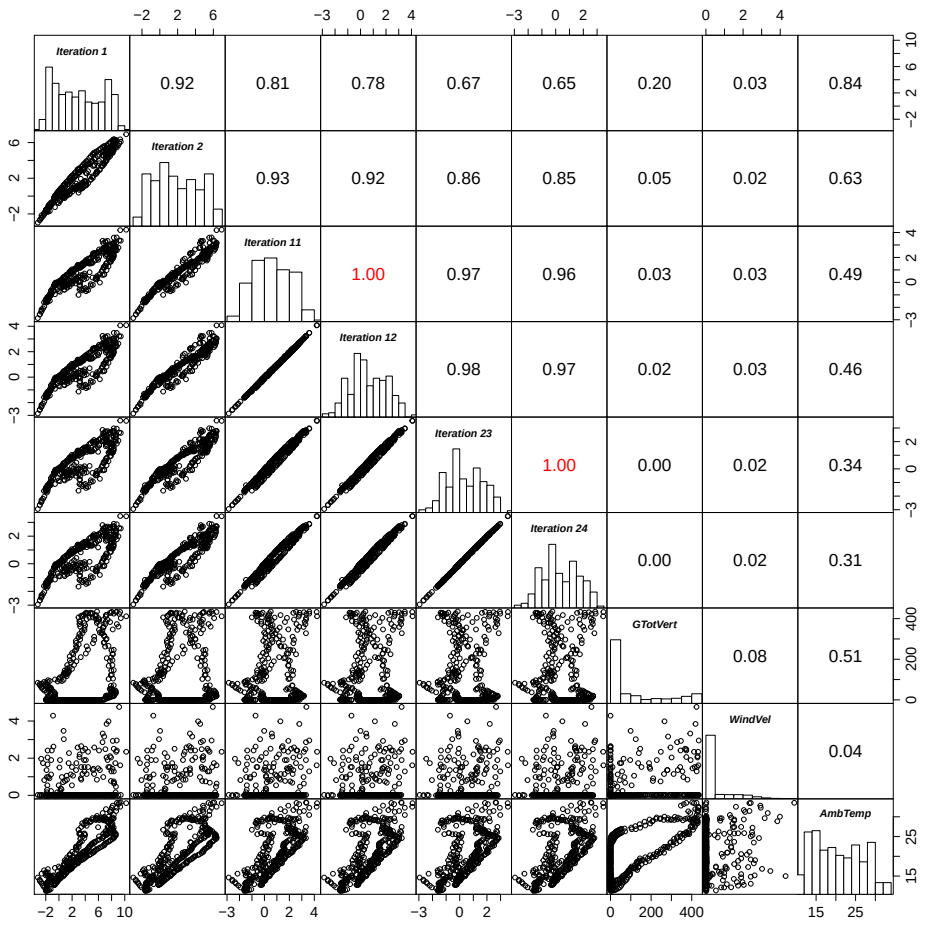

Figure 13: Correlation plots of the means of residuals among some of the iterations, Incident solar radiation ($GTotVert$), wind velocity ($WindVel$) and ambient temperature ($AmbTemp$)

In Fig.13, it can also be seen that there is a strong correlation between means of residuals and outdoor temperature, while there is no correlation with the wind velocity. It can also be observed that the correlation with the incident solar radiation decreases for higher iterations, however some level of heteroskedasticity is observed. This results, reveal what was previously stated that the simulated results are conditioned by some of the inputs, mainly by the ambient temperature and, with lower influence, by the solar radiation.

Evaluation of the overall energy balances

In Fig.14, a comparison of the predicted electricity production and the enthalpy gains within the air gap, versus the measured data, is shown. As in the case of Fig.8, the red line corresponds to the measured data in the monitoring period, the blue line corresponds to the mean of the set of trials of each iteration and the gray shaded area corresponds to the 95^{th} probabilistic threshold range of solutions.

In Fig.8 it can be seen that the electricity production is predicted with high precision and the differences with the monitored data are almost negligible. However, in the case of the enthalpy gains, the differences between the mean of solutions and the measured data are appreciable. It can also be seen the high dispersion of solutions in this last case. These differences can be acceptable if we consider the range of uncertainty in the measurements of the air flow rate ($\pm 10\%$) which is transmitted to the monitored enthalpy gains. The main reason for these deviations is probably due to the lack of precision in the modeling of the air mass flow rate.

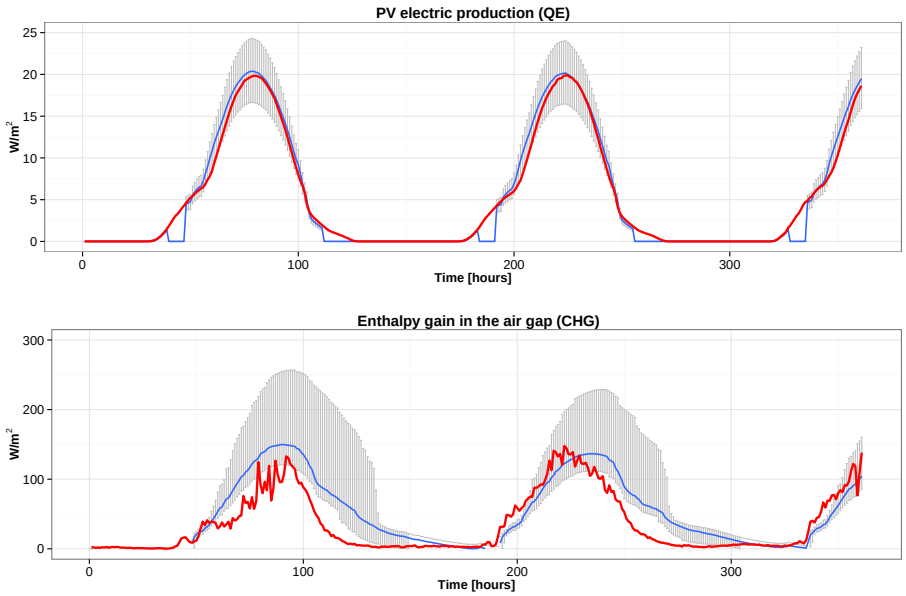

Figure 14: Comparison of predicted PV electrical production and enthalpy gain at the air gap with the monitored data

5. Conclusions

A strong thermodynamic coupling exists between the air flow through the naturally ventilated PV component, the air temperature difference between the cavity and the outside and the incident solar radiation. This interaction can only be predicted by sophisticated dynamic energy modeling and simulation techniques as has been done in the current study.

Three new TRNSYS types have been developed and validated through monitoring experiments. The very flexible programming environment of TRNSYS has allowed the implementation of numerical approximations of the heat conduction in the multilayer PV module, of several heat transfer correlations as well as the evaluation of the internal solar reflections. The unknown coefficients and parameters can be easily adjusted to the specific conditions with the corresponding calibration methodology.

In this research it has been demonstrated that the combination of dynamic modeling with calibration methodologies is of critical importance to achieve a precise simulation of the real energy performance of complex components. It is not enough to implement very sophisticated differential equations, empirical correlations and complex solvers if there is no confronting with the real energy performance. Besides, this calibration should be embedded in the overall simulation methodology in a semi-automatic way to allow for massive batch running and optimization . The open software environments used in this research, R and jEplus, [47], permit this automation by

coupling the fundamental empirical physical models with strong statistical tools and introduce the needed degree of randomness and stochasticity in the empirical models.

Some general conclusions must be stated regarding the multi stage calibration procedure implemented in this research. This kind of calibration techniques highly depends, in one side, from the initial estimated range of variation of the input parameters [43], and on the other side, on the accuracy of the monitored data, since the GOF evaluation is calculated based on them. These two main factors constrain the validity of the selected set of best trial solutions and of the identified strong parameters. This means that the results of the calibration should not be generalized but limited to the initial variational ranges, to the experimental data and to the characteristics of the PV ventilated component.

Regarding the results of the calibration, it should be mentioned that the predominant air flow regime is the transition state from laminar to turbulence and that the main strong parameters are related to the hydraulic losses coefficient and to the Nussel number correlation coefficients. The correlation of Bansal [26] obtains better results than the procedure of Brinkworth [7, 8, 10] for the modeling of the air flow rate. However, further refinements or other alternative expressions should be tested because the major differences in the residuals are related to the prediction of the air mass flow rate. The other strong parameters are related to the transparency properties of the PV module.

Another main conclusion is related to the electrical production of the PV module. The high precision in the prediction of the electricity produced by the PV module indicates a weak coupling between the electrical production and the heat transfer process that occurs in the ventilated air gap. This decopling could be justified because of the low density of PV cells, leading to the main conclusion that in the case of high transparent PV modules, the effect of the ventilated air gap over the electrical production is negligible should only be considered as a method to evacuate the incident solar radiation in the form or warmed air.

The implemented dynamic model, combined with the multi-stage guided search approach, has demonstrated a great precision in achieving minimum GOF criteria for a set of best trials, however it fails in capturing the dynamics of the PV component. The dynamic model is not able to fulfill the criteria of white noise for the residuals and presents some problems with autocorrelation of residuals. This lack of precision in capturing the dynamics, limits the application of this simulation model to long-term evaluations of the electrical and heat energy production and to parametric analyses such as the evaluation of changes in the materials of the PV, in the rear facing material or in the air gap dimensions. In case that the designers are interested in short term dynamic modeling, other methods based on stochastic inverse modeling such as those developed by [52] are preferable. Considering the level of auto regression of the ambient temperature, of the solar radiation and of the residuals, auto regressive forecasting methods such as the ARIMA models would also be a another alternative short term forecasting method.

Nomenclature

A	area $\left(m^2\right)$
b	depth of the air gap (m)
C_d	discharge coefficient (-)
c_p	specific heat capacity of the air $(J/kg^\circ C)$
D_h	hydraulic diameter (m)
g	gravitational acceleration (m/s^2)
G	incident solar radiation (W/m^2)
B	buoyancy term, (-), $B = {}^{2SGr_{Dh}}/_{Pr}$
$\overline{h}$	average convective heat transfer coefficient $(W/m^{2\circ}C)$,$\overline{h} = {}^{\overline{Nu}\cdot k}/_{D_h}$

h_r	linearized radiative heat transfer coefficient ($W/m^{2\circ}C$)
h_i	thickness of each solid layer (m)
H	height of the ventilated PV component (m)
H^+	dimensionless height, (-), $H^+ = H/2bRe$
k	thermal conductivity ($W/m^{\circ}C$)
k_h	inlet and outlet hydraulic losses (-)
$\dot{m}$	air mass flow rate (Kg/s)
$\overline{Nu}$	average Nusselt number (-)
Pr	Prandtl number (-)
q"	specific heat flux (W/m^2)
q_e"	specific electrical production of the PV laminate (W/m^2)
Q	volumetric heat source (W/m^3)
Ra"	modified Rayleigh number for uniform heat flux boundary conditions, (-), $Ra" = \rho^2 g\beta c_p q_w"/$
Re	Reynolds number (-)
S	coefficient of stratification (-)
S_g	solar radiation absorbed by the solid layers(W/m^2)
T	average temperature of the air gap at a fixed height (°C)
y	vertical distance (m)
W	width of the ventilated PV component (m)

Greek letters

α	solar absorptivity (-)
τ	solar transmittance (-)
ρ	density (Kg/m^3)
ν	kinematic viscosity $\left(m^2/s\right)$
η	unitary vector at normal direction (-)
η_{PV}	photovoltaic cells efficiency at standard conditions (-)
θ	incident angle (°)

Subscripts

a	ambient
app	apparent
b	beam
c	front node of the PV laminate
$cond$	conduction
d	diffuse
e	back node of the PV laminate
e_i	thickness of the solid layers
f	air or fluid
g	rear facing material
$g1$	front node of the rear facing material
$g2$	back node of the rear facing material

gPV	clear glass of the PV module
h	horizontal
i	inlet
m	weather station
n	normal
o	outlet
PV	photovoltaic cells
$PV1$	node of the PV cells layer
r	radiation
s	sky
t	turbulent
tr	semi transparent surface
T	total surface
wc	cold wall
wh	hot wall

Superscripts

b	back
f	front

References

[1] J.J. Bloem, A. Gandini, and L. Mazzarella. A TRNSYS type calculation model for double skin photovoltaic facades. 2004.

[2] J.J. Bloem and R. van Dijk. The PV module considered from an energy flow perspective. 2000.

[3] J.J. Bloem, W. Zaaiman, and D. van Dijk. Electric and thermal performance assessment of hybrid photovoltaic systems using the PASLINK test facility. 1997.

[4] J.J. Bloem. Evaluation of a PV-integrated building application in a well-controlled outdoor test environment. *Building and Environment*, 43(2):205–216, February 2008.

[5] P.A. Strachan and L. Vandaele. Case studies of outdoor testing and analysis of building components. *Building and Environment*, 43(2):129–142, February 2008.

[6] L. Mei, D. Infield, U. Eicker, and V. Fux. Thermal modelling of a building with an integrated ventilated PV facade. *Energy and Buildings*, 35:605–617, 2003.

[7] B.J. Brinkworth. A procedure for the routine calculation of laminar free and mixed convection in inclined ducts. *International Journal of Heat and Fluid Flow*, 21(4):456–462, August 2000.

[8] B.J. Brinkworth, R.H. Marshall, and Z. Ibarahim. A validated model of naturally ventilated PV cladding. *Solar Energy*, 69(1):67–81, 2000.

[9] B.J Brinkworth. Estimation of flow and heat transfer for the design of PV cooling ducts. *Solar Energy*, 69(5):413–420, 2000.

[10] B.J. Brinkworth and M. Sandberg. Design procedure for cooling ducts to minimise efficiency loss due to temperature rise in PV arrays. *Solar Energy*, 80(1):89–103, 2006.

[11] Ursula Eicker. *Solar technologies for buildings*. 2003.

[12] D. Faggembauu, M. Costa, M. Soria, and A. Oliva. Numerical analysis of the thermal behaviour of ventilated glazed facades in mediterranean climates. part i: development and validation of a numerical model. *Solar Energy*, 75(3):217–228, September 2003.

[13] Dirk Saelens and Hugo Hens. Experimental evaluation of airflow in naturally ventilated active envelopes. *Journal of Building Physics*, 25(2):101–127, January 2001.

[14] Dirk Saelens, Dirk Saelens, and Hugo Hens. *Energy performance assessment of single storey multiple-skin facades*. PhD thesis, Katholieke Universiteit Leuven, 2002.

[15] D. Saelens, S. Roels, and H. Hens. Strategies to improve the energy performance of multiple-skin facades. *Building and Environment*, 43(4):638–650, April 2008.

[16] Geun Young Yun, Mike McEvoy, and Koen Steemers. Design and overall energy performance of a ventilated photovoltaic façade. *Solar Energy*, 81(3):383–394, March 2007.

[17] Rémi Charron and Andreas K. Athienitis. Optimization of the performance of double-façades with integrated photovoltaic panels and motorized blinds. *Solar Energy*, 80(5):482–491, May 2006.

[18] Tingting Yang and Andreas K. Athienitis. A study of design options for a building integrated photovoltaic/thermal (BIPV/t) system with glazed air collector and multiple inlets. *Solar Energy*, 104:82–92, June 2014.

[19] Y. B. Assoa and C. Ménézo. Dynamic study of a new concept of photovoltaic–thermal hybrid collector. *Solar Energy*, 107:637–652, September 2014.

[20] J. Cipriano, G. Mor, D. Chemisana, D. Pérez, G. Gamboa, and X. Cipriano. Evaluation of a multi-stage guided search approach for the calibration of building energy simulation models. *Energy and Buildings. ENB-D-14-01064R1*.

[21] Solar Energy Laboratory and University of Wisconsin-Madison. TRNSYS 16-user manual. *User guide*, pages 273–282, 2005.

[22] J. Cipriano, G. Houzeaux, D. Chemisana, C. Lodi, and J. Martí-Herrero. Numerical analysis of the most appropriate heat transfer correlations for free ventilated double skin photovoltaic façades. *Applied Thermal Engineering*, 57(1-2):57–68, 2013. cited By (since 1996)0.

[23] Warren M. Rohsenow, James P. Hartnett, and Young I. Cho. *Handbook of heat transfer*. McGraw-Hill, May 1998.

[24] W.M. Kays, M.E. Crawford, and Weigand Bernard. *Convective Heat and Mass Transfer*, volume 4th Edition. 2004.

[25] S.W. Churchill and H. Ozoe. Correlations for forced convection with uniform heating in flow over a plate and in developing and fully developed flow in a tube. *Journal of Heat Transfer*, 95:78–84, 1973.

[26] N. K. Bansal, Rajesh Mathur, and M. S. Bhandari. Solar chimney for enhanced stack ventilation. *Building and Environment*, 28(3):373–377, July 1993.

[27] S. Kakaç, R.K. Shah, and W.Aung. *Handbook of single-phase convective heat transfer*. John Wiley & Sons, New York. USA, 1987.

[28] Frank P. Incropera and P. Dewit DeWitt. *Fundamentals of Heat and Mass Transfer*, volume 4th Volume. John Wiley & Sons, 1996.

[29] W.H. McAdams. *Heat Transmission*, volume 3rd. McGraw-Hill, New York. USA, 1954.

[30] D. Watmuff, J.H. Charters, and W.W.S. Proctor. Solar and wind induced external coefficients - solar collectors. *Cooperation Mediterraneenne pour l'Energie Solaire, Revue Internationale d'Heliotechnique, 2nd Quarter.*, 1977.

[31] L. F. A. Azevedo and E. M. Sparrow. Natural convection in a vertical channel vented to the ambient through an aperture in the channel wall. *International Journal of Heat and Mass Transfer*, 29(6):819–830, June 1986.

[32] S. Sharples. Full-scale measurements of convective energy losses from exterior building surfaces. *Building and Environment*, 19(1):31–39, 1984.

[33] S. Sharples and P. S. Charlesworth. Full-scale measurements of wind-induced convective heat transfer from a roof-mounted flat plate solar collector. *Solar Energy*, 62(2):69–77, February 1998.

[34] Technologies Department Building. OPTICS version 5.1. *Lawrence Berkeley National Laboratory*, 2006.

[35] Technologies Department Building. WINDOW version 5.2.a. *Lawrence Berkeley National Laboratory*, 2006.

[36] Antonio Parretta and Francesca Ferrazza. Method for measurement of the hemispherical/hemispherical reflectance of photovoltaic devices'. pp.-. *Optics Communications*, 194:17–32, 2001.

[37] Antonio Parretta and Haruna Yakubu. Non-destructive optical characterization of photovoltaic modules by an integrating sphere.: Part i: Mono-si modules. *Optics Communications.161*, pages 297–309, 1999.

[38] J. A. Duffie and W. A. Beckman. *Solar Engineering of Thermal Processes*. Wiley, 3 edition, August 2006.

[39] Robert Siegel. *Thermal Radiation Heat Transfer*. 2002.

[40] G. Barker and P. Norton. Building america system performance test practices: Part 1 - photovoltaic systems. *National Renewable Energy Laboratory (NREL), Golden, CO.*, NREL/TP-550-30301, 2003.

[41] Young Tae Chae, Jeehwan Kim, Hongsik Park, and Byungha Shin. Building energy performance evaluation of building integrated photovoltaic (BIPV) window with semi-transparent solar cells. *Applied Energy*, 129:217–227, September 2014.

[42] B. Marion. A method for modeling the current-voltage curve of a PV module for outdoor conditions. *Progress in Photovoltaics: Research and Applications.National Renewable Energy Laboratory*, 10(3):205–210, 2002.

[43] T.A. Reddy and I. Maor. Calibrating detailed building energy simulation programs with measured data - part II: application tothree case study office buildings (RP-1051). HVAC&R Research 13 (2), 2007.

[44] V. Corrado and E. Mechri. Uncertainty and sensitivity analysis for building energy rating. *Journal of Building Physics*, pages 33–125, 2009.

[45] J. Cipriano. *Experimental evaluation of the energy performance of ventilated double skin photovoltaic components. Chapter 3 of the PhD Thesis.* PhD thesis, University of Lleida, Lleida. October 2014.

[46] Andrea Saltelli, Marco Ratto, Terry Andres, Francesca Campolongo, Jessica Cariboni, Debora Gatelli, Michaela Saisana, and Stefano Tarantola. *Global sensitivity analysis: the primer*. John Wiley & Sons, 2008.

[47] Y. Zhang. "parallel" energyplus and the development of a parametric analysis tool. In *IBPSA 2009 - International Building Performance Simulation Association 2009*, pages 1382–1388, 2009. cited By (since 1996)6.

[48] Karl Pearson. X. on the criterion that a given system of deviations from the probable in the case of a correlated system of variables is such that it can be reasonably supposed to have arisen from random sampling. *Philosophical Magazine Series 5*, 50(302):157–175, 1900.

[49] Yongcai Li and Shuli Liu. Experimental study on thermal performance of a solar chimney combined with PCM. *Applied Energy*, 114:172–178, February 2014.

[50] J. Martı´-Herrero and M. R. Heras-Celemin. Dynamic physical model for a solar chimney. *Solar Energy*, 81(5):614–622, May 2007.

[51] ASHRAE. *ASHRAE Guideline 14, Measurement of Energy and Demand Savings*. ASHRAE Standards Committe, 2002.

[52] C. Lodi, P. Bacher, J. Cipriano, and H. Madsen. Modelling the heat dynamics of a monitored test reference environment for building integrated photovoltaic systems using stochastic differential equations. *Energy and Buildings*, 50:273–281, 2012.

Chapter 4

Global discussion of results

The main tangible results of this PhD thesis are summarized below:

1. An overall methodology for the integration of detailed analysis of the heat transfer processes, of experimental measurements in outdoor conditions of dynamic model and a multi stage calibration methodology.
2. An experimental set up for measuring the energy performance of ventilated PV components which allows for a detailed analysis of the effect of different ventilation regimes, including natural ventilation, several inclinations and rear facing materials.
3. An experimental parametric analysis of a semi transparent ventilated PV component in forced and natural convection with two different rear facing materials and six inclinations.
4. Three new TRNSYS types which constitute a flexible software frame for the implementation of several mathematic correlations and for the overall energy evaluation of semi transparent or opaque ventilated PV systems.
5. A multi stage calibration methodology which can be applied to both building energy simulation to models and to dynamic models of specific complex building components.

Furthermore, some specific results have been found in each of the papers that constitute the core of this PhD thesis.

Regarding the first paper, the main results of the physical hypothesis evaluation of the CFD code, is that the inlet modelling significantly affects the simulation results. It is found that the best modelling approach consisted in including an artificial extension at the inlet and applying a dynamic pressure boundary condition at the entrance of this extended domain. The FEM code is able to describe the heat transfer processes occurring in double skin façades with integrated PV under natural convection and in laminar regime, showing NMBE within the acceptable range of 5% when velocity and temperature profiles are calibrated with experimental measures. In the case of the average Nusselt number and symmetric or asymmetric with adiabatic wall situations, at least one mathe- matical correlation for each boundary case fits the numerical results with a high precision. In cases with pure asymmetric UHF there are no available mathematical correlations for the average Nusselt numbers. From the numerical results post process it can be observed that for $Ra_b > 1000$ there is no interaction between the boundary layers, therefore, existing mathematical correlations for symmetric UHF or for asymmetric UHF with adiabatic wall are both valid. For Ra_b below this limit, the two boundary layers interact and affect the

temperatures of the air in contact with the walls. New mathematical correlations are necessary to model the convective heat transfer coefficient in this region. Regarding the air mass flow rate, or the Reynolds number and cases of asymmetric UHF with adiabatic wall, no mathematical correlations were found in literature, therefore, further research to find suitable correlations for these situations is necessary. For situations with pure asymmetric UHF, correlations for the air mass flow rate were neither found in literature.

In the second paper, some specific results are found. In forced convection, it is stated that the thermal production increases with the *Re* and with inclinations close to the optimized inclination of each season. More specific conclusions can be obtained in relation to the distribution of PV temperatures. In forced convection, the PV temperature decreases when airflow rate increases but not linearly, this decrease is greater in turbulent regimen than in laminar one. It is also stated the PV temperature in natural convection situations is always warmer than in forced convection regardless the *Re*. The comparison between the ventilated PV module of TRE-L and the reference modules yields the conclusion that differences appear when *Re* approaches transition to turbulent regime and are significant for fully turbulent regime, reaching temperature differences between the insulated PV module and the ventilated PV of TRE-L of around 15 °C. In natural convection, however, the differences are not very appreciable and the ventilated PV of TRE-L is always in between the insulated and the free rack PV modules. These measurement conditions provide an indication for both the best and the worst working conditions of a PV module and allow for an effective comparison of the energy performance of the three PV modules. During the night it can be observed that, both in natural and forced convection, the temperature of the PV rapidly decreases and even achieves lower values than the ambient temperature. This negative temperature difference leads to a cooling effect over the air which enters the cavity in forced convection plus a downwards flow in natural convection. This behavior can be understood as a radiative cooling effect and could be used for passive cooling in summer period. In natural convection, the maximum values of air mass flow rate are not affected by the inclination, however, when the PV module is in optimized inclination, the night backwards flow is higher than in vertical inclination. The present work reflects the necessity of BIPV systems performance indicators under real operating conditions which clearly differ from both STC and NOCT standards.

The third paper, centered in the development and validation of a novel multi stage calibration methodology has obtained some specific results. Since the calibration methodology has been tested over a real unoccupied building, some results regarding the strong parameters detection can be found. It can be concluded that the parameters related to the air infiltration are clearly influencing parameters (strong) and the inclusion of two parameters depending on the outdoor temperature and on the wind velocity are preferable for a better modeling this physical phenomenon. Other influencing parameters, which are not so strong, are those related to the conductivity and the specific heat of the envelope materials. Regarding the sensitivity analysis, some more conclusions can be obtained: in cases where the Pearson χ^2 test is used as the sensitivity analysis, the threshold of the p-value should be around 1 %, since a small variation in this criterion has a big impact in both the detection of the strong parameters and in the goodness of fit of the simulations. The criteria to select a parameter as strong should also include a new test based on the level of change of the range of variation of the parameters after each iteration. In other words, to select a parameter as strong the posterior distribution, compared to the prior distribution, should have a considerable variation. Regarding the optimal LHMC sample size, it can be concluded that a minimum sample size of 15-19 times the number of unknown parameters is necessary to detect all the potential strong parameters and to achieve the minimum number of iterations which guarantee acceptable GOF ranges.

Regarding to the results of the calibration of the dynamic model in the last paper, some specific results are discussed below. It is concluded that the predominant air flow regime is the transition state from laminar to turbulence and that the main strong parameters are related to the hydraulic losses coefficient and to the Nusselt number correlation coefficients. The correlation of Bansal [26] obtains better results than the procedure of Brinkworth [7, 8, 9, 10] for the modeling of the air flow rate. However, further refinements or other alternative expressions should be tested because the major differences in the residuals are related to the prediction of the air mass flow rate. The other strong parameters are related to the transparency properties of the PV module. Another main conclusion is related to the electrical production of the PV module. The high precision in the prediction of the electricity produced by the PV module indicates a weak coupling between the electrical production and the heat transfer process that occurs in the ventilated air gap. This decopling could be justified because of the low density of PV cells, leading to the main conclusion that in the case of high transparent PV modules, the effect of the ventilated air gap over the electrical production is negligible should only be considered as a method to evacuate the incident solar radiation in the form or warmed air.

Chapter 5

General conclusions

The main conclusion of this PhD thesis is that a strong thermodynamic coupling exists between the air flow through the naturally ventilated PV component, the air temperature difference between the cavity and the outside, the incident solar radiation and the electricity produced at the PV module. This interaction can only be accurately predicted by sophisticated dynamic energy models which need to be evaluated against experimental measures. The evaluation or calibration of dynamic models is one of hot spots within the field of building energy modeling and many authors have been working on it for the last years and, as in the case of other building physics phenomena, it is one of the main pillars for this PhD to be consistent and coherent with the real energy performance of these complex PV components.

What can be also deduced from the results of this PhD thesis is that the whole process of defining the theoretical model, the experiments or monitoring measures and the methodology to perform the calibration, should be designed following a holistic approach with clear limits of level of detail in each process. Since the physical phenomenon is very complex, it is relatively easy to put a lot of attention in one of the aspects to be solved, while the other important factors are not considered and the overall vision is lost. A balance between the depth of the research in each stage and the overall scope is necessary. A clear example of this can be seen in the first paper of the thesis. As it is stated, in most of the ventilated PV components the air of the ventilated gap is flowing following a regime between the transition to turbulence to fully turbulence. Indeed, the boundary conditions in the solid parts of the PV system vary between adiabatic to pure asymmetric within a single day period . The detailed analysis of air under these transient and turbulent conditions is one of the most advanced themes within the computational fluid dynamics field and would have required a PhD thesis only focused on that. What was decided in this PhD thesis was to limit the study to the analysis of the existing correlations of heat and mass transfer with the aim to get more insights on the physic phenomenon and to find their range of applicability. From this first paper, it has been concluded that for a range $Gr < 10^4$, the effect of the asymmetry in the uniform heat flux boundary conditions (UHF) is negligible and correlations for symmetric UHF can be also valid for pure asymmetric UHF conditions. Within the range of $10^4 < Gr < 10^7$, which is the transition to turbulent region, it has been seen that the asymmetry in the boundary conditions clearly affect the air mass flow rate leading to higher velocities close to the hot wall. To properly model this effect, further research is necessary to find new suitable mathematical correlations.

Another example on how this PhD addressed the degree of in depth in measuring the real energy performance of ventilated PV components in real conditions, is described in the second paper. As it is well documented, indoor experiments are normally very accurate however they do not

take into account the dynamic variations in the boundary conditions once they are integrated into a real building. On the other hand, experiences involving the measurements of double skin BIPV systems in real buildings revealed that these studies are expensive and problematic in achieving good quality data, isolating the performance of the individual components, and extending results to different buildings, occupancies and climates. These constrains lead to the conclusion that controlled outdoor test facilities should be adopted in this research since they can be considered as an economical and practical intermediate bridge between laboratory tests and monitoring of real and occupied buildings. An improved version of the Test Reference Environment (TRE), has been constructed and monitored during two periods in two years. One of the main conclusions of the experiments was that the thermal production is dominant in the energy balance of the system. It has been also concluded that, from an energy efficient perspective, natural convection is a preferable option for producing both thermal energy and electricity. Although the air mas flow rate is smaller than in turbulent forced convection situations, the higher turbulence in the temperature field causes higher temperature gain within the air gap and, therefore, higher production of thermal energy. The positive effect of natural convection is not perceived in the case of electrical production, since it remains almost constant regardless the variation of air flow regime, rear facing material and inclination. This is mainly due to the fact that the analyzed PV module has a low density of PV cells, meaning that the electrical production is marginal compared to the solar energy which crosses the transparent surfaces and impacts in the rear facing material.

The third paper is centered in contributing to the increase of the knowledge in methodologies for the calibration of dynamic simulation models, but avoiding a too complex meta-model development, which is again, the way found to get a good balance in the level of detail of the study. A multi-stage calibration method based on the combination of the Latin Hypercube Monte Carlo method (LHMC) and sensitivity analysis, is presented for application to guided coarse grid search methods for calibrating BES under free floating situations. The method is useful for determining strong unknown input parameters and to obtain a set of top parameter combinations able to achieve a very precise goodness of fit criteria with the measured data. One of the main conclusions of this paper, is that the initial best estimated range of variation applied to the input parameters clearly constrains the results. A weak parameter can become strong if the initial range is extended or moved to other values, therefore, the result that a parameter is weak or strong should not be generalized but limited to the initial variational ranges. In addition to the re-assignment of narrowed ranges of variation over the strong parameters after each iteration, the PDF which is applied plays a crucial role in the sensitivity analysis precision. The multi-stage guided search approach presented in this paper, has also demonstrated a great precision in achieving minimum GOF criteria for a set of best trials, however it fails to capture the dynamics of the buildings. This approach is not able to fulfill the criteria of white noise for the residuals with enough statistical significance and presents some problems with auto-correlation of residuals. This lack of precision in capturing the building dynamics limits the application of this approach to analyses which aim at evaluating the influence of some building parameters such as the evaluation of the influence of renovation measures.

Following the coherence fixed in this PhD of developing an overall characterization methodology which should have a balance between complexity and accuracy, three new TRNSYS types have been developed and validated through monitoring experiments in the last paper. The very flexible programming environment of TRNSYS has allowed the implementation of numerical approximations of the heat conduction in the multilayer PV module, of several heat transfer correlations as well as the evaluation of the internal solar reflections. The unknown coefficients and parameters have been easily adjusted to the specific conditions of ventilated PV components with the previous validated calibration methodology. In this paper it has been demonstrated

that the combination of dynamic modeling with calibration methodologies is of critical importance to achieve a precise simulation of the real energy performance of complex components. It is not enough to implement very sophisticated differential equations, empirical correlations and complex solvers if there is no confronting with the real energy performance. Besides, this calibration should be embedded in the overall simulation methodology in a semi-automatic way to allow for massive batch running and optimization . The open software environments used in this paper, have permitted this automation by coupling the fundamental empirical physical models with strong statistical tools and introduce the needed degree of randomness and stochasticity in the empirical models. As was highlighted in the previous paper, the implemented dynamic model, combined with the multi-stage guided search approach, has demonstrated a great precision in achieving minimum GOF criteria for a set of best trials, however it has been failed in capturing the dynamics of the PV component. This lack of precision in capturing the dynamics, limits the application of this dynamic simulation model to medium to long-term evaluations of the electrical and heat energy production and to parametric analyses such as the evaluation of changes in the materials of the PV, in the rear facing material or in the air gap dimensions.

The overall methodology developed in this PhD which has been tested and contrasted with experiments, has demonstrated enough flexibility and great precision in achiving minimum differences with the measured results. However, some limitations have been detected. They are mainly related to the high complexity of evaluating, with a better precision, the heat transfer coefficients and the natural ventilated air flow rate and also related to the difficulties in measuring the air mass flow rate in natural convection. Regarding the theoretical modeling it has been evident that these kind of empirical models should be limited to medium to long term forecasting or to parametric analysis, but they are not valid for capturing the instant dynamics of these PV systems. In case that the designers are interested in short term dynamic modeling, other methods based on stochastic inverse modeling such as those developed by [27] and [24] are preferable. Considering the level of auto regression of the ambient temperature, of the solar radiation and of the residuals, auto regressive forecasting methods such as the ARIMA models would also be a another alternative short term forecasting method.

Bibliography

[1] J.J. Bloem, W. Zaaiman, and D. van Dijk. Electric and thermal performance assessment of hybrid photovoltaic systems using the PASLINK test facility. 1997.

[2] J.J. Bloem. Evaluation of a PV-integrated building application in a well-controlled outdoor test environment. *Building and Environment*, 43(2):205–216, February 2008.

[3] J.J. Bloem and R. van Dijk. The PV module considered from an energy flow perspective. 2000.

[4] J.J. Bloem, A. Gandini, and L. Mazzarella. A TRNSYS type calculation model for double skin photovoltaic facades. 2004.

[5] P.A. Strachan and L. Vandaele. Case studies of outdoor testing and analysis of building components. *Building and Environment*, 43(2):129–142, February 2008.

[6] Li Mei, D. Infield, U. Eicker, and F. Volker. Thermal modelling of a building with an integrated ventilated PV facade. *Energy and Buildings*, 35(6):605–617, July 2003.

[7] B.J. Brinkworth and M. Sandberg. Design procedure for cooling ducts to minimise efficiency loss due to temperature rise in PV arrays. *Solar Energy*, 80(1):89–103, 2006.

[8] B.J Brinkworth. Estimation of flow and heat transfer for the design of PV cooling ducts. *Solar Energy*, 69(5):413–420, 2000.

[9] B.J. Brinkworth. A procedure for the routine calculation of laminar free and mixed convection in inclined ducts. *International Journal of Heat and Fluid Flow*, 21(4):456–462, August 2000.

[10] B.J. Brinkworth, R.H. Marshall, and Z. Ibarahim. A validated model of naturally ventilated PV cladding. *Solar Energy*, 69(1):67–81, 2000.

[11] W. Aung, L. S. Fletcher, and V.Sernas. Developing laminar free convection between vertical flat plates with asymmetric heating. *International Journal of Heat and Mass Transfer*, 15(11):2293–2304, 1972.

[12] IEC-61215. *Crystalline Silicon Terrestrial Photovoltaic (PV) modules - Design Qualification and Type Approval*. 2005.

[13] T.Y.Y. Fung and H. Yang. Study on thermal performance of semi-transparent building-integrated photovoltaic glazings. *Energy and Buildings*, 40:341–350, 2008.

[14] M. Sandberg and B Moshfegh. Buoyancy-induced air flow in photovoltaic facades effect of geometry of the air gap and location of solar cell modules. *Building and Environment*, 37:211–218, 2002.

[15] Ursula Eicker. *Solar technologies for buildings*. 2003.

[16] D. Faggembauu, M. Costa, M. Soria, and A. Oliva. Numerical analysis of the thermal behaviour of ventilated glazed facades in mediterranean climates. part i: development and validation of a numerical model. *Solar Energy*, 75(3):217–228, September 2003.

[17] Dirk Saelens and Hugo Hens. Experimental evaluation of airflow in naturally ventilated active envelopes. *Journal of Building Physics*, 25(2):101 –127, October 2001.

[18] D. Saelens, S. Roels, and H. Hens. Strategies to improve the energy performance of multiple-skin facades. *Building and Environment*, 43(4):638–650, April 2008.

[19] Mats Sandberg and Bahram Moshfegh. Ventilated-solar roof air flow and heat transfer investigation. *Renewable Energy*, 15(1-4):287–292, 1998.

[20] B. Moshfegh and M. Sandberg. Flow and heat transfer in the air gap behind photovoltaic panels. *Renewable and Sustainable Energy Reviews*, 2(3):287–301, October 1998.

[21] B. Moshfegh and M. Sandberg. Investigation of fluid flow and heat transfer in a vertical channel heated from one side by PV elements. part i - numerical study. 1996.

[22] Geun Young Yun, Mike McEvoy, and Koen Steemers. Design and overall energy performance of a ventilated photovoltaic façade. *Solar Energy*, 81(3):383–394, March 2007.

[23] European Parliament. *Directive 2010/31/EU of the European Parliament and of the Council of 19 May 2010 on the energy performance of buildings*. 2010.

[24] C. Lodi, P. Bacher, J. Cipriano, and H. Madsen. Modelling the heat dynamics of a monitored test reference environment for building integrated photovoltaic systems using stochastic differential equations. *Energy and Buildings*, 50:273–281, 2012.

[25] T.A. Reddy and I. Maor. Calibrating detailed building energy simulation programs with measured data - part i: general methodology (RP-1051). HVAC&R Research 13 (2), 2007.

[26] N. K. Bansal, Rajesh Mathur, and M. S. Bhandari. Solar chimney for enhanced stack ventilation. *Building and Environment*, 28(3):373–377, July 1993.

[27] P. Bacher and H. Madsen. Identifying suitable models for the heat dynamics of buildings. *Energy and Buildings*, 43:1511–1522, 2011.